Title
Elucidating Interfacial Design Principles to Engineer Hybrid Gas Separation Membranes

Author
Su, Norman C.

Publication Date
2016

Peer reviewed|Thesis/dissertation

Elucidating Interfacial Design Principles to Engineer Hybrid Gas Separation Membranes

By

Norman Chi Su

A dissertation submitted in partial satisfaction of the

requirements for the degree of

Doctor of Philosophy

in

Chemical Engineering

in the

Graduate Division

of the

University of California, Berkeley

Committee in charge:

Professor Nitash P. Balsara, Co-chair
Dr. Jeffrey J. Urban, Co-chair
Professor Susan J. Muller
Professor Andrew Minor

Spring 2016

Elucidating Interfacial Design Principles to Engineer Hybrid Gas Separation Membranes

by Norman Chi Su

Abstract

Elucidating Interfacial Design Principles to Engineer Hybrid Gas Separation Membranes

by

Norman Chi Su

Doctor of Philosophy in Chemical Engineering

University of California, Berkeley

Professor Nitash P. Balsara, Co-chair
Dr. Jeffrey J. Urban, Co-chair

The dramatic rise in atmospheric carbon concentrations and consequences thereof has spurred a renewed effort to develop strategies to mitigate consumption of fossil fuels and emission of carbon dioxide. Membranes occupy a small niche within the larger strategy of carbon capture and storage as an effective medium to curb carbon dioxide emissions. However, to become competitive with incumbent technologies such as amine scrubbing, the performance of membranes needs to be greatly improved. Separation membranes are engineered to selectively permeate one molecular species over others through a combination of chemical and physical interactions between the molecule and gas. The performance limitations of current commercial polymeric membranes are due to an intrinsic trade-off between its permeability and selectivity. A novel and emerging approach to bypass traditional polymeric transport limitations is through the addition of inorganic nanomaterials. Inorganic materials often have inherently higher selective chemical and size sieving properties than polymers, but their material brittleness limits their large-scale adoption. However, we can harvest the selective properties of inorganics in hybrid polymer/inorganic composites to design membranes whose performance exceeds that of conventional polymers.

While promising, the primary obstacle towards developing high-performing hybrid membranes is to understand the role of polymer/inorganic interactions on molecular transport properties. These interactions can be highly complex and more often than not, the combination of a polymer and inorganic creates a non-selective membrane due to poor adhesion between phases. As a result, only a few systematic studies aimed to understand the complex nature of the interface have been reported in hybrid systems. Here, I describe the development of a model system using silica nanoparticles to examine contributions from the interface on transport properties. Utilizing this model system, I develop design rules for hybrid membranes and provide a scientific foundation on the role of inorganic size and surface chemistry on molecular transport properties. Polymer dynamics and structure, features that largely govern molecular transport properties, sensitively depend on three key variables (size, surface functionalization, and total volume loading) that are all linked by the total available interfacial surface area of the nanomaterials. From insights

gained in these model studies, I explore the design of a completely new class of dual transport membranes using metal-organic frameworks (MOFs) as the inorganic material. By pushing the boundaries of previously achievable MOF loadings, I demonstrate the ability to create a secondary transport pathway through a percolating MOF network, which bypasses transport inefficiencies of the polymer. The new transport channel through the MOF greatly enhances the total CO_2 permeability without sacrificing selectivity. Finally, I demonstrate the ability to design a flexible MOF membrane on a polymer support, leading to a new paradigm in inorganic membranes.

The findings presented in this dissertation offer a stronger understanding of fundamental transport properties in hybrid membranes and strategies to design membranes to overcome traditional limitations of polymer membranes. The utilization of dual transport membranes can lead to marked improvement in separation performance, which extends beyond carbon capture applications.

Dedication

To my beautiful daughter, Riley, who brings joy into my life everyday.
To my sweet wife, Mandy, who is my rock through thick and thin.
and finally
To my family and friends who have supported me through this journey.

Table of Contents

List of Figures

List of Tables

Acknowledgements

First and foremost, I would like to thank my advisor, Dr. Jeff Urban, for his guidance, mentorship, and belief that I could start a completely new research project. I do not know if I would have taken the same chance on me five years ago. His constant encouragement to let me define my research pathway, while challenging, enabled me to grow as a scientist and individual.

I am grateful to my co-advisor, Prof. Nitash Balsara, for supporting me in my journey up the hill to the Molecular Foundry and follow my passion for clean energy research. Our brief but enlightening conversations have guided me through these past five years.

I would like to place a very special thank you and sincere gratitude to Dr. Benny Freeman and his research group. Without his generosity, I would not be where I am today. The two trips to his lab over the course of two summers have been invaluable. I would like to thank Dr. David Sanders and Dr. Zach Smith for their supervision and insight as I visited their lab. I would like to also thank Dr. Qiang Liu and Kevin Stevens for showing me the membrane ropes. Also, I would like to thank Dr. Dan Miller, Ni Yan, and Dr. Kevin Tung.

I am grateful to the entire Gruppo Urban for their support and guidance over the years. Prof. Rizia Bardhan and Dr. Anne Ruminski who welcomed me into the group and are valued mentors. I am grateful for the scientific guidance, occasional golf outings, and daily coffee chats with Dr. Jason Forster, Prof. Nelson Coates, and Dr. Jared Lynch. I am thankful for Dr. Boris Russ for showing me how to succeed in graduate school. I am grateful for my desk neighbor Dr. Ayash Sahu for his insights and friendship. I still do not know how you convinced me to give two talks at AIChE, but I appreciate it. I am thankful for the rest for friendship I have with the entire gruppo. The post-docs: Dr. Fen Qiu, Dr. Eun Seon Cho, Dr. Karol Miszta, Dr. Woochul Lee, Dr. Heng Wang, Dr. Youngsong Kim, Dr. Peter Yang. The graduate students: Cynthia Chen, Eddy Zaia, Erin Creel, and Elizabeth Corson. The master students: Robin Mutschler, Paul Baade, and Max Szybowski. The intern: Maddie Gordon.

I am deeply grateful to the entire staff and members of the Molecular Foundry for their training, support, and scientific discussions. I am especially thankful to Tracy Mattox, Alyssa Brand, Dr. Tev Kuykendall, Dr. Emory Chan, and Dr. Nate Hohman for supporting the Inorganic Facility and keeping the lab from falling apart. I will not forget about the delicious treats you all (especially Alyssa) bring, the potlucks, the fitness challenges, and the lab clean-ups. I am thankful for the support from and discussions with Dr. Brett Helms, the Helms Group, Dr. Wendy Queen, Dr. David Britt, Liana Klivansky, Teresa Chen, Teresa Williams, Andrew Pun, David Hanifi, Carleton Falzone, Rick Kelly, Gil Torres, Dr. Paul Ashby, Virginia Altoe, Dr. Shaul Aloni, Dr. Lei Zhang, The Milliron Group, Dr. Evie Rosen, David Hom, Jason Sweet, Meg Holm, Branden Brough, Allison Hatt, and Ed Wong. A special thanks to Daniel Sun for the carpooling and the good times. I want to also thank the rest of the LBL community, especially the bus drivers, for waiting for me as I run for the bus to rescue my experiment on many occasions.

I want to thank the Chemical Engineering Department, especially my entering class of 2011. Peter Lobocarro, I still owe you a bachelor's party. The lunches with Eddie Buehler and David Liu. I will always believe that our class was and will be the most social class in the history of the department. I want to thank the CBE administrative staff Fred Deakin and Carlet Altamirano.

Finally, I want to thank my family and friends for their love and support through this not so straightforward journey. Their patience as I navigated the choppy waters provided me the stability I needed to reach the end. I am extremely grateful for my wife, Mandy, and her loving support and constant encouragement. I will never forget stuffing our faces in celebration or sadness. I am thankful for my daughter, Riley, and the smile she gives me every night I come home. I am grateful for my parents, Jin and Xiao-Hong, who provided and sacrificed for me, for their life lessons, and educational opportunities. I would not be here without everyone around me and I am eternally grateful every adventure we've been on.

Chapter 1. Introduction

1.1 Rise of Anthropogenic Carbon Dioxide Emissions

The discovery of fossil-based fuels (e.g. coal, oil, and natural gas) has led to a rapid acceleration of the globalization and modernization of our society. The advent of steam engines in the 18th and 19th centuries led to enormous improvements in manufacturing and transportation. Travel time from the Atlantic to the Pacific was reduced from several months to just a few days. The refining of crude oil into isolated products such as kerosene, gasoline, and diesel contributed to the mass adoption of automobiles and pushed the human frontier into space. Unfortunately, however, the global economy is still heavily dependent on fossil fuels; over 80% of total energy consumption is derived from the combustion of coal, oil, and natural gas as seen in **Figure 1.1a**.[1] The use of fossil-based fuels is not without consequences as was highlighted by the recent United Nations Climate Change Conference held in Paris at the end of 2015 to combat growing climate change globally.[2]

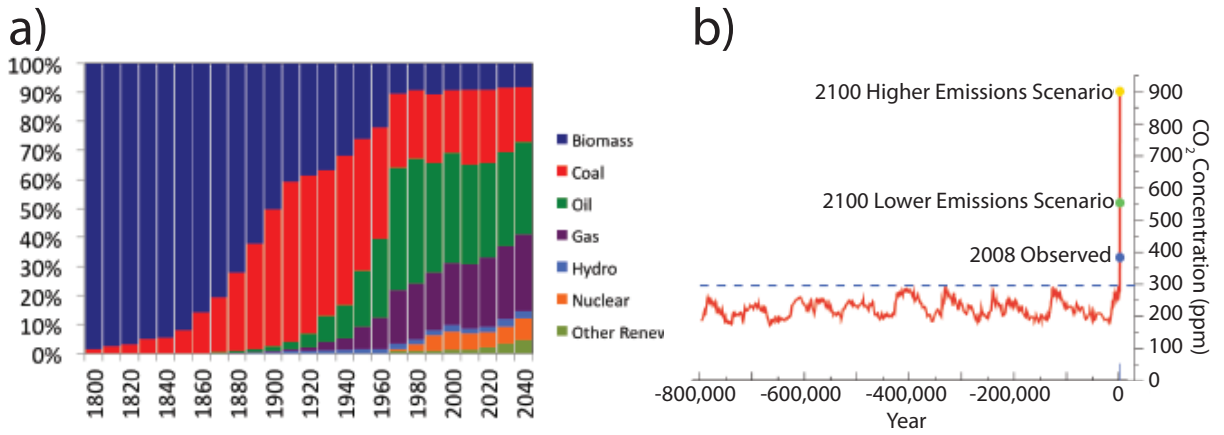

Figure 1.1. a) Adaptation of global energy consumption breakdown by fuel source.[1] Coal, oil, and gas dominate current and future global energy consumption. b) Analysis of air bubbles in Antarctic ice core samples. Historic CO2 levels are consistently below 300 ppm. CO2 can be expected to increase to 550-900 ppm if control measures are not taken.[3]

Carbon dioxide, a greenhouse gas, is one of two primary combustion products from fossil fuels, the other being water. In 2014, over 35 gigatons (Gt)[4] of carbon dioxide were freely emitted into the earth's atmosphere; for perspective, this is equivalent to the average CO_2 emissions of 5.8 billion automobiles. CO_2, at moderate levels, is critical for life because it absorbs rather than transmits infrared light. Without CO_2 in the atmosphere, the average global temperatures would be 60 °F lower, and thus unsustainable for human life. Unfortunately, atmospheric CO_2 concentrations have risen dramatically over the past 40

years as observed by the Mauna Loa Observatory in Hawaii. Historically, the average atmospheric CO_2 levels have rarely exceeded 300 ppm for hundreds of thousands of years as recorded by Antarctic ice core samples as seen in **Figure 1.1b**.[3] Even as late as 1960, the CO_2 was only at a modest concentration of 320 ppm. Today, as of the writing of this dissertation, the atmospheric CO_2 concentrations have exceeded 400 ppm.[5] If we continue our business as usual, CO_2 concentrations can be expected to reach at least 550 ppm and potentially 900 ppm by 2100.

In 2004, Pacala and Socolow proposed a portfolio of CO_2 emission reduction strategies known as stabilization wedges.[6,7] Each wedge represents a 25 Gt of carbon equivalent emission reduction over 50 years. A wedge can be derived from carbon capture implementation or efficiency improvements in 1) End-User Energy Efficiency, 2) Agriculture and Forestry, 3) Alternative Energy Sources, 4) Carbon Capture and Storage (CCS), and 5) Power Generation. Of these, CCS is the most immediate and deployable strategy. CCS is the process of capturing carbon emissions before or after the combustion of fossil fuels and storing the carbon by pumping supercritical CO_2 underground, converting it into a mineral, or regenerating it into chemicals (e.g. carbon monoxide, methanol). Carbon capture processes can be implemented most readily in three large-scale industrial processes: 1) Post-combustion, 2) Pre-combustion, and 3) Natural Gas Sweetening.[8]

Post-combustion: Carbon dioxide is separated from flue gas after the combustion of the fuel and prior to release into the atmosphere. Flue gas is primarily N_2 (65%) and CO_2 (14%). Carbon capture in post-combustion can be highly energy intensive due to the large volume of gas and low concentration of CO_2.

Pre-combustion: Carbon dioxide is separated from hydrogen after the gasification of coal (conversion of coal to syngas) or the steam reforming of methane into hydrogen and carbon dioxide prior to combustion. This process is advantageous because the fuel is completely converted to mostly CO_2 and H_2, resulting in a significantly higher CO_2 concentration than post-combustion (40% vs. 14%), where N_2 dominates the gas composition. Carbon capture in pre-combustion will be considerably less expensive and easier than post-combustion processes.

Natural Gas Sweetening: Raw natural gas is increasingly poisoned by carbon dioxide. Sweetening is the process of removing acid gases (e.g. CO_2) to meet specification limits. The presence of CO_2 prevents transportation of the fuel through pipelines, as it would lead to accelerated pipeline corrosion. Approximately 20% of total extracted natural gas must be extensively treated before pipeline delivery.

1.2 Carbon Capture Methods

CO_2 can be captured through many different techniques, each with their own energy penalties as illustrated in **Figure 1.2**. Of the methods listed, solvent extraction, adsorption, and membrane technologies are most relevant for carbon capture.

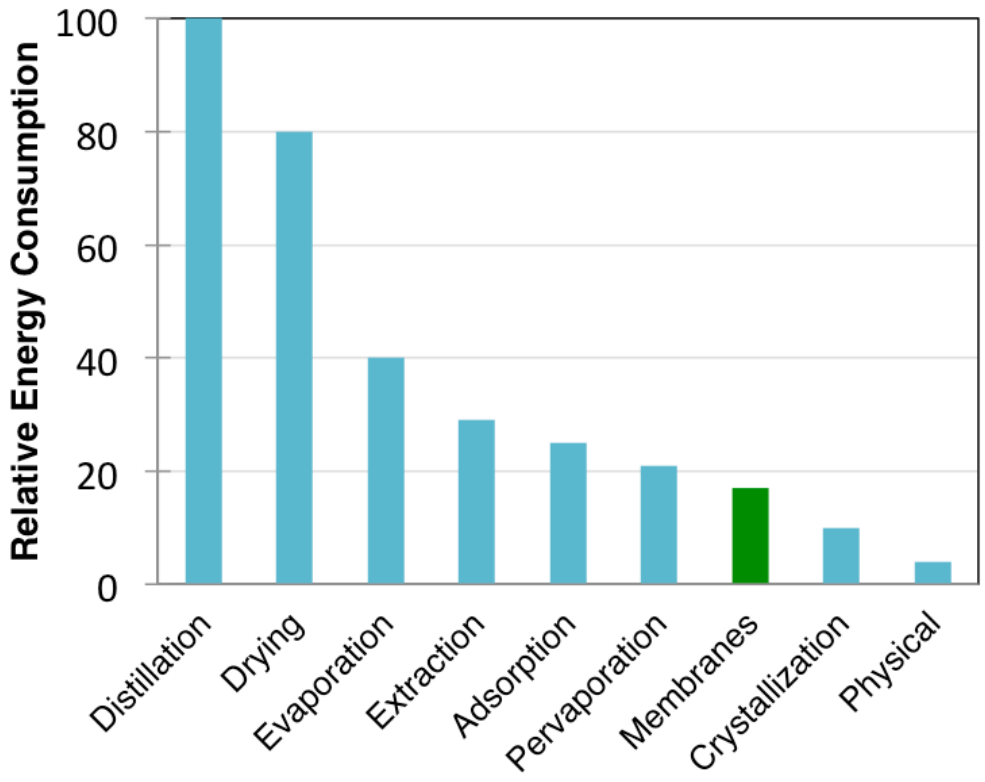

Figure 1.2 Relative energy consumption of various separation technologies.[9]

1.2.2 Solvent Extraction

Solvent extraction processes are a very mature and the primary go-to technology for carbon capture. The incumbent solvent utilized consists of 30% aqueous solution of monoethanol amine. CO_2 rich gas is processed at low temperature, where it reacts with the amine group to form a carbonate species. The CO_2 enriched solvent enters into a stripper column at elevated temperatures to release CO_2 as a purified product. Selexol, Rectisol, and KS-1 are other commercially used solvents utilizing different chemistries but rely on the same separation principle.[8] The process, while conceptually simple, can be very energy intensive due to strong enthalpy of formations of intermediate products and the cost to reverse the process. The parasitic energy costs can cannibalize 20-30% of the total electricity production.

1.2.2 Adsorption

Porous materials as basic as silica[10–12], alumina[13], and activated carbon[14] or more intricate materials such as zeolites[15,16] and metal-organic frameworks[17–20] can adsorb CO_2 through chemical or physical interactions. Adsorption is similar to solvent extraction, as it requires a temperature or pressure swing process to regenerate the adsorbent. The design of adsorption systems can be more complicated than solvent extraction due to the difficulty of transporting solid materials. However, the parasitic energy costs of adsorbents are moderately lower but still comparable to solvent extraction methods.

1.2.3 Membranes

Membranes, polymeric or inorganic, selectively permeate one gas over others due to a combination of physical and chemical interactions between the gas and membrane and will be the primary focus of this dissertation. An illustration of this process is depicted in **Figure 1.3**, where blue and yellow balls represent different molecular species. Unlike solvent extraction and adsorption processes, membranes can passively separate gases, (there is no need for a temperature or pressure swing). Further, the capital and size requirements of membrane-based technologies can be significantly lower due to the ability to process into hollow fibers or spiral wound modules.[21,22] The simplified operating process even further reduces the parasitic energy cost down to 10-20% if target permeation and selectivity are achieved (i.e. 1-2 order of magnitude increase in permeation and CO_2/N_2 selectivity of 30).[8] To envision how membranes meet the criteria for carbon capture applications, it is helpful to understand the fundamental principles and challenges of membranes and introduce current material designs initiatives to overcome these challenges.

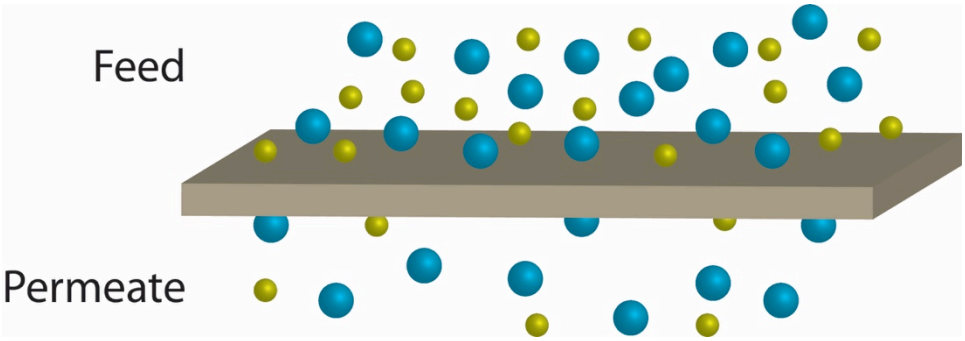

Figure 1.3. Illustration of membrane separation process. The membrane material selectively permeates blue balls over yellow balls due to more selective chemical and physical interactions.

1.3 Membrane Fundamentals

The performance of membranes is governed by two parameters: permeability and selectivity.[23] The permeability, P, is an intrinsic property of the membrane and reflects the relative rate of molecular transport through the membrane. Permeability is empirically defined as:

$$P = \frac{Nl}{p_2 - p_1} \qquad (1.1)$$

where N is the flux through the membrane (cm^3 (STP)/(cm^2 s)), l is the thickness of the membrane (cm), and p_2 and p_1 are the pressure of the feed gas and permeate, respectively (cmHg). The units of permeability are often converted from metric units to the widely accepted unit of "barrer". 1 barrer is equal to 10^{-10} cm^3 (STP) cm/(cm^2 s cmHg). The selectivity, α, is a parameter reflecting the ratio of the permeability of two different

molecular species (through the same system) and indicates the relative separation efficiency of the membrane. Selectivity is written as follows

$$\alpha = \frac{P_A}{P_B} \qquad (1.2)$$

where P_A is the permeability of the more permeable gas and P_B is the permeability of the less permeable gas.

There are many various mechanisms, which govern molecular transport through membranes (**Table 1.1**).[24] Of these, only molecular sieving and solution-diffusion will be considered as they offer the highest selectivity for carbon capture.

Table 1.1. Membrane Transport Mechanisms

Transport Mechanism	Pore Size	Selectivity
Bulk Flow	> 200 Å	Non-selective
Knudsen Flow	20-1000 Å	Low Selectivity
Surface Flow	5-10 Å	Moderate Selectivity
Molecular Sieving	< 5 Å	High Selectivity
Solution-Diffusion	Non-porous	Varies with Polymer

1.3.1 Molecular Sieving

Transport occurs by molecular sieving mechanisms when the pore diameters are comparable to the dimensions of individual molecules. Molecules with sizes smaller than the pore dimensions can permeate through the membrane, and molecules, which are larger, are blocked. The selectivity of molecular sieving materials can be very high, and many porous inorganic membranes obey the molecular sieving mechanism. While promising, the material brittleness of inorganics has inhibited the large-scale implementation and commercialization into membranes.[25]

1.3.2 Solution-Diffusion

The Solution-Diffusion model was originally proposed by Sir Thomas Graham in the 19th century when he observed the transport of gas through dense polymer films.[26] A feed gas is introduced at a pressure p_2 and concentration c_2 as illustrated in **Figure 1.4**. The permeate pressure and concentration are defined as p_1 and c_1. Molecular species flow in the membrane from the feed to the permeate by a three-step process:

1. Molecules dissolve into the feed side of the membrane according to its solubility coefficient.
2. Molecules diffuse from the feed side to the permeate side of the membrane.
3. Molecules desorb out of the membrane and into the permeate gas stream.

An assumption of the model is that pressure is constant throughout the membrane and equal to the feed pressure. Understanding the basis of the Solution-Diffusion model begins with Fick's first law of diffusion:

$$N = -D\frac{\partial c}{\partial x} \qquad (1.3)$$

where D is defined as the diffusion coefficient (cm^2/s) and $\delta c/\delta x$ is the concentration gradient profile across the membrane. Solving this differential equation, using the relationship that c/p equals the solubility coefficient, and assuming the concentration and pressure of the feed are significantly higher than the permeate, we arrive at the following equation:

$$P = DS \qquad (1.4)$$

where S is the solubility coefficient of the membrane (cm^3 (STP)/(cm^3 cmHg)), equal to amount of gas, which can dissolve in the membrane.

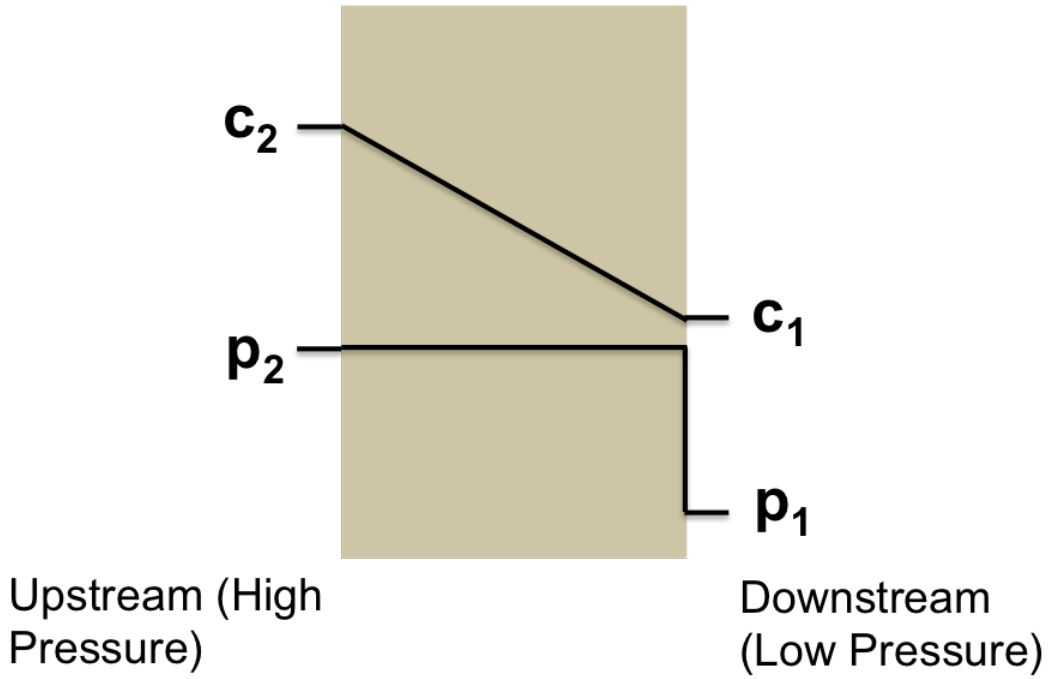

Figure 1.4. Underlying assumptions of the Solution-Diffusion Model. Driving force for molecular transport is governed by concentration gradient.

1.3.3 Diffusion

Diffusion through membranes is an activated process, and the diffusion coefficient can therefore be written as an Arrhenius relationship

$$D = D_o \exp\left(-\frac{E_D}{RT}\right) \qquad (1.5)$$

where D_o is the pre-exponential term (cm^2/s), E_D is the activation energy (kJ/mol), R is the gas constant (kJ/(mol K), and T is the absolute temperature (K).[23,27] The transition state occurs when the molecular species pass through a restrictive "neck" region between pores. This is easy to visualize in porous inorganic media such as metal-organic frameworks, which have defined pore dimension, but is slightly more complex for polymers.

To understand the transition state model in these systems, we must first consider the molecular structure of polymers. Polymeric membranes consist mainly of amorphous network of entangled polymer chains and in some cases crystalline regions. These crystalline regions are impermeable and will not be described further in this dissertation. Amorphous polymers pack very inefficiently and result in significant volume fraction of voids or free volume between polymer chains as illustrated in **Figure 1.5**. These voids can contain single or multiple gas molecules kinetically trapped. Diffusion through polymers occurs when the random thermal fluctuations of polymer chains creates an opening in the neck large enough to enable molecular species to hop from one void to another.

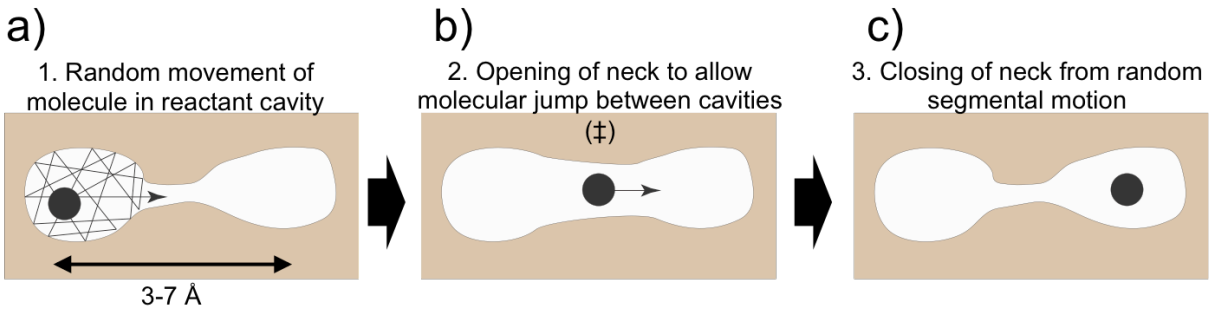

Figure 1.5. Molecular diffusion through polymers. a) Molecules are confined in voids between polymer chains. b) Random thermal fluctuation of polymer chains leads to a transition-state opening of a neck between two voids, allowing a molecular jump. c) The neck closes

The rate of diffusion can thereby be directly correlated to a molecular dimension, such as kinetic diameter, for light gases, which are more relevant for carbon capture. Selected molecular kinetic diameters are listed in **Table 1.2.**[23] This correlation, however, breaks down with larger molecules as rotational degrees of freedom begin to play a larger role.

Table 1.2. Physical Properties of Relevant Gases for Carbon Capture.

	Hydrogen	Carbon Dioxide	Nitrogen	Methane
Kinetic Diameter (Å)	2.89	3.3	3.64	3.8
T_c (K)	33.2	304.2	126.2	190.8

1.3.4 Solubility

The solubility of a molecular species defines the relative uptake capacity of the gas, which can diffuse across the membrane. A good indicator for the solubility of a molecular species is its critical temperature (**Table 1.2**). Molecules with higher critical temperature are more condensable and thus more enthalpically favored to dissolve into the membrane. Larger or more polar molecular species (CH_4 and CO_2) have a higher critical temperature, T_c; higher T_c typically correlates to higher solubility values than smaller and less polar species (H_2 and N_2). Unfortunately, there is an inverse relationship between the critical temperature, which correlates with solubility, and the kinetic diameter, which correlates with diffusion. Thus, a trade-off exists, especially in polymers, between diffusion and solubility, which leads to a larger and more critical performance barrier in polymeric membranes and will be discussed in the next section.

1.3.5 Robeson Upper Bound

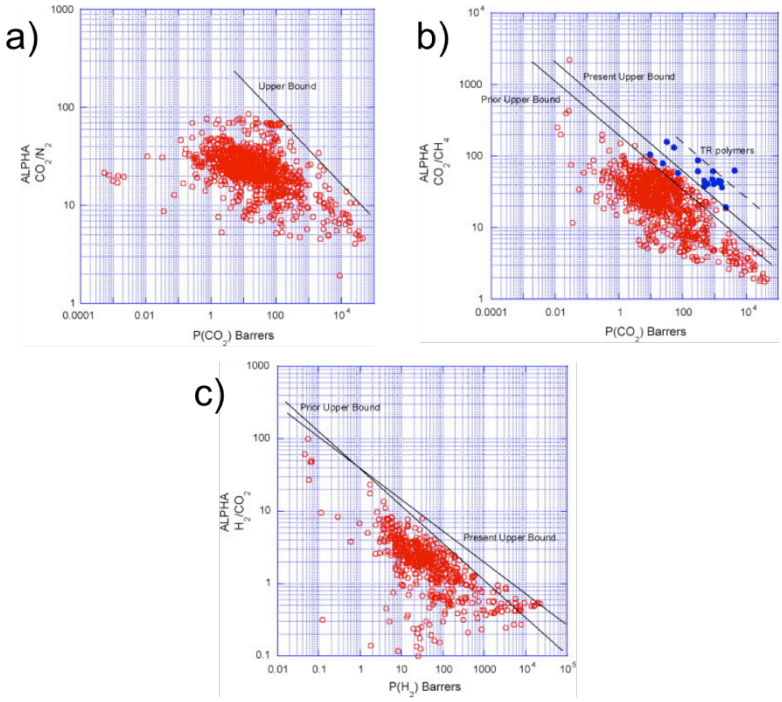

Figure 1.6. Robeson Upper Bound plots for a) CO_2/N_2 separation, b) CO_2/CH_4 separation and c) H_2/CO_2 separation.[28] Reproduced with permission from *Journal of Membrane Science.*

Popularized by Lloyd Robeson in 1991[29] and revised in 2008[28], the Robeson plot and Upper Bound illustrates the relationship between polymer membrane permeability and selectivity for various binary mixtures of gases constructed from data compiled in hundreds of publications. In the Robeson plot, the permeability of the more permeable species is plotted on the x-axis; its selectivity over various gases is plotted on the y-axis (**Figure 1.6**). We can quickly see that a trade-off exists between permeability and

selectivity. A membrane, which possesses high permeability, generally displays low selectivity and vice versa. The upper limit of membrane performance can be empirically drawn and is universally referred to as the Robeson Upper Bound.

While originally derived through empirical principles, the upper bound line was shown to have a fundamental relationship to chemical and physical properties of the polymer by Freeman.[30] The slope and intercept of the upper bound can be defined by the kinetic diameter of the gas molecule and relative rigidity of the polymer, respectively. As a result, the majority of performance improvements have occurred through increasing the diffusivity through simultaneous increases in pore volume and polymer backbone rigidity. Opportunities to increase performance through solubility selectivity enhancements are possible, but may be inhibited by decreases in diffusion. Examples of recent advances in polymer engineering to enhance performance are achieved with polymers of intrinsic microporosity (PIMs)[31,32] and thermally rearranged polymers (TR polymers)[33–36].

PIMs and TR polymers are a new class of designer polymers that exhibit both high permeability and selectivity. This is possible because of the high rigidity uniquely designed into the polymer backbone, which severely restricts polymer chain packing, and results in a polymer with significantly higher free volume than conventional polymers. Consequently, the transport mechanism through these polymers more closely resembles molecular sieves than solution-diffusion. Unfortunately, while these polymers initially exhibit high performance, their performance severely decreases due to collapse of free volume from polymer relaxation, when the thickness decreases to commercially relevant dimensions. The "aging" of polymers is of primary concern to many newer class of polymers. As a result, only a few polymers have been commercialized for membrane separation purposes: polysulfone, polyimide, cellulose acetate, polycarbonate, and silicone rubber. The properties of these polymers lie far below the Robeson Upper Bound. The CO_2 separation properties for polymers most relevant for carbon capture are tabulated in **Table 1.3**.

Table 1.3. Pure Gas CO_2 Permeability and Selectivity over CH_4 and N_2 for select polymers

Polymer	P_{CO2} (Barrer)	$\alpha_{CO2/CH4}$	$\alpha_{CO2/N2}$
Polysulfone[37]	5.6	27	30
Cellulose Acetate[38]	5.5	29	26
Polyimide[39]	10	36	31

1.4 Hybrid Organic Inorganic Membranes for Carbon Capture

Hybrid organic/inorganic membranes have attracted a growing interest in research because they show precedent to display significantly higher separation properties over pure polymers.[40,41] Hybrid membranes are not to be confused with mixed matrix membranes (MMMs)[42–45], which are both consider composite type architectures but embody fundamentally different principles. Both of these systems contain a polymer matrix and an inorganic nanomaterial dispersant. However, the difference between MMMs

and hybrids lies in the interface between the polymer and the inorganic. There are three modes of interaction between the organic and inorganic, which dictate the transport properties of the membranes. These are illustrated in **Figure 1.7**. The following scenarios are not limited to just membrane transport, and can be applied to any binary system.

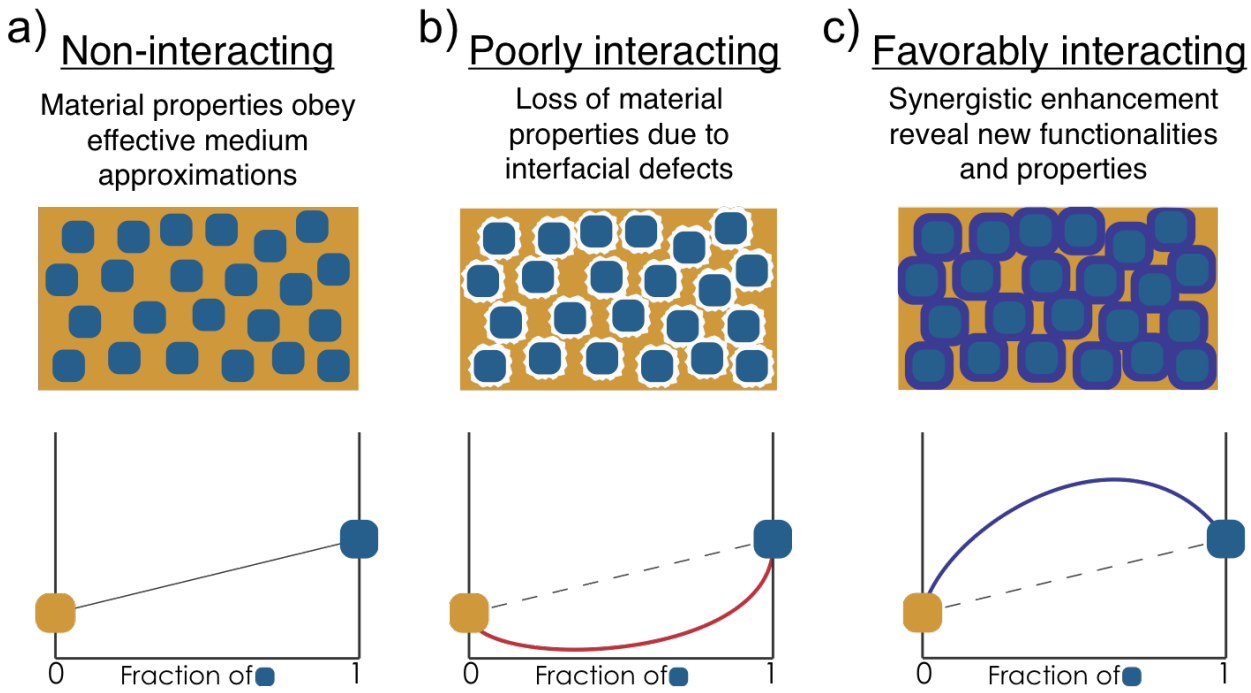

Figure 1.7. Modes of interactions between the organic (gold) and inorganic (blue) components.

Mode 1- Non-interacting

The non-interacting case is most typical of MMMs. In this case, the organic polymer and the inorganic component are indifferent towards one another. There is good contact between the two components, but the presence of one does not affect the material or transport properties of the other. The resulting molecular transport is then understood as an effective medium approximation, a linear sum of the two components.

Mode 2- Poorly Interacting

Here, the polymer and the inorganic interact unfavorably with each other. As a result, there is poor contact and adhesion between the two components and severe defects, in the form of interfacial voids, arise. The separation performance is severely degraded as molecular transport primarily occurs through the non-selective but highly permeable defects. Improper adhesion is one of the key early issues in hybrid or MMMs and this issue has persisted to this day.[42,46–49]

Mode 3- Favorably Interacting

The final mode is relevant to hybrid membranes and materials. Due to favorable interactions between the polymer and inorganic, a tertiary phase is formed at the interface. The properties of the membrane are improved through synergistic enhancements due to the new interfacial phase.[41] The molecular transport properties of the hybrid membrane are now greater than the sum of the individual parts.

In addition, to the performance enhancement achieved through the interface, hybrid membranes also offer many advantages over either pure polymers or inorganics such as enhanced selectivity, material robustness, and solution processability. Enhanced selectivity over pure polymers arises when inorganic materials are selected, which exhibit high selectivity for a molecular species due to chemical interactions or physical size selectivity.[50] This is possible due to the wider availability of inorganic elements, possible material combinations, and the rigid nature of inorganics when covalently bonded to form porous channels. In contrast PIMs and TR polymers are restricted to a few chemical classes of bis(phenazyl) and polyimides, respectively. Increased material robustness can be viewed from the perspective of both the polymer and inorganic. When inorganic nanomaterials are added to polymers and favorable interactions are present, the hybrid system will display significantly higher mechanical and thermal stability over pure polymers. Purely inorganic membranes, while very promising as membranes, are very difficult to scale due to constraints in material brittleness and cost to scale. By combining with polymers, hybrids can harvest the selective properties of the inorganic species without concern of membrane brittleness typical with inorganics. Finally, hybrid membranes maintain the solution processability of polymers, which is advantageous, as it enables roll-to-roll processing and ease of scale-up.

1.4.1 Types of Inorganic Nanomaterials

Early hybrid/composite membrane reports showed great promise, as exemplified by the seminal paper by Freeman *et al.* in 2002.[51] However, most of the development in hybrid membranes is driven by advancements in polymer science and typically use inorganic materials that are widely available in catalogues. As a result, the inorganic materials are poorly controlled, inhomogeneous, and polydisperse. Thus, significant headroom exists to develop understanding of molecular transport in hybrid materials if we focus on development of well-controlled inorganic nanomaterials. Inorganic nanomaterials can broadly be divided into two main categories: non-porous and porous. Non-porous materials function as an avenue to impart structure/property changes of the polymer for transport and may actively contribute to permeability/selectivity enhancements through surface interactions with molecules. Porous materials primarily introduce a new transport mode, namely molecular sieving, as well as chemical selectivity enabling significantly higher performance.

<u>Non-porous</u>

Non-porous inorganic materials are further classified by its level of “activity” or interaction with molecular species. Inactive materials do not exhibit any chemical selectivity with the molecular species. Instead, these materials induce separation performance enhancements by structure/property relationships through changes in structural or dynamical changes in

the polymer.[52] Silica is the most common material used[51,53–57]; though titanium dioxide[58] has been used also. Silica is widely used because of its availability and general inertness towards many chemicals and polymers. A seminal paper by Freeman *et al.*[51] in 2002 used fumed silica to alter and enhance the free volume elements of poly (methyl pentene) for butane separation from methane. This was possible because the fumed silica could disrupt the packing efficiency of the polymer chains. Active materials, as expected, exhibit chemically selective interactions within a given molecular species (e.g. CO_2) and present significantly more opportunities to improve separation performance. Active materials are a natural evolution from inactive materials once structure/property relationships are established. Performance enhancements are realized with active materials through two avenues. First, it serves to increase solubility of given molecular species it interacts with from native surface properties or through introduction of functionality groups on the surface, as is shown in this dissertation. However, care must be taken, as there is a delicate balance between solubility improvements and diffusion reductions, when selecting an active material. An increase in solubility due to selective interactions can actually increase the activation energy required for diffusion, and thus reduce diffusion. Second, if designed properly, the addition of active materials can introduce a new transport mechanism known as facilitated transport[59–61]. If active sites on the inorganic nanomaterial surface are spaced close enough, molecules will be able permeate across the membrane through hopping from one active site to the next. Common inorganic materials for carbon capture applications include MgO[62], other basic metal-oxides[13] and nickel[63]. Silver[60,64,65] is also an interesting material for the separation of olefins.

Porous

Porous materials used in hybrid or MMMs include carbon molecular sieves[39,66], microporous silica[67–69], zeolites[70,71], and most recently metal-organic frameworks[43,72–75]. The later three all consist of regular well-defined crystalline pore structure, while the former contains less defined amorphous network of pores. Porous inorganic materials are advantageous to their non-porous counterparts because they do not inhibit the diffusion of molecules, and can lead to significantly higher separation performance. The dimension of the pores governs the separation efficiency of porous materials; an ideal pore size would fall between the kinetic diameters of two molecular species. Of the different porous materials listed, metal-organic frameworks (MOFs) have shown the most promising for improving separation performance. MOFs are a new class of 3-D porous crystalline materials, which can exhibit surface areas up to 6000 m^2/g.[76] For perspective, the surface of a football field is roughly 5300 m^2/g. High surface areas enable higher capacity uptake for molecule (e.g. solubility) in membranes and will lead to increases in permeability. MOFs consist of a metal cluster linked together by organic ligands. The coordination preference of the metal and the length of the organic ligand govern the shape and size of the pore. As a result, an almost unlimited number of MOFs can be synthesized for any number of applications. Further, chemical functionalities can be attached to the MOF through the ligand or at open-metal sites, which enable even more tunability and selectivity for molecular species. One particular MOF of interest is the amine derivative of UiO-66.[17] UiO-66 is a zirconium based MOF and exhibits high CO_2 adsorption and water stability. The later of these is valuable for carbon capture applications. A CO_2 enriched stream will most likely contain water, and the presence of water can lead to decomposition of the crystalline

structure inherent to the MOFs. While MOFs are a promising materials system, they mainly come in the form of a loose powder because they are primarily synthesized through solvothermal techniques. This powder form severely inhibits the commercial applicability of MOFs. To combat this, methods have been derived to coalesce MOF into pellets or grown directly onto rigid substrates, but significant headroom exists to improve the usability of MOFs further.

1.4.2 Predicting Transport in Hybrid Membranes

Transport through hybrid membranes is oftentimes difficult to predict due to the complexities arising from non-ideal interactions between the polymer, inorganic, and gas. A comprehensive list of various ideal and non-ideal models for transport predictions in MMMs can be found here.[77,78] The remainder of this section will focus on a simple effective medium model known as Maxwell's Model. Models that can consider non-idealities require making unproven quantitative assumptions simply to fit the data to the model. Thereby, Maxwell's model is chosen as the primary model in this dissertation because it presents a baseline for which results can be meaningfully compared and is also the most commonly used model in literature.

Maxwell's model attempts to predict the gas permeability of a composite system, and is analogous to the more extensively studied permittivity of dielectrics. Maxwell's model is written as follows:

$$P_{Maxwell} = P_p \frac{nP_d + (1-n)P_p - (1-n)\phi_d(P_p - P_d)}{nP_d + (1-n)P_p + n\phi_d(P_p - P_d)} \qquad (1.6)$$

where $P_{Maxwell}$ is the permeability of the composite, P_p is the permeability of the polymer, P_d is the permeability of the dispersed inorganic phase, ϕ_d is the volume fraction of the dispersed phase, and n is the conflated shape factor and orientation of the dispersed phase. When n = 0, the dispersed phase spans across the membrane in parallel to the direction of molecular transport. When n = 1, the dispersed phase is perpendicular to the direction of transport. The most ubiquitous form of this equation appears when n = 1/3, and the dispersed phase adopts a spherical form factor. In this scenario, the model reduces to Maxwell's equation and is written as follows:

$$P_{Maxwell} = \frac{P_d + (1-2\phi_d) + (2-2\phi_d)P_p}{P_d(1-\phi_d) + (2+\phi_d)P_p} \qquad (1.7)$$

Further simplifications can be made if assumptions are made about the permeability of the dispersed phase. When the dispersed phase is completely impermeable ($P_d = 0$), Maxwell's equation reduces to

$$P_{Maxwell} = P_p \frac{(2-2\phi_d)}{(2+\phi_d)} \qquad (1.8)$$

This form of the equation in important as it relates the expected permeability when non-porous inorganic materials are used. Similarly, if we assume the dispersed phase is infinitely permeable ($P_d = \infty$), the equation reduces to

$$P_{Maxwell} = P_p \frac{(1 + 2\phi_d)}{(1 - \phi_d)} \qquad (1.9)$$

While convenient, Maxwell's model is a poor predictor of permeability in hybrid systems, where interphase interactions can greatly affect transport properties. As seen in the equations above, Maxwell's primarily depends on the dispersed phase's volume fraction and shape, but present a baseline and framework to understand how interactions are contributing to non-ideal changes in molecular transport.

1.4.3 Factors to Consider

Inorganic Size

Maxwell's model only considers the total loading of the inorganic dispersant and nothing else. However, I speculate that size can greatly contribute to deviations from the model due to difference in the interaction with the polymer. It is helpful to make a comparison to the relative size of polymer chains (e.g. the radius of gyration, R_g).[52] The interaction between the polymer and inorganic are the same, independent of the inorganic size. However, when the inorganic is significantly larger than the R_g, the observed effect is negligible as the interfacial surface area per unit volume of inorganic is very low. Conversely, as the inorganic size approaches the R_g, these interfacial interactions begin to play a significant role in molecular transport properties. This is visualized in **Figure 1.8a**. There has been no considerable effort to accurately investigate and quantify the size effect in gas separation membranes, mainly because much of the research has focused on the development and engineering of new polymeric materials. Fumed silica is a primary component in composite or MMMs. However, fumed silica is a less than ideal material system to conduct fundamental transport studies. For example, while the reported particle size is 12 nm, in actuality, fumed silica is highly polydisperse and aggregated (**Figure 1.8b**). Covalently bonded, these "12 nm" particles aggregate into network chain spanning multiple orders of magnitude. Thus, de-convolution of the multiple length scales can lead to a stronger more fundamental understanding of the influence of size from the inorganic species. Further, size of the inorganic matter can influence the packing efficiency of the polymer chain. As the inorganic size approaches the R_g of the polymer, the inorganic can hinder the packing of the polymer and lead to an increase in the available free volume.

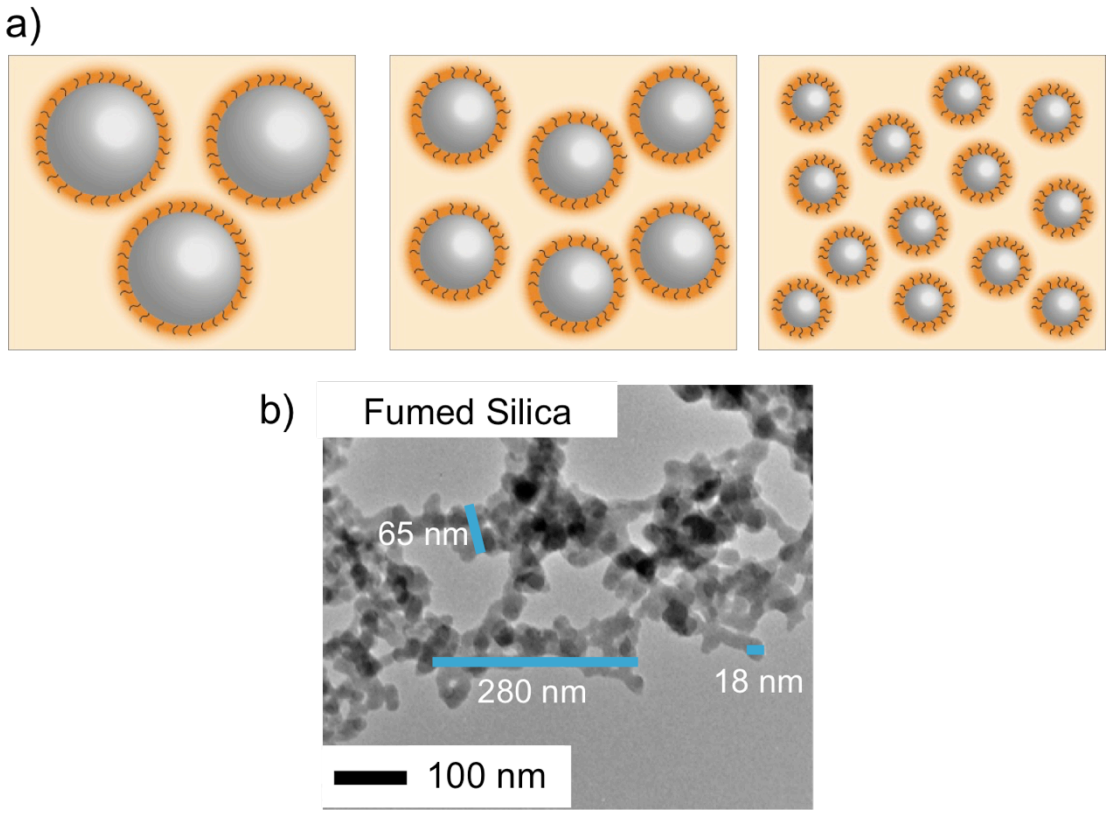

Figure 1.8. a) Interfacial interaction between the polymer and inorganic influences material properties more strongly as inorganic size decreases and approaches respective dimensions of the polymer. At smaller nanoparticle sizes, surface area per unit volume increases, thus increasing total available interaction. b) TEM image of fumed silica illustrating the polydispersity and aggregated nature of the material.

Inorganic Surface Chemistry

The surface chemistry of the inorganic component plays a dual role in governing molecular transport properties and can significantly influence the mode of interfacial interaction. If the inorganic is inactive towards molecular species, the interfacial interaction with the polymer strongly dictates how transport performance changes through hydrogen bonding, van der Waals, or direct covalent bonding. The primary response to any observed interaction can be captured by monitoring changes in polymer chain dynamics. The glass transition temperature (T_g) and the thermal response from the transition from a glass to a rubber are useful metrics to understand how interfacial interactions effect polymer dynamics.[79–81] there are three modes of perturbation on T_g that can be observed: negative shift, positive shift, and broadening. First, an inorganic that weakly interacts with the polymer results in an increase in the segmental chain motion, a relaxation of the polymer, and subsequently a decrease in the T_g. The polymer perceives the inorganic surface as a free surface, similar to a polymer-air interface, where movements in polymer chains are not sterically hindered by a solid surface. Second, a strong interaction between the polymer and inorganic can lead to an increase in the T_g due to a reduction in segmental chain mobility. Finally, rather than an absolute increase or decrease in T_g, select polymers

undergo a broadening of the thermal transition region from non-cooperative changes in polymer dynamics. The fragility of the polymer dictates whether the T_g transition undergoes a shift or broadening. Fragility in polymers is understood as the rate at which cooperative segmental dynamics of glass-forming liquids changes as T_g is approached.[82–84] A polymer with low fragility is considered "strong" and the segmental motion of polymer chains is not dependent on its neighboring chains. Thus, in strong polymers, the interactions between the polymer and inorganic slowly fade as one moves away from the interface. As a result, the polymer would be expected to exhibit a broadened transition. Alternatively, a "fragile" polymer exhibits high cooperativity in polymer segmental dynamics and direct T_g shifts would be observed. Furthermore, when chemical functionalities are added to the surface, which selectively interact with certain molecular species, the inorganic becomes active towards molecular species and lead to increases in solubility of the molecule in the membrane.[85,86] For example, as will be shown in this dissertation, amine groups can be introduced on the surface and selectively interact with CO_2 to form reversible carbonate species.

A fundamental study on the effects of inorganic size and surface chemistry is critical to more critically understand transport behavior in hybrid membranes. The effect can be as simple as increasing the solubility of a molecular species or more complex and range from introducing new transport mechanisms to multi-faceted structure-property relationships.

1.4.4 Beyond Hybrid Membranes

Hybrid membranes are currently garnering significant attention in the field primarily because they take advantage of the selective properties of the inorganic component. While solution processability is maintained in hybrid systems, the transport properties are still constrained to solution diffusion transport in polymers. Thus, opportunities exist to leverage polymer/inorganic interactions to induce continuity and stability of inorganic materials across the membrane leading to significant enhancements in membrane separation efficiencies.

1.4 Outline of Dissertation

In this dissertation, I explore the interfacial relationship of inorganic/polymer properties on gas transport and leverage the initial findings to design high performing carbon capture membranes.

In Chapter 2, I create a design space to explore the role of inorganic size on molecular transport properties in a model system. The model system consists of inactive non-porous silica nanoparticles as the inorganic phase and cross-linked poly (ethylene glycol) as the polymer. The decrease in nanoparticle size leads to a surprising decrease in gas permeability not predicted by Maxwell's equation. The contributing factor to the permeability decrease is quantified by the total surface area interactions.

In Chapter 3, surface functionalization of the silica surface with amino-propyl groups create an active surface for molecular interactions and leads to a complete reversal in CO_2 permeability observed in the previous chapter. The improvement in permeability over the pure polymers is coupled to simultaneous increases in mechanical and thermal stability of the membrane

In Chapter 4, the insights learned from chapter 2 and 3 are applied towards designing a high-performing CO_2 capture membrane utilizing metal-organic frameworks as the inorganic material. The MOF forms a percolating network and allows for molecular species to more quickly diffuse through the new secondary MOF pathway.

In Chapter 5, I exploit a polymer surface to covalently attach a continuous MOF layer and explore its gas transport properties.

The design of hybrid membranes to improve membrane separation performance is necessary to overcome the relative ease of implementing energy inefficient solvent extraction and adsorption methods. Applying the insights learned here, the implementation of a widespread carbon capture strategy is within our reach.

Chapter 2. Size-Dependent Permeability Deviations from Maxwell's Model in Hybrid Cross-linked Poly(ethylene glycol)/Silica Nanoparticle Membranes

Adapted from "Size-Dependent Permeability Deviations from Maxwell's Model in Hybrid Cross-linked Poly (ethylene glycol)/Silica Nanoparticle Membranes." N.C. Su, Z.P. Smith, B.D. Freeman, and J.J. Urban. *Chemistry of Materials*, 2015, 27, 2421 (DOI: 10.1021/cm504463c). Reproduced with permission from *Chemistry of Materials.*

Currently, separation of gaseous mixtures largely relies on energy intensive and expensive processes, like chemical looping of amines. This has driven research into less energy-intensive, passive methods of performing separations such as the use of polymer membranes. While pure polymer membranes have demonstrated appealing separation performance, they suffer from an inherent trade-off between permeability and selectivity, which limits overall performance. Recent research efforts have shown that the introduction of a secondary phase, often an inorganic species, is added to selectively boost permeability and/or selectivity. However, these hybrid organic/inorganic systems have not seen widespread adoption because synthetic control over the size, shape, and dispersion of the inorganic species is poor, and understanding of transport in these membranes is largely empirical. Thus, understanding and optimizing hybrid membranes requires development of well-controlled model systems in which size, shape, and surface chemistry of the inorganic species are precisely controlled, leading to homogeneous membranes amenable to careful study. Here, I report on the synthesis, characterization, and gas transport properties of tailored hybrid membranes composed of cross-linked poly(ethylene glycol) and silica nanoparticles. I show excellent control of nanoparticle size, loading, and dispersability. I find that permeability deviations from Maxwell's model increases as the size of silica nanoparticle decreases and loading increases. These size-dependent deviations from Maxwell's model are attributed to interfacial interactions, which scale with surface area and act to decrease segmental chain mobility.

2.1 Introduction

The use of membranes for gas separation processes is becoming increasingly important for applications in carbon capture, hydrogen purification, and natural gas sweetening.[8] Membranes are highly energy efficient as they do not require temperature or pressure cycles to perform separations, unlike current methods like chemical looping of amines. An ideal membrane would possess both high permeability and selectivity as it would decrease the physical footprint and result in a higher purity product. However, pure polymer membranes suffer from an inherent empirical trade-off in permeability and selectivity commonly known as the Robeson Upper Bound.[28]

Improving the performance of polymer membranes can be achieved by increasing the diffusion or solubility coefficient of the gas with respect to the polymer as proposed by the solution-diffusion model.[23,87] However, improvements in membrane performance have primarily been achieved through diffusivity enhancements arising from an understanding of structure/property relationships, and less commonly with solubility enhancements. The diffusion of gases through polymer films is an activated process driven by thermal fluctuations in the polymer chain. Thus, by simultaneously increasing polymer chain stiffness and interchain spacing, it is possible to increase the diffusive properties of the polymer to a point where interchain spacing becomes so large that the solution-diffusion model fails. Current examples of this strategy are exemplified in polymers of intrinsic microporosity[31,32] and thermally-rearranged polymers[33]. Unfortunately, these polymers lose their performance over time and have been difficult to synthesize on a large-scale, thereby limiting their commercial applicability.

A complementary approach relies on adding a secondary phase, often an inorganic species, to selectively boost permeability or selectivity. Recently, these hybrid membranes have shown promising enhancements in permeability and selectivity, some of which even surpass the Robeson Upper Bound.[51,55] The enhancement in gas transport is credited to synergistic improvement in the morphological structure of the polymer or contributions from an inherently higher selective inorganic species. Specifically, addition of an inorganic phase can enhance gas transport via several mechanisms such as acting as a diffusion barrier[88] or channel[39,44,67,75], disrupting polymer chain packing[51,53], increasing void volume[54,58,89], or interacting favorably with specific gases.[65,90,91] The extent and character of the modification on gas transport depends on the porosity, size, surface chemistry, and composition of the inorganic species. Gas transport through hybrid systems is oftentimes understood by applying simple effective medium approximations, such as Maxwell's model[77], but these models do not account for variability of the inorganic phase and interfacial interactions. While hybrid membranes display desirable properties, further advancements in hybrid membranes are hampered because the understanding of transport mechanisms is limited to empirical relationships, and the isolation of independent variables has been difficult. This is due to the poor synthetic control over the size, shape, and surface of the inorganic species, which often span from single nanometers to microns. As a result, the dependence of interfacial interactions as a function of inorganic size and their impact on over gas transport has not been well understood.

I report the preparation of a tunable and well-controlled hybrid membrane system of silica nanoparticles distributed within cross-linked poly(ethylene glycol), XLPEG. Through this system, I aim to better understand the influence of polymer-inorganic interactions on gas transport. I systematically vary the size of silica nanoparticles over a large range with diameters of 12 ± 1.2 nm, 41 ± 3.9 nm, and 130 ± 6.5 nm and loading from 0 to 30 volume percent. Silica nanoparticles were chosen because they are chemically neutral and should not express any selectivity amongst the gases tested. As a result, only interactions between the XLPEG and silica contribute to transport deviations from Maxwell's model. I examine the effect of varying silica nanoparticle size and loading on interactions between the XLPEG and silica through differential scanning calorimetry (DSC) measurements around the glass transition, Tg, region and attempt to relate microscale morphology behavior to macroscale gas transport properties. Pure gas permeabilities of hydrogen, nitrogen, methane, and carbon dioxide, as well as the selectivity to CO2 are presented. Permeability deviations from Maxwell's model were found to be dependent to silica nanoparticle size due to increased interaction at the interface between silica and XLPEG and were predicted through DSC measurements.

2.2 Experimental Procedure

Materials. Poly(ethylene glycol) diacrylate (PEGDA, M_n = 700), 2,2-Dimethoxy-2-phenylacetophenone (DMPA), ammonium hydroxide, tetraethyl orthosilicate (TEOS), and Ludox SM silica were purchased from Sigma Aldrich. 70% HNO_3 was purchased from Alfa Aesar. All chemicals were used as received. Hydrogen, nitrogen, methane and carbon dioxide with a purity of at least 99.97% were purchased from Praxair for use in gas permeation studies.

Silica Nanoparticle Synthesis and Preparation. Silica nanoparticles of 41 and 130 nm diameters were prepared following the Stöber method.[92] Ammonium hydroxide, water, and ethanol were mixed at pre-determined amounts. TEOS was added to give a final concentration of 0.15 M. The volume of ammonium hydroxide, water, and ethanol added was determined through an empirical correlation developed by Bogush and co-workers[93] based on TEOS concentration and desired final particle size. The synthesized silica nanoparticles were cleaned by centrifugation with ethanol and finally dispersed in isopropanol. Ludox SM (~12 nm) were transferred from an aqueous solution to an alcoholic solution by mixing Ludox SM with 60:1 ratio of ethanol:nitric acid followed by centrifugation. The nanoparticles were then redispersed in ethanol, centrifuged, and finally dispersed in isopropanol. Nanoparticles were deposited onto a holey carbon copper TEM grid and imaged using a Zeiss Libra 120 transmission electron microscope operated at 120 keV. Nitrogen adsorption measurements were performed at 77 K using a Tristar II (Micromeritics). Surface area values were calculated following Brunauer-Emmet-Teller method over a relative pressure range, p/p_o, of 0.05 to 0.25.

Membrane Preparation. XLPEG films were fabricated following published procedures.[94] A polymer solution containing PEGDA and 0.1 wt% of the initiator DMPA were pre-mixed. Silica nanoparticles in isopropanol were then mixed with the polymer solution to give a

final dry silica volume loading of approximately 0 vol%, 8.5 vol% (15 wt%), 18 vol% (30 wt%), and 30 vol% (45 wt%). The mixture of silica, polymer, and isopropanol was placed under nitrogen flow to slowly evaporate all of the isopropanol with occasional gentle vortexing. The resulting solution was clear and homogenous. The solution was sonicated for 10 minutes to remove bubbles. Films were cross-linked by sandwiching the hybrid solution between two quartz plates separated by spacers and exposing the film to 354-nm UV light (Spectrolinker XL-1000, Spectronics Corp.) for 90 seconds. The films were then dried under vacuum at 25 °C overnight to remove any residual solvent.

Membrane Characterization. Volume and mass loading of the XLPEG/silica composites was verified gravimetrically using a Q5000IR Thermogravimetric Analyzer (TA instruments). Hybrid films were decomposed under atmospheric conditions to 600 °C at 10 °C/min The conversion of mass to volume loading was done using values of 1.18 g/cm^3, 2.1 g/cm^3, and 2.2 g/cm^3 for the density of XLPEG, Stöber silica, and Ludox SM silica respectively as follows.[93–95]

$$\phi_{SiO2} = \frac{\frac{\omega_F}{\rho_F}}{\frac{\omega_F}{\rho_F} + \frac{\omega_P}{\rho_P}} \qquad (2.1)$$

ϕ_{SiO2} is the volume fraction of the silica nanoparticles. ω_F and ω_p are the mass fraction of silica nanoparticles and polymer respectively, while ρ_F and ρ_p are their respective densities. Cross-sectional images of the hybrid films were acquired with a Zeiss Gemini Ultra-55 Analytical Scanning Electron Microscope using a beam energy of 5 keV. Prior to imaging, the films were cryofractured after immersion in liquid N_2 to provide a clean surface. Density measurements of the bulk hybrid films were performed using hydrostatic weighing and a density determination kit (Mettler Toledo). Heptane was used as the secondary liquid. A Q200 differential scanning calorimeter (TA instruments) was used to determine glass transition temperatures and obtain thermograms surrounding the glass transition region, scanning from -90 °C to 0 °C at a heating rate of 20 °C /min. Density measurements of the bulk dense hybrid and pure polymer membranes were conducted using a hydrostatic weighing method (Mettler Toledo). The density of the membranes, ρ_m were calculated as follows:

$$\rho_m = \frac{M_A}{M_A - M_L}\rho_L$$

where M_A is the weight of the membrane in air, M_L is the weight in the auxiliary liquid, and ρ_L is the density of the auxiliary liquid. In this case, heptane was chosen as the auxiliary liquid as it does not readily swell the polymer.

The effective medium density, ρ_{approx}, of the hybrid membranes is calculated as follows:

$$\rho_{approx} = \phi_{SiO2}\rho_{SiO2} + (1 - \phi_{SiO2})\rho_p$$

where ϕ_{SiO2} is the volume fraction of the silica nanoparticles, ρ_{SiO2} is the density of the silica (2.1 or 2.2 gm/cm^3 for Stöber synthesized silica or Ludox SM silica, respectively), and ρ_p is the density of the polymer, 1.18 g/cm^3. XRD patterns of the hybrid membranes were taken with a Bruker D8-Advance X-ray diffractometer equipped with a GADDS area detector

operating at the Cu Kα wavelength, 1.54 Å. Peaks were fitting using Multi-peak Fit 2 package.

Gas Permeability Measurements. Pure gas permeability of XLPEG/silica composite membranes for H_2, N_2, CH_4, and CO_2 were measured using a custom built constant volume/variable pressure apparatus based upon the work of Lin and coworkers.[94,96] The films were masked with brass discs to accurately define an area where gas transport could occur. Thicknesses of films were measured and found to be approximately 90 to 120 μm. Prior to testing, the films were degassed within the apparatus. A fixed pressure (between 3-16 atm) was applied to the upstream side of the membrane, while the gas flux was recorded as a steady-state pressure rise downstream of the membrane. Permeability values were calculated as follows:

$$P = \frac{V_D l}{p_2 ART}\left(\frac{dp_1}{dt}\right) \qquad (2.2)$$

where V_D is the downstream volume (cm^3), l is the film thickness (cm), p_2 is the upstream pressure (cmHg), A is the surface area of the film (cm^2), R is the gas constant, T is the absolute temperature (K), and dp_1/dt steady state pressure rise downstream at fixed upstream pressure (cmHg/sec). The measurements were obtained under isothermal conditions at 308 K

2.3 Results and Discussion

2.3.1 Silica Nanoparticle Characterization

Silica nanoparticles have been commonly used in hybrid membranes in the form of fumed silica. [51,56,97] However, the polydisperity of fumed silica, a result of large poorly controlled inhomogeneous aggregates of particles exceeding 100 nm, hinders more fundamental studies of microscopic interactions in hybrid system. Therefore, it was critical to control the shape and size of silica for our study. Following the method proposed originally by Stöber, we chemically synthesized uniform silica nanoparticles greater than 30 nm in diameter. Stöber-synthesized nanoparticles of less than 30 nm in diameter are more irregularly shaped and were not used in this study. Instead, I used Ludox SM silica nanoparticles for the smallest particle size studied. Due to the alkaline conditions present in native Ludox SM dispersion, the direct addition of the polymer resulted in heavy gelation. Consequently, it was necessary to transfer the Ludox SM particles into an organic alcohol. Silica nanoparticles were imaged through transmission electron microscopy as seen in **Figure 2.1**. The particles are spherical with low polydispersity, and the particle diameters were calculated to be 130 ± 15, 41 ± 3.8, and 12 ± 1.2 nm. Hereafter, the nanoparticles will be referred to only by their size.

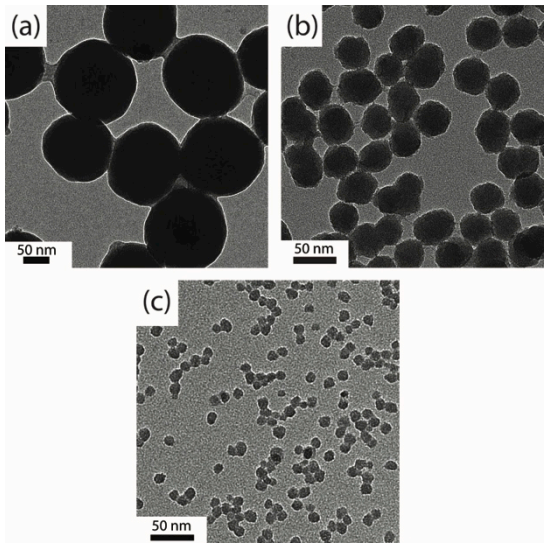

Figure 2.1. TEM images of silica nanoparticles from isopropanol and representative XLPEG/silica nanocomposite film. (a) Stöber silica (130 nm), (b) Stöber silica (41 nm), and (c) Ludox SM silica (12 nm)

2.3.2 Hybrid Membrane Characterization

Hybrid organic/inorganic membranes consisting of silica nanoparticles of various diameters dispersed in a cross-linked poly(ethylene glycol) matrix were successfully prepared through UV photopolymerization. Silica loading in films ranges from 0 vol% up to 30 vol% and was confirmed through TGA experiments (**Figure 2.2**). Values of silica volume percent, ϕ_{SiO2}, are presented in **Table 2.1**. **Figure 2.3(a)** shows a representative image of a hybrid XLPEG/silica film containing 19 vol% 12-nm silica nanoparticles. There was no appearance of pinhole defects and film quality is easily reproducible from sample-to-sample. All films studied were optically transparent, suggesting macroscale homogeneity of the composite. If heterogeneity or phase segregation of the hybrid were present, it would be readily observable as a consequence of light scattering off of macroscale particulate aggregates. Thus, the high transparency of all the films studied indicates that the inorganic nanoparticles are homogenously well-dispersed within the polymer. Additionally, the bulk density measurements of the hybrid films are consistent with effective medium density calculations and do not suggest the presence of macroscale defects, Table 2.1 and **Figure 2.4**.

Table 2.1. Properties of Cross-Linked Poly (Ethylene Glycol) Containing Silica Nanoparticle Composites.

Polymer	Silica Size (nm)	$\phi_{SiO2}\times100\%$	Density (g/cm^3)	T_g (°C)
XLPEG	-	0	1.182 ± 0.001	-39
XLPEG	130 ± 6.5	6.9	1.265 ± 0.006	-38
XLPEG	130 ± 6.5	17	1.351 ± 0.008	-38
XLPEG	130 ± 6.5	27	1.434 ± 0.003	-38
XLPEG	41 ± 3.9	7.9	1.258 ± 0.006	-39
XLPEG	41 ± 3.9	17	1.348 ± 0.003	-39
XLPEG	41 ± 3.9	28	1.441 ± 0.004	-40
XLPEG	12 ± 1.2	7.8	1.279 ± 0.004	-39
XLPEG	12 ± 1.2	19	1.372 ± 0.005	-36
XLPEG	12 ± 1.2	30	1.498 ± 0.007	-39

Cross-sectional scanning electron microscopy (SEM) images of the pure XLPEG and hybrid membranes were collected to examine microscopic homogeneity of the films and are presented in **Figures 2.3(b)-(k)**. The pure XLPEG film, as seen in Figure 2.3(b), is highly uniform, non-porous, and consistent with the macroscale observations of a defect-free film. Hybrid films containing 130-nm silica nanoparticles are presented in Figures 2.3(c)-(e) in order of increasing volume loading. The silica nanoparticles are easily discernable from the polymer and uniformly distributed throughout the film, as evinced by lack of light scattering. The nanoparticles are randomly distributed at the lowest loading, 6.9 vol%, and begin to undergo a transition to a close-packed configuration at the highest loading, 27

vol%. Interestingly, the SEM images reveal a sub-layer of silica nanoparticles confined below a layer of polymer. The homogeneity of the nanoparticles in the sub-layer further confirms the homogeneity of the hybrid membrane. Figures 2.3(f)-(h) show hybrid XLPEG/silica membranes containing 41-nm silica nanoparticles. The nanoparticles are similarly homogenously distributed throughout the polymer at all volume loadings. Finally, hybrid membranes containing 12-nm silica nanoparticles are presented in Figures 2.3(i)-(k). While the resolution limits of the SEM make it difficult to resolve individual particles, the film is visibly homogenous and defect-free, and no signs of micro-scale phase segregation or aggregates were observed.

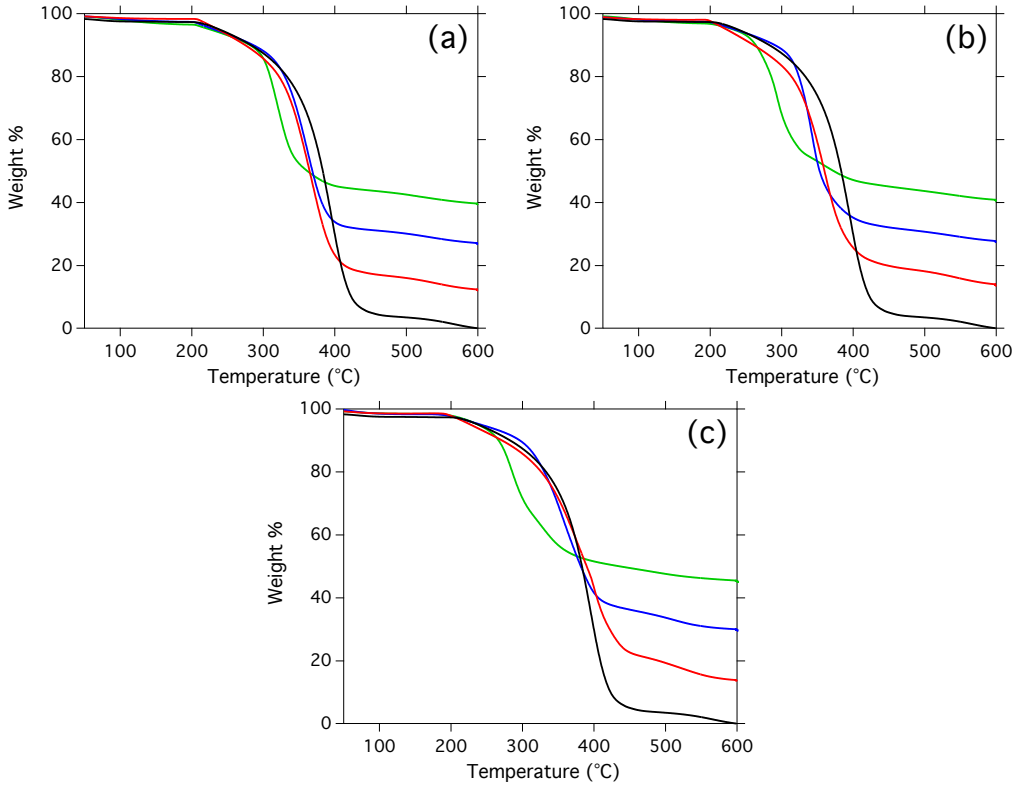

Figure 2.2. Thermogravimetric analysis decomposition curves of XLPEG/silica. a) 130 nm silica in XLPEG, b) 41 nm silica in XLPEG, and c) 12 nm silica in XLPEG.

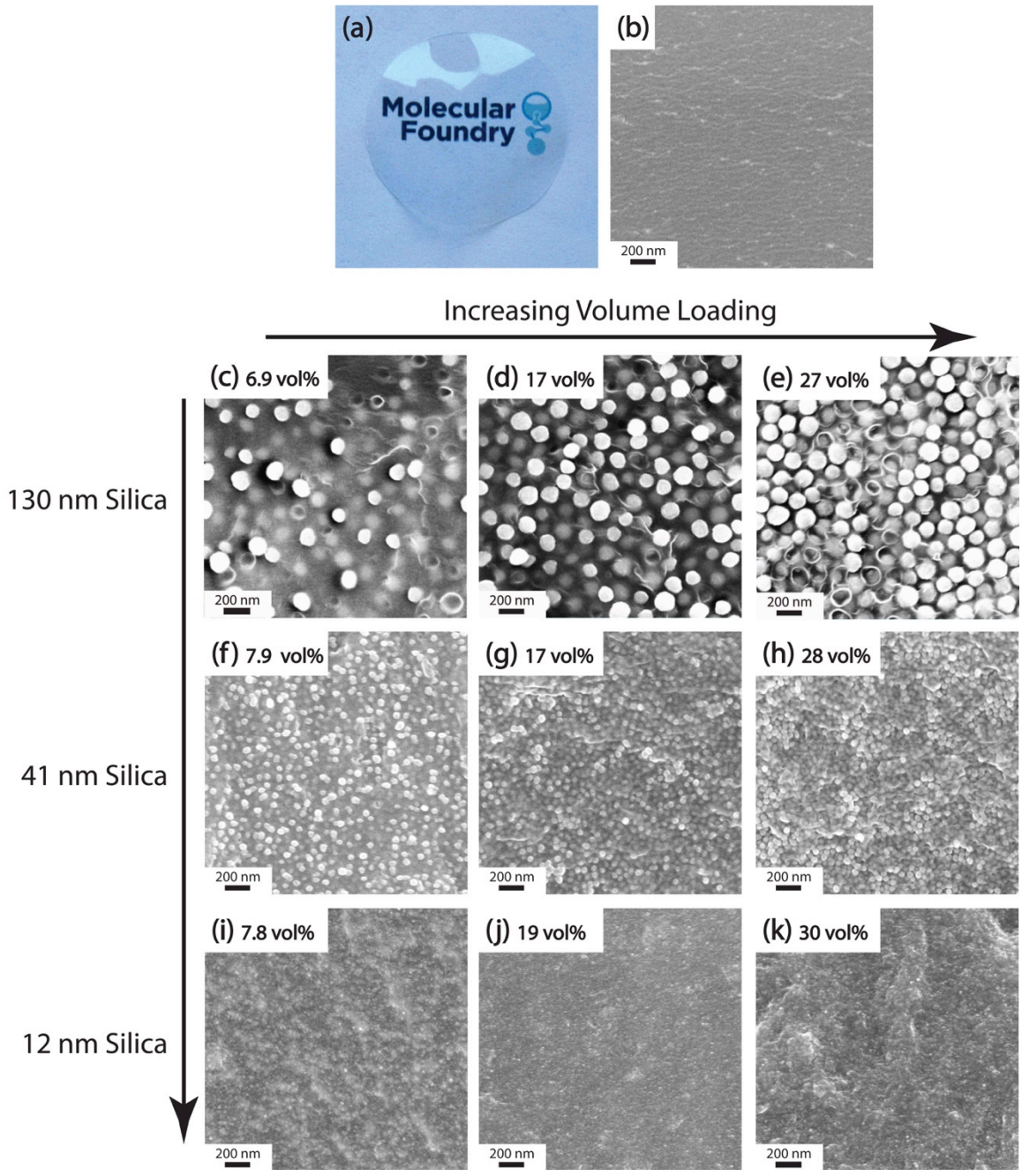

Figure 2.3. (a) Image of hybrid XLPEG/silica film containing 19 vol% 12-nm nanoparticles. (b) SEM cross-section image of pure XLPEG film and (c)-(k) SEM cross-section images of hybrid XLPEG/silica films. (c)-(e) 109-nm hybrid films; (f)-(h) 38-nm hybrid films; (i)-(k) 12-nm hybrid films. Images are of increasing silica loading from left to right. The silica nanoparticles in all hybrid membranes appear homogenously dispersed.

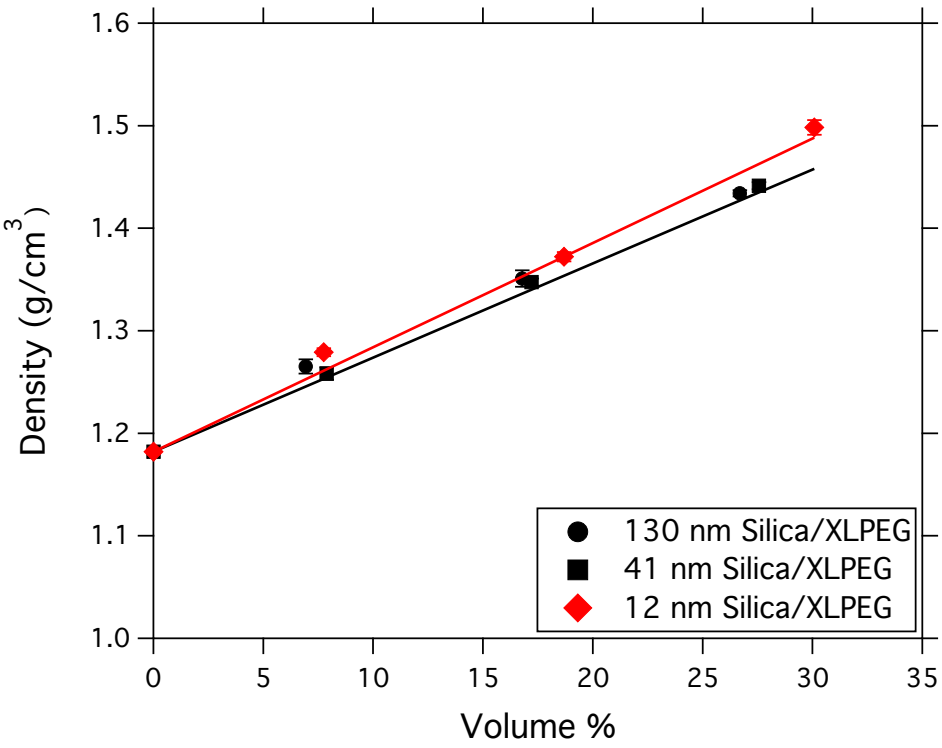

Figure 2.4. Density of XLPEG/Silica nanocomposites versus volume fraction of silica at 20 °C. The solid lines are predicted additive density. The red line represents Ludox silica composites, and the black line Stöber silica composites.

2.3.3 Understanding Interfacial Interactions

In addition to the synthetic control of the inorganic phase, the manner in which the inorganic species interacts with the polymer is critical, as it will greatly affect gas transport through the membrane. Examining the glass transition temperature, T_g, of the polymer can shed light on the interaction between the polymer and inorganic phase thereby providing insight on the polymer dynamics. Differential scanning calorimetry is a useful technique to elucidate changes in polymer dynamics upon the incorporation of a secondary inorganic phase.[79–81] In hybrid systems, the T_g of the polymer has been observed to underdo three modes of perturbations upon the introduction of an inorganic phase: a positive shift,[48,80,98] negative shift,[79,80,99] and broadening.[81,100] When T_g shifts to higher temperatures, it corresponds to a glassier polymer due to favorable interactions with the inorganic phase that reduce segmental chain mobility. Alternatively, T_g can shift to lower temperatures due to unfavorable interactions with the inorganic phase.

Interestingly, I found that the T_g of all hybrid membranes in our study are similar to pure XLPEG, as presented in Table 1 and seen in Figure 3 insets. The absence of T_g shifts is common in "strong" polymers; polymer strength is characterized by its fragility.[81,82] Polymer fragility is understood as the rate at which cooperative segmental dynamics of glass-forming liquids changes as T_g is approached. XLPEG has a fragility index of 23, which is well below the general threshold of 50, where cooperativity between polymer chains is low, and thereby considered strong.[82–84] Thus, the segmental motion of XLPEG chains

should not be dependent on the motion of neighboring chains. Instead, I would expect the polymer to display a distribution of segmental mobility behavior that would be revealed in the broadening of the T_g region as the polymer transitions from a glass to a rubber.

In **Figure 2.5**, DSC thermograms of hybrid XLPEG/silica membranes are plotted and compared to that of the pure homopolymer, XLPEG. Each thermogram is shifted laterally by its respective T_g, and the heat flow has been normalized to the heat flow difference between the rubbery and glassy state to compare between films. Thermograms of hybrid membranes containing 130-nm nanoparticles closely match the thermal behavior of the pure homopolymer, as seen in Figure 2.5(a). There is no apparent broadening at any volume loading of the 130-nm nanoparticles. A similar observation is noted in the hybrids containing 41-nm nanoparticles at loadings of 7.9 and 17 vol%, as seen in Figure 2.5(b). At the highest loading, 28 vol%, the thermogram begins to broaden at temperatures above the T_g. Furthermore, for hybrid membranes containing 12-nm nanoparticles, Figure 2.5(c) shows systematic curve broadening of the thermograms as the loading is increased from 7.8 vol% to 30 vol%. Through our well-controlled system, I can see that the size of silica nanoparticles plays an important role in the interaction between of the polymer and silica.
To understand the magnitude of the observed broadening of the thermograms, I attempt to relate the broadening to surface area to volume, SA/V, ratio of the silica nanoparticles. I expect surface area of the nanoparticles to be a significant contributor to interfacial interactions and total surface area of silica irrespective of size would present similar broadening behavior. Nitrogen adsorption at 77 K was used to determine the surface area of the silica nanoparticles. BET surface area of 130, 41, and 12 nm particles was found to be 24 ± 0.2, 170 ± 1.4, and 293 ± 2.1 m^2/g, respectively, or 53, 365, and 638 m^2/m^3, respectively, on a volumetric basis. Comparing these measured values to estimated SA/V for spherical particles of equivalent size (**Table 2.2**), I find that the SA/V for 130-nm and 12-nm silica match closely to the estimates, while 41-nm silica is higher than estimates. The higher than expected SA/V of 41 nm nanoparticles can be a result of surface roughness, as seen in Figure 2.1(b), or particle porosity.[93]

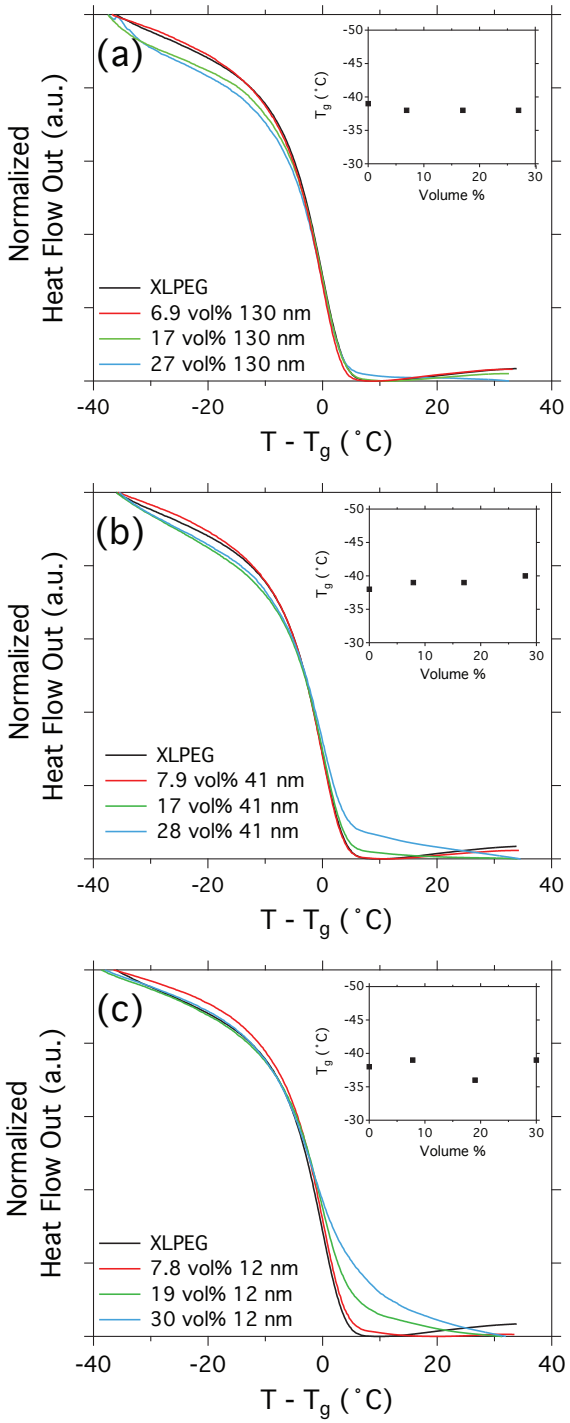

Figure 2.5. DSC thermograms of XLPEG/Silica composite films containing (a) 130 nm silica nanoparticles, (b) 41 nm silica nanoparticles, and (c) 12 nm silica nanoparticles. The thermograms are first run scans, normalized to the maximum heat flow of each respective scan, and shifted by their respective $T_{g\,g}$, listed in Table 1. Insets show T_g plotted against volume percent.

Table 2.2. Total surface area per volume of composite films of a given volume percent and nanoparticle size.

	130 nm	41 nm	12 nm
ϕ_{SiO2}× (100%)	SA/V m^2 (silica)/m^3 (composite)		
Spherical Est. (100)	45	140	640
100	52.5	365	638
28	14.7	102	179
18	9.5	65.6	114
7	3.7	25.5	44.7
1	-	3.6	6.4
0.5	-	-	3.2

If surface area were the primary contributor to the observed broadening, then similar total surface areas between nanoparticles of different sizes would exhibit similar thermal behaviors. Hybrid membranes containing 28 vol% 41-nm silica and 19 vol% 12-nm silica were chosen because of similar total surface area per unit volume of film, 102 and 114 m^2/m^3, respectively. The thermograms are plotted in **Figure 2.6** and compared to the pure homopolymer. The thermal transitions of these well-controlled hybrid membranes match closely. This indicates that the polymer dynamics behave similarly between these two hybrid membranes and the effect of silica on polymer dynamics is dependent on nanoparticle size and loading. Having precise control of the nanoparticle size and dispersion is an important criteria in making this comparison. I did not include a comparison with 130-nm nanoparticles because even at 100% loading, I would expect there to be no broadening at those total surface area values (refer to Table 2.2 for SA/V comparisons in hybrid membranes).

The broadening of the DSC thermograms is focused in the temperature region above the T_g of the hybrid membranes. This is due to favorable interactions between the ether oxygen in poly(ethylene glycol) and the surface hydroxyl groups found on the silica nanoparticles.[48,101] A favorable interaction results in a decrease in the segmental chain mobility of the polymer due to adsorption onto the surface of the nanoparticle. Thus, the polymer at the interface will become more rigid and display a higher T_g than the pure homopolymer. Similar observation of polymer chain modification in two-phase materials has been observed with X-ray diffraction where d-spacing between polymer chains decreases as content of the secondary phase increases.[102] I see a similar phenomenon in our membranes, most prominently in membranes containing 19 and 30 vol% 12 nm silica nanoparticles (**Figure 2.7**). However, due to the "strength" of XLPEG and lack of cooperative segmental mobility, the polymer exhibits a distribution of segmental mobility leading to a broadening above T_g. The resulting hybrid membranes, which display broadening behavior, are characteristically more "glassy" than the pure homopolymer.

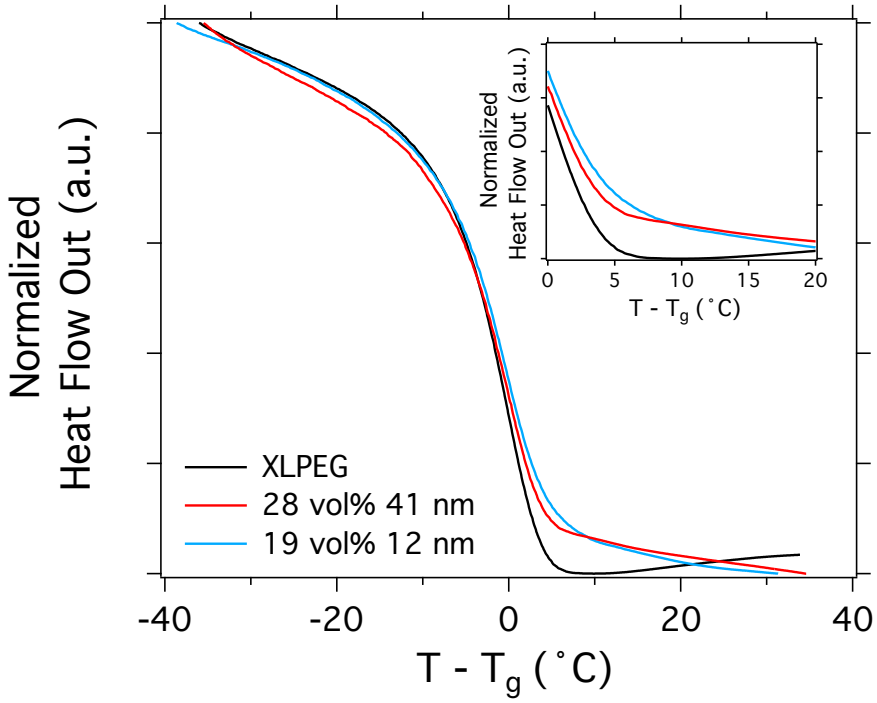

Figure 2.6. Comparison of DSC thermograms at equivalent total silica surface area. Pure XLPEG (black), 28 vol% 41 nm silica (red), 19 vol% 12 nm silica (blue).

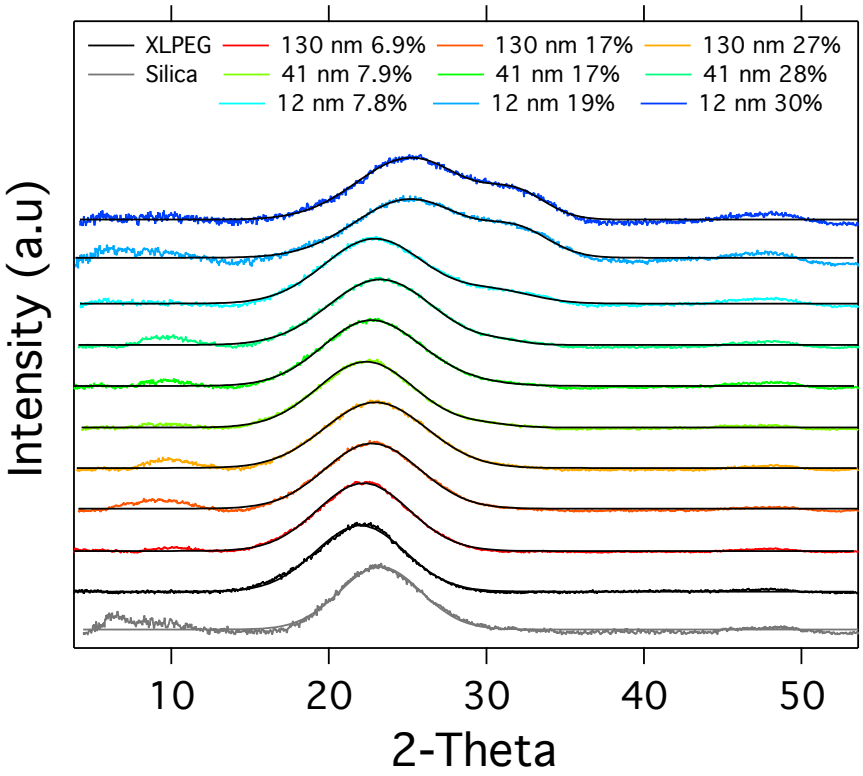

Figure 2.7. XRD patterns of hybrid XLPEG/silica nanoparticle membranes. Each pattern was fitted either to single or multiple Gaussian functions. XLPEG exhibits a broad amorphous peak center at 22° 2-theta. As nanoparticle loading increases within size classification, the peak center undergoes a shift to higher 2-theta and in the appearance of a secondary peak at higher 2-theta. This is most clearly seen in 12 nm silica nanoparticle membranes. 19 and 30 vol% 12 nm hybrids show a disappearance of peak at 22° and the appearance of to peaks at 25.2° and 32°. These peaks do not correlate to amorphous silica which has a broad peak centered around 23.2°. The location of these peaks suggests that at these loadings the segments of the polymer have indeed become more rigid and closely packed. The interchain d-spacing of the polymer has decreased from 4.05 Å to 3.56 Å and 2.80 Å.

2.3.4 Gas Permeability Measurements

Pure gas permeability measurements of H_2, N_2, CH_4, and CO_2 as a function of silica volume loadings at 35 °C and 6 atm are plotted in **Figure 2.8** for each nanoparticle size. In general, for all sizes, permeability decreases as nanoparticle loading is increased. Permeability through heterogeneous systems is frequently described by effective medium approximations such as Maxwell's model.[77] For a system containing impermeable non-interacting particles distributed within a polymer matrix, the composite permeability, P_c, can be described by matrix, the composite permeability, P_c, can be described by Equation 2.3,

$$P_c = P\frac{2-2\phi_{SiO_2}}{2+\phi_{SiO_2}} \qquad (2.3)$$

where P is the permeability of the pure polymer, and ϕ_f is the volume fraction of the dispersed impermeable filler phase.

The simplicity of Maxwell's model allows it to be widely used to understand gas transport through many types of hybrid membranes, but this model and other effective medium approximations are not sensitive to variations in the dispersed phase shape and size, which I have shown to contribute to differences in polymer dynamics. Permeability through hybrid membranes containing 130- and 41-nm silica can be mostly captured by Maxwell's model, but permeability through 12-nm silica hybrid membranes is consistently lower than predicted by the model. Thus, permeability through our well-controlled hybrid membranes is influenced by not only the loading of the inorganic phase, as understood by Maxwell's model, but also by the size of the nanoparticles. This is not predicted by Maxwell's model, but is clearly observed in the data.

To quantify the deviation from Maxwell's model of the hybrid membranes, we have plotted the permeability data as relative permeability on the basis of Maxwell's predicted permeability values in **Figure 2.9**. The predicted permeability values from Maxwell's model are plotted as a straight line crossing through the zero point. Data above Maxwell's model are measured permeabilities that deviate positively, and data below the line indicate negative deviations. N_2, CH_4, and CO_2 permeabilities for hybrid membranes containing 130- and 41-nm silica are consistent to Maxwell's model because of the low level of interaction between the polymer and silica as observed in the DSC measurements. However, H_2 permeability has a positive deviation from the model, especially at the highest nanoparticle loading. The H_2 permeabilities are 37% and 27% higher than Maxwell's prediction for the 130- and 41-nm hybrid membranes, respectively. Although the permeability for H_2 is significantly higher than predicted by the model, it is still a lower absolute permeability than the pure polymer.

I speculate that the increase in H_2 permeability in the 130- and 41-nm silica hybrid membranes with respect to Maxwell's prediction may arise for one of two possible reasons. First, at high nanoparticle loadings, the polymer may not be able to completely infiltrate the space between nanoparticles and result in the formation of voids.[103] However, the density data does not support this explanation because I would expect to see densities lower than effective medium predictions. Second, voids may occur at the silica/polymer interface due to chemical incompatibility or surface roughness.[104] As a result, "nanogaps" may form in regions where the polymer does not fully wet the silica. These nanogaps may only affect the permeability of H_2 because of its significantly smaller kinetic diameter (2.89 Å vs. CO_2 (3.3 Å), N_2 (3.64 Å), and CH_4 (3.8 Å)).[23] Furthermore, the H_2 permeability is only affected at higher loadings for 130- and 41-nm hybrid membranes, which is consistent with this explanation. Unfortunately, it is not trivial to determine the presence of nanogaps from our current analysis and so it will not be investigated further at this time.

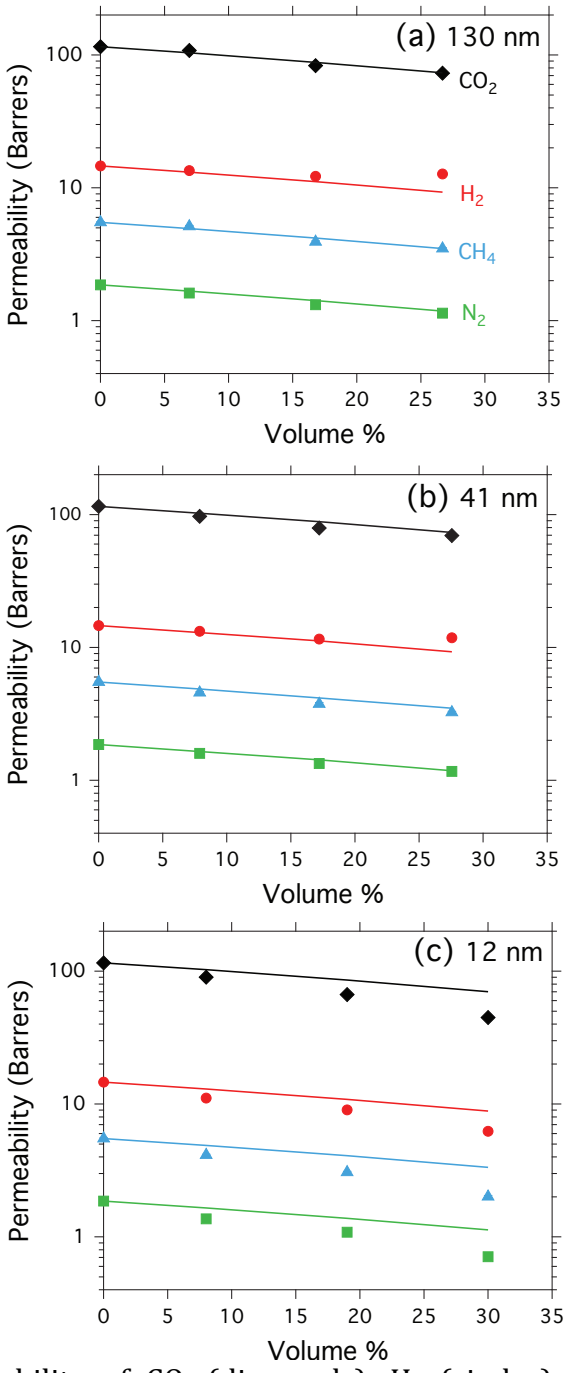

Figure 2.8. Gas permeability of CO_2 (diamonds), H_2 (circles), CH_4, (triangles) and N_2 (squares) for XLPEG/silica nanocomposites containing (a) 130 nm nanoparticles, (b) 41 nm nanoparticles, and (c) 12 nm nanoparticles at 6 atm and 35 °C. The solid lines represent the permeability prediction from Maxwell Model (eqn. 2.3).

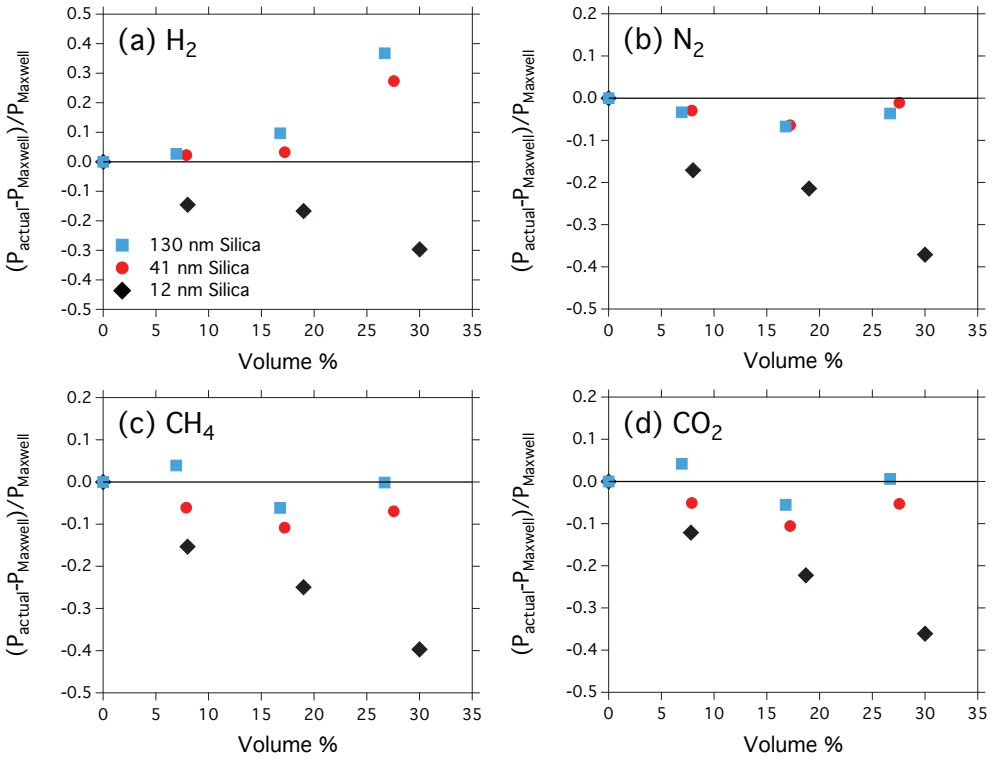

Figure 2.9. Relative permeability deviation of XLPEG/silica nanocomposites from Maxwell prediction of gas permeability at 6 atm and 35 °C. 109 nm nanoparticles (squares), 38 nm nanoparticles (circles), and 12 nm nanoparticles (diamonds). (a) H_2, (b) N_2, (c) CH_4, and (d) CO_2. P_{actual} is measured permeability and $P_{Maxwell}$ is the calculated permeability of the composite from Maxwell's model.

Hybrid membranes containing 12-nm silica exhibit permeabilities that increasingly deviate from Maxwell's prediction as volume loading is increased, as seen in Figure 6. Interestingly, at the highest loading of 30 vol%, the magnitude of deviation follows the order of kinetic diameter of gases, $H_2 < CO_2 < N_2 < CH_4$. The permeabilities for H_2, CO_2, N_2, and CH_4 are 29%, 36%, 37%, and 40% lower than Maxwell's prediction, respectively. Furthermore, the permeability of the 30 vol% 12-nm silica hybrid membranes is approximately 60% lower for all gases than pure XLPEG permeability. The much lower permeability of hybrid membranes containing 12-nm silica rather than 41- or 130-nm silica was expected due to the increased interfacial interactions arising from significantly higher SA/V values of 12-nm silica and total surface area available for interaction in 12-nm silica hybrid membranes. The interactions, as discussed earlier, led to an overall polymer in the hybrid that is glassier than the pure polymer system. The reduction in segmental chain mobility will decrease the diffusion of gas molecules due to a higher activation energy required to undergo diffusive jumps. Furthermore, when the loading of 12-nm silica increases, a larger fraction of polymer will have reduced chain mobility, which will lead to a decrease in the gas permeability property of the polymer that is not captured by Maxwell's model.

I have compared our permeability measurements to reports in literature of gas transport through XLPEG/silica membranes. XLPEG nanocomposites containing fumed silica with primary particle diameter of 12 nm have been reported.[105,106] The addition of

methacrylate-terminated fumed silica up to 10 wt% loading showed permeability values following Maxwell's model. Our composites, at a similar loading of 13 wt% (7.8 vol%) and particles size, have permeability values on average 14% lower than Maxwell. However, in those reports, the dispersion of fumed silica was not homogenous over length scales of 100 nm, whereas our hybrid XLPEG/silica membranes are homogeneous for length scales exceeding one micron. The fumed silica had a reported surface area of 150 ± 25 m^2/g, which is much lower than the 12-nm silica and closer to the 41-nm silica used in this study. From our results, given the reported surface area and volume loading of fumed silica, I would not anticipate to observe any deviation from Maxwell's model in their results. The total surface area of silica at 7.8 vol% is not enough to force the XLPEG to undergo significant and relevant changes in polymer dynamics and would not have any additional affect in gas transport other than predicted in Maxwell's model.

2.3.5 Gas Selectivity

Selectivity of CO_2 over H_2, N_2, and CH_4 for our XLPEG/silica membranes is presented in **Figure 2.10**. CO_2/N_2 and CO_2/CH_4 values remained unchanged relative to selectivity values observed in pure XLPEG. The relatively constant selectivity of CO_2/N_2 and CO_2/CH_4 suggests that the solution-diffusion mechanism of polymer gas transport is still the dominant mechanism in our hybrid membranes. Furthermore, it indicates that there is no specific interaction between the silica nanoparticles and gases tested. However, for CO_2/H_2, the selectivity decreases as silica loading increases for all nanoparticle sizes studied. In 130- and 41-nm silica hybrid membranes, CO_2/H_2 selectivity is lower than for the pure polymer membrane due to higher H_2 permeability than predicted by Maxwell. In 12-nm silica hybrid membranes, lower CO_2/H_2 selectivity is a result of smaller H_2 permeability reductions than CO_2, N_2, or CH_4. This could be due to the smaller kinetic diameter of H_2 molecules, which are not subject to the same constraints of segmental chain mobility of larger molecules.

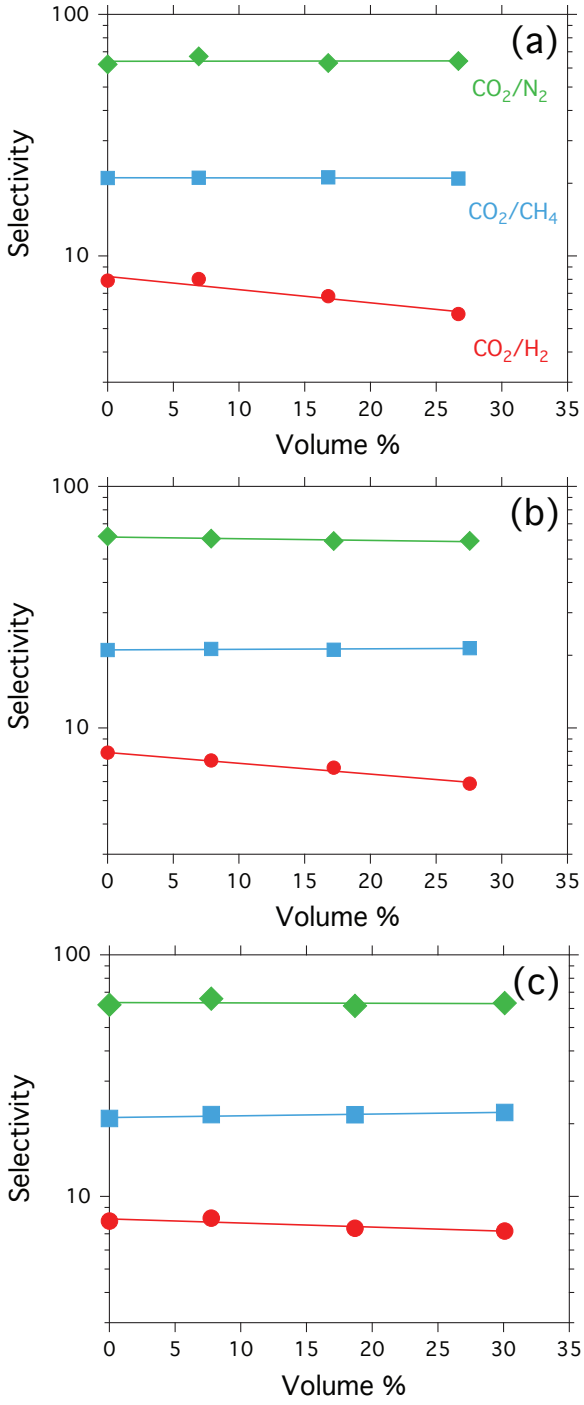

Figure 2.10. Gas selectivity of CO_2/N_2 (diamonds), CO_2/CO_4 (squares), CO_2/H_2 (circles) for XLPEG/silica nanocomposites containing (a) 130 nm nanoparticles, (b) 41 nm nanoparticles, and (c) 12 nm nanoparticles at 6 atm and 35 °C. The solid lines serve as guides to the eye.

2.4 Conclusions

We have developed a well-controlled model system of hybrid XLPEG/silica membranes with uniformly dispersed nanoparticles to understand the effects of polymer/nanoparticle interactions on gas transport. The nanoparticles studied span over an order of magnitude in size and are homogeneously distributed throughout the membrane at all loadings explored. The incorporation of silica nanoparticles into the polymer matrix can lead to a reduction of segmental chain mobility of the polymer, which was manifested as a broadening of the T_g in DSC measurements, because of the favorable interaction between the hydroxyl groups on silica and ether oxygen in the XLPEG. Hybrid membranes with low surface area to volume ratios and minor interfacial interactions (e.g. those with 130-nm and 41-nm silica nanoparticles) exhibited permeability properties that can be understood by applying effective medium approximations such as Maxwell's model. However, hybrid membranes displaying significantly increased interfacial interactions due to increased surface area (e.g. those with 12-nm silica nanoparticles) exhibited a decrease in gas permeability that significantly deviated from Maxwell's model, due to a broad reduction in segmental chain mobility, especially at higher loadings.

Furthermore, the selectivity of the hybrid membranes remained relatively constant indicating weak interactions between the silica nanoparticles and gases tested. Additionally, the development of a tunable system provides a pathway for future work towards understanding how I can control surface chemistry and interactions with the polymer to enhance gas transport properties of hybrid organic/inorganic membranes.

2.5 Acknowledgements

The authors would like to thank Dr. David Sanders, Kevin Stevens, and Prof. Bryan McCloskey for their discussion and resources in the field of gas transport. Work at the Molecular Foundry was supported by the Office of Science, Office of Basic Energy Sciences, of the U.S. Department of Energy under Contract No. DE-ACO2-05CH11231. I would also like to acknowledge Dr. Jason Forster for his assistance. N. Su was supported by the Department of Defense (DoD) through the National Defense Science & Engineering Graduate Fellowship Program.

2.6 Supporting Information

Supporting information for this chapter can be found in Appendix A.1.

Chapter 3. Enhancing separation and mechanical performance of hybrid membranes through nanoparticle surface modification

Adapted from "Enhancing separation and mechanical performance of hybrid membranes through nanoparticle surface modification." N.C. Su, H.G. Buss, B.D. McCloskey, and J.J. Urban. *ACS Macro Letters.* 2015, 4, 1239, DOI: 10.1021/acsmacrolett.5b00681. Reproduced with permission from *ACS Macro Letters.*

Membranes with selective gas transport properties and good mechanical integrity are increasingly desired to replace current energy intensive approaches to gas separation. Here, I report on the dual enhancement of transport and mechanical properties of hybrid cross-linked poly(ethylene glycol) membranes with aminopropyl-modified silica nanoparticles. In the previous chapter, I analyzed the effect of size, and I build from the model platform to investigate surface functionalization effects. CO_2 permeability in hybrid membranes exceeds what can be predicted by Maxwell's equation and surpasses values of the pure polymer. Furthermore, dynamic mechanical and Thermogravimetric analyses reveal increases in both the storage modulus and thermal stability in hybrid membranes, with respect to silica nanoparticle loading.

3.1 Introduction

Membranes have become increasingly important in gas separation processes with applications ranging from carbon capture to chemical production because of their relative ease of operation and efficiency.[8,21] Current research in membranes is concentrated on polymeric systems due to ease of processability, which enables large-scale commercialization. While significant progress has been made towards improving the performance of these membranes, they suffer from an empirical trade-off between permeability and selectivity, which has thus far prevented the development of high performance membranes.[28,87]

Hybrid membranes, which typically consist of inorganic nanomaterials dispersed within a continuous polymer matrix, present an opportunity to overcome the traditional limitations of polymers and optimize separation performance.[40] Membranes derived solely from inorganic materials often possess better transport properties than polymers. For instance, the rigid nature of porous inorganic materials allows significantly better molecular size discrimination.[43,50] Furthermore, inorganic materials exhibit much higher chemical selectivity.[60,107] Unfortunately, the separation performance and commercial scalability of inorganics are ultimately limited by material brittleness. Thus, hybrid membranes can combine the separation properties of inorganics with the processability of polymers and provide additional avenues to improve performance. In addition, hybrid membranes can realize new properties and functionalities not found in pure component systems through synergistic enhancements.[41] For example, mundane materials such as silica can improve transport properties through cooperative changes in polymer structure and dynamics.[51,55,97] Inorganic materials can also increase the mechanical and thermal stability and robustness of a polymer membrane if favorable interphase interactions exist.[52,108] However, improving mechanical stability often comes at a cost to transport properties. Favorable interphase interactions can lead to rigidification of polymer chains near the interface and increase both the glass transition temperature (T_g) of the polymer and activation energy for molecular diffusion, thereby decreasing gas permeability.[48,108] The degree of influence from these interactions can depend on the inorganic dispersant size and volumetric loading.[17] Contrastingly, interactions that are weak can result in non-selective transport pathways due to void formation or mechanical instability.[103] Therefore, it is critical to select inorganic materials, which exhibit optimal interfacial interactions and maximize gas separation performance.

Here, I report on the design of hybrid membranes that achieve simultaneous improvements in transport and mechanical properties through appropriate surface modification of the inorganic phase. The hybrid membranes are composed of cross-linked polyethylene glycol (XLPEG) and surface-modified silica nanoparticles. I test the transport of gases, which are relevant to carbon capture applications (e.g. carbon dioxide, methane, and nitrogen). The silica nanoparticles used in this study have an average diameter of 12 nm. Native silica nanoparticles are typically terminated with hydroxyl groups, whose interaction with XLPEG has been shown to be detrimental to gas transport.[109] Informed by this, I explore the effects on membrane properties when the hydroxyl groups are replaced with aminopropyl

ligands through silanization. I expect that the amine group will not interact too strongly or too weakly with the ether group in XLPEG, thereby avoiding adverse effects on transport properties. Furthermore, the incorporation of amines can increase the solubility of carbon dioxide, helping to further drive transport performance increases. Recent literature has also supported the use of amines on inorganic surfaces in hybrid membranes as it can serve a dual purpose of adding facilitated transport channels and improve interfacial compatibility with the polymer.[69,85,110–114] Hybrid membranes systematically prepared with a range of different silica loadings from 0 vol% to 16 vol%. XLPEG is prepared through a photopolymerization method using poly (ethylene glycol) diacrylate (700MW) and 2,2-dimethoxy-2-phenylacetophenone as the photoinitiator.[109]

3.2 Experimental Procedure

Silica Surface Modification and Characterization. All chemicals were purchased from Sigma Aldrich. Ludox SM silica nanoparticles are initially transferred from an aqueous solution into an alcohol by mixing Ludox SM with 60:1 ratio of ethanol:nitric acid followed by centrifugation. The nanoparticles are washed again two more times with ethanol and the final dispersed in isopropanol.

Silica silanization is conducted with aminopropyl triethoxysilane (99%) (APTES). Silica nanoparticles are first diluted such that the concentration is below 10 mg/ml in isopropanol. Ammonia hydroxide and water are added to the mixture in a 1:3600 and 1:6000 volumetric ratios, respectively. The mixture is heated to reflux and APTES is injected such that the concentration is equal to ~7 monolayer molar equivalent coverage on total silica surface in reaction mixture assuming 4 hydroxyl groups/nm^2.[115] The solution is kept under reflux for at least 16 hours, cooled to room temperature, and purified using centrifugation and redispersion in isopropanol. Ninhydrin testing was conducted with a 0.1M solution in ethanol. 10 µL was dropped into 1 ml of silica-APTES and gently shaken.

CO_2 adsorption on silica-APTES nanoparticles is conducted on a Q5000IR Thermogravimetric Analyzer (TA Instruments). The nanoparticles are dried within the instrument at 150 °C for a period of two hours under argon before cooling to the experimental temperature of 40 °C. CO_2 and argon are cycled in 90 minute intervals for 3 times. Nitrogen adsorption isotherms were collected at 77 K using a Tristar II Surface Area Analyzer (Micromeritics). Surface area values are calculated following Brunauer–Emmet–Teller method over a relative pressure range, p/po, of 0.05 to 0.25.

Membrane Fabrication and Characterization. Neat XLPEG and hybrid membranes are fabricated following adapted procedures[109]. A polymer solution containing poly (ethylene glycol) diacrylate (700 MW) and 0.1 wt % of the initiator 2 are mixed together until the initiator is completely dissolved. Silica-APTES nanoparticles in isopropanol are gently dried and then redispersed in a 1-2pH acidic aqueous HCl solution. After gentle vortexing of the nanoparticle dispersion, it is combined with the polymer solution to give a final dry silica volume loading of approximately 0 vol %, 2.5 vol % (7.5 wt %), 7 vol % (15 wt %), 11 vol % (22.5 wt %), and 17 vol% (30 wt%). The solution is sonicated for 10 min to remove

bubbles. Films are cross-linked by sandwiching the hybrid solution between two quartz plates separated by spacers and exposing the film to 354 nm UV light (Spectrolinker XL-1000, Spectronics Corp.) for 240 s. The films are then dried under vacuum at 25 °C overnight to remove any residual solvent.

Cross-sectional images of the hybrid films are acquired with a Zeiss Gemini Ultra-55 Analytical Scanning Electron Microscope using a beam energy of 5 keV. Prior to imaging, the films are immersed in liquid N_2 and cryo-fractured are cryofractured to provide a clean surface. Density measurements of the hybrid films are conducted with a density determination kit (Mettler Toledo) following Archimedes' principle. Heptane is used as the secondary liquid. Glass transition temperature of the membranes are found using a Q200 differential scanning calorimeter (TA Instruments) scanning from −90 to 0 °C at a heating rate of 20 °C/min.

Pure gas permeability of XLPEG/silica-APTES membranes for nitrogen, methane, and carbon dioxide are measured using a custom built constant volume/variable pressure apparatus. The films are masked with brass discs to accurately define an area where gas transport could occur. Thicknesses of films are measured and are approximately 100-130 μm. Prior to testing, the films are degassed within the apparatus overnight. A fixed pressure is applied to the upstream side of the membrane, while the gas flux is recorded as a steady-state pressure rise downstream of the membrane. Permeability values are calculated as follows:

$$P = \frac{V_D l}{p_2 ART}\left(\frac{dp_1}{dt}\right) \qquad (3.1)$$

where V_D is the downstream volume (cm^3), l is the film thickness (cm), p_2 is the upstream pressure (cmHg), A is the surface area of the film (cm^2), R is the gas constant, T is the absolute temperature (K), and dp_1/dt steady state pressure rise downstream at fixed upstream pressure (cmHg/sec). The measurements are obtained under isothermal conditions at 308 K. Diffusion and solubility coefficients are calculated following the solution diffusion model and permeation time-lag experiments.

Dynamic mechanical analysis of the hybrid membranes is conducted using a TRITEC 2000 DMA (Triton Technology Ltd) in tension geometry. Films are clamped at room temperature, and tension is applied below the glass transition temperature. Modulus and tan δ values are collected at a scan rate of 2 °C/min at a frequency of 1 Hz under inert N_2 atmosphere.

3.3 Results and Discussion

A schematic of the silanization of silica nanoparticles with aminopropyl triethoxysilane (APTES) is shown in **Figure 3.1(a)**. APTES is added in excess such that the molar amount of APTES is 7 times more than the calculated monolayer coverage on the silica surface to drive the reaction to completion.[115,116] The resulting amine-modified silica nanoparticles will be referred to as silica-APTES. I confirm the presence and stability of APTES after repeated purification of the nanoparticle dispersion as shown in **Figure 1(b) and (c)**. I use the addition of ninhydrin to detect the presence of primary amines. The reaction of ninhydrin with primary amines results a deep purple hue, known as Ruhemann's purple.[117] After the addition of ninhydrin to a solution of silica-APTES, I observe a dramatic color change from clear to purple within seconds after addition, indicating the successful coverage of the surface. CO_2 adsorption cycles of silica-APTES are conducted using Thermogravimetric analysis at 40 °C with argon as an inert gas and is shown in Figure 1(c). Total CO_2 adsorption capacity can be a quantitative indicator of the total surface coverage of amines on silica nanoparticles. Silica-ATPES adsorbs 300% more CO_2 than native hydroxyl terminated silica (silica-OH), increasing capacity from 0.22 mmol/g to 0.66 mmol/g. This corresponds to an approximate surface concentration of 2.7 amine/nm^2 when taken into account the bare silica BET surface area of 293 m^2/g. APTES coverage on silica is reported to be roughly between 2.1 and 4.2 amine groups per nm^2, depending on the initial concentration of hydroxyl groups[115], and suggests that I have approximately achieved monolayer coverage.

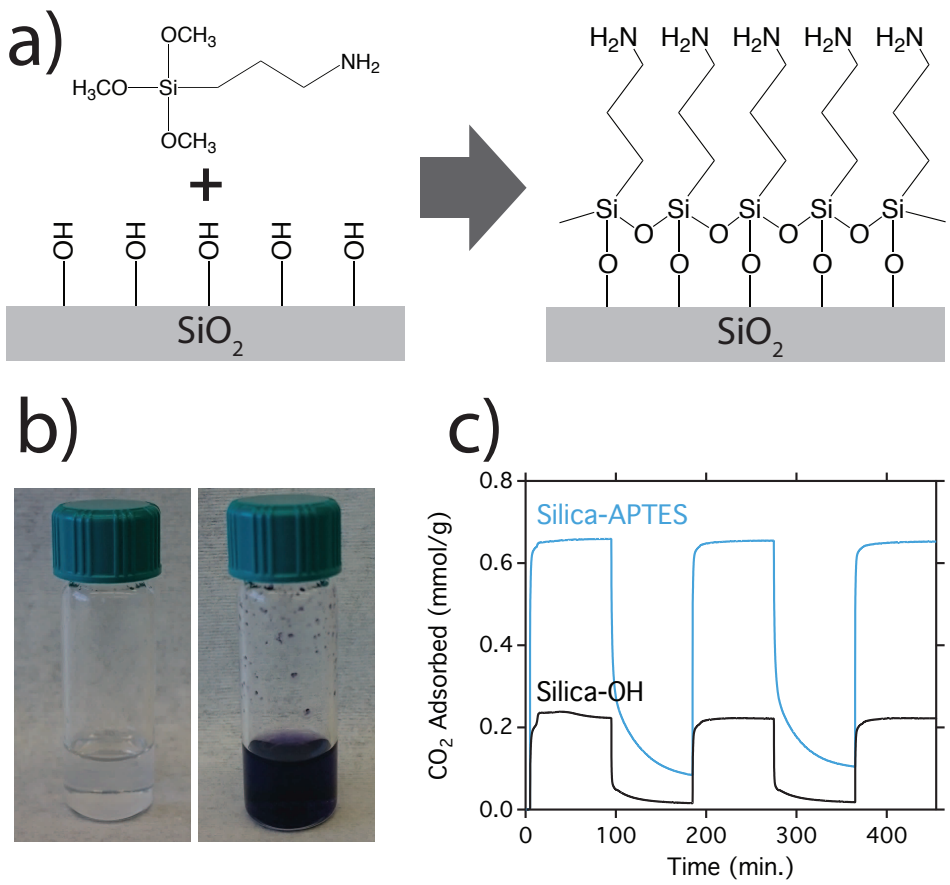

Figure 3.1. (a) Schematic of silanization with APTES. (b) Observing color change from clear to purple of silica-APTES when ninhydrin is added. (c) CO_2 adsorption cycles on TGA at 40 °C. Silica-APTES has 3 times more adsorption capacity than native silica-OH.

Morphological characterization of the homogeneity of the hybrid membranes is performed using cross-sectional SEM and is shown in **Figure 3.2**. Membranes are prepared with 2.7, 6.6, 10, or 16 volume % silica-APTES. Prior to imaging, the membranes are immersed in liquid N_2 and cryo-fractured to provide a clean surface. The observed combination of good miscibility between the polymer and the silica-APTES, the absence of obvious defects, and the homogeneity of the distribution of nanoparticles are good indicators that APTES interacts sufficiently well with the ether groups in XLPEG. I further confirm this through density measurements of the hybrid membranes (**Figure 3.3**). The hybrid membranes exhibit a clear linear relationship between density and volumetric loading consistent with good interfacial interactions.[109] The density measurements also indicate that there are no changes in the polymer free volume, which is also known to contribute to changes in permeability. Interestingly, I note that the membranes with the highest loadings (Figure 3.2(c, d)) exhibit the most uniform dispersion of nanoparticles.

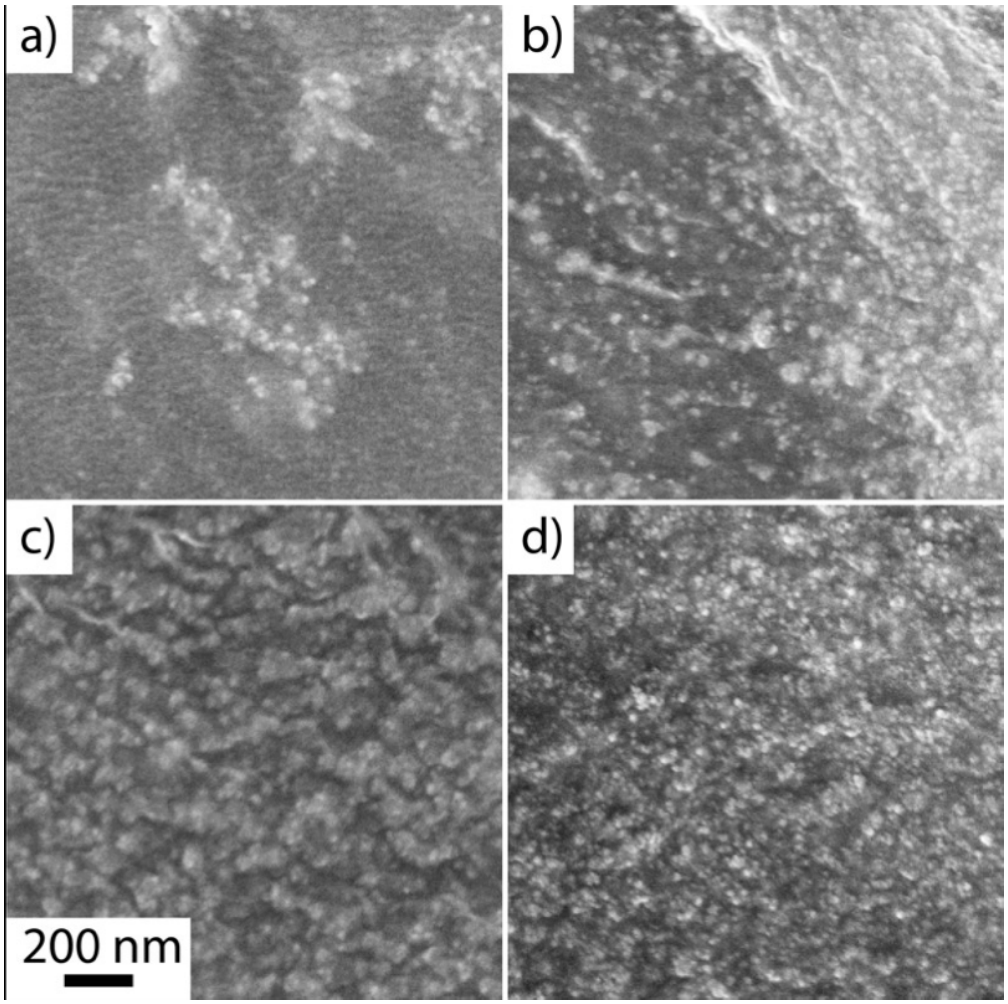

Figure 3.2. SEM cross-section images of hybrid membranes containing (a) 2.7 vol%, (b) 6.6 vol%, (c) 10 vol%, and (d) 16 vol% silica-APTES.

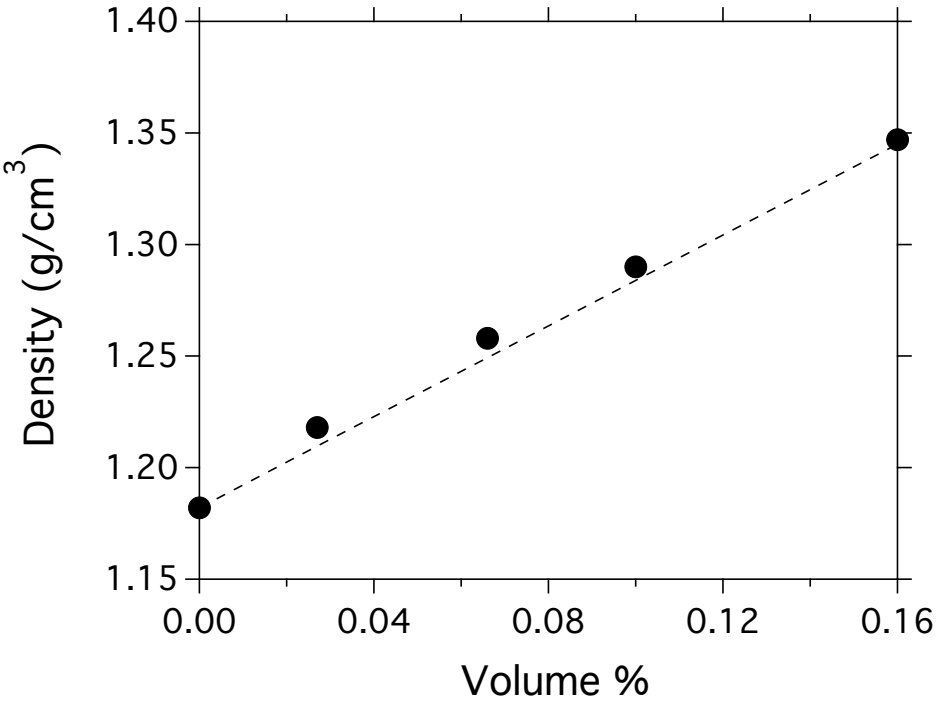

Figure 3.3. Density of hybrid XLPEG/silica-APTES membranes. Experimental densities (circles) are well correlated with calculated volume additive density (dotted line), suggesting good interaction between the polymer and nanoparticles.

Gas transport properties of the hybrid membranes are shown in **Figures 3.4 and 3.5**. I compare the measured permeability values to values predicted by Maxwell's equation. As an effective medium model, Maxwell's equation attempts to predict the permeability of heterogeneous two-phase membranes as a function of only the volume loading of the dispersed phase and does not take interfacial effects into consideration.[77] Thus, for an impermeable dispersed phase, I anticipate permeability to decrease as loading is increased due to an increase in diffusive tortuosity. Maxwell's equation for an impermeable dispersed phase is written as follows,

$$P_{Maxwell} = P_p \frac{2-2\phi_{SiO2}}{2+\phi_{SiO2}} \qquad (3.2)$$

where $P_{Maxwell}$ and P_p are the permeabilities of the hybrid and polymer, respectively, and ϕ_{SiO2} is the volume fraction of silica. I plot CO_2 permeability with respect to the relative deviation from Maxwell's equation as shown in Figure 3.4(a).

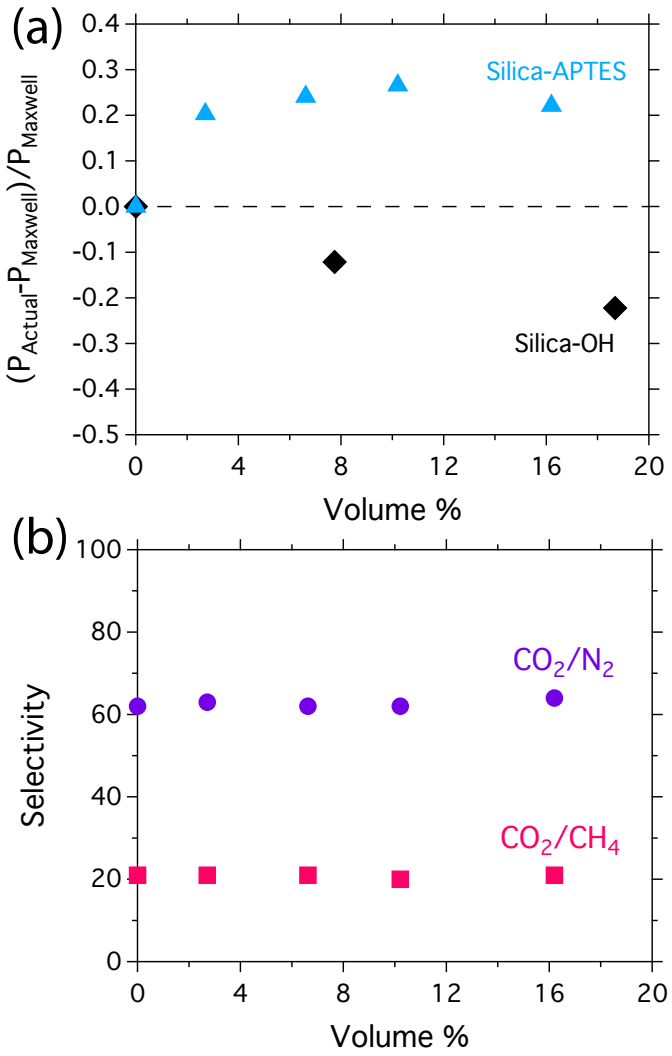

Figure 3.4. (a) Relative CO_2 permeability deviation from Maxwell's equation of silica-APTES (triangles) hybrid membranes as a function of volume %. Silica-OH hybrid membranes (diamonds) are included for comparison. Dashed line represents predictions from Maxwell's equation. CO_2 permeability in hybrids is higher than expected by Maxwell's equation. (b) CO_2/N_2 (circles) and CO_2/CH_4 (squares) selectivity as a function of volume %. Measurements were performed at 35 °C and 6 atm.

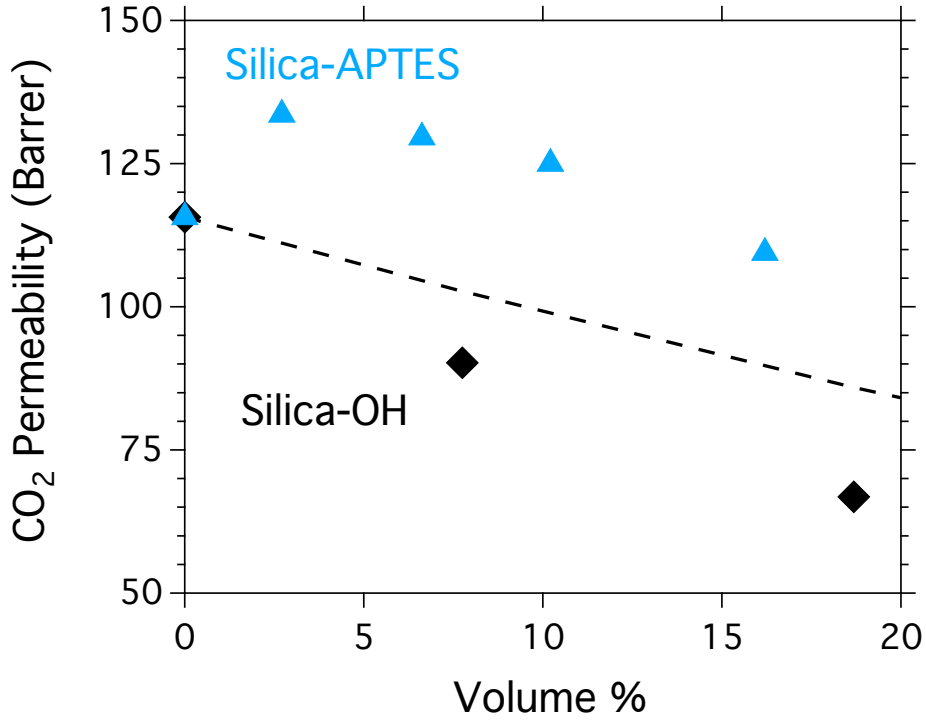

Figure 3.5. Pure gas CO_2 permeabilities of hybrid membranes with silica-APTES and native silica-OH nanoparticles. Permeability of silica-APTES hybrids is higher than neat XLPEG and those predicted by Maxwell's model (dotted line)

Surprisingly, the hybrid membranes with silica-APTES show a positive deviation from the trend predicted by Maxwell's equation. I expect that the improvement in transport properties is a result of the added functionality and interaction with the polymer arising from silica surface APTES groups. The permeability of all membranes is at least 20% higher than what would be expected from the model and continues to increase from 0 to 10 vol% before plateauing. Additionally, the absolute CO_2 permeability of hybrid membranes is higher than neat XLPEG, except at the highest loading, achieving a maximum permeability of 133 barrers (Figure 3.5). For comparison, I include the permeability values when silica-OH is the inorganic component instead in Figure 3.4(a). These hybrids exhibit a detrimental deviation from Maxwell's equation due to stronger hydrogen-bonding interactions than silica-APTES with XLPEG, which further induce rigidification of the polymer.[109] Selectivities of CO_2/N_2 and CO_2/CH_4 are shown in Figure 3.4(b). In both cases, selectivity is constant and is not affected by addition of silica nanoparticles. CO_2/N_2 and CO_2/CH_4 selectivities are 62 and 22, respectively. I speculate that improvement in permeability in hybrid membranes over the neat polymer is a result of changes in polymer dynamics. The glass transition temperature (T_g) decreases from -38 °C in neat XLPEG to -41 °C for all hybrid membranes as shown in **Figure 3.6**. The modest decrease in T_g indicates a slight increase in the segmental mobility and relaxation of polymer chains, which would allow for increased molecular diffusion through the polymer over the bulk. This in contrast to hybrids containing silica-OH which show rigidification of the polymer at the interface. Amine

groups as postulated earlier exhibit weaker hydrogen bonding interactions than hydroxyl groups with the XLPEG. Fortunately, the interaction is still sufficient to promote good homogeneity and dispersablity of the silica while affording more flexibility for segmental chain motion.

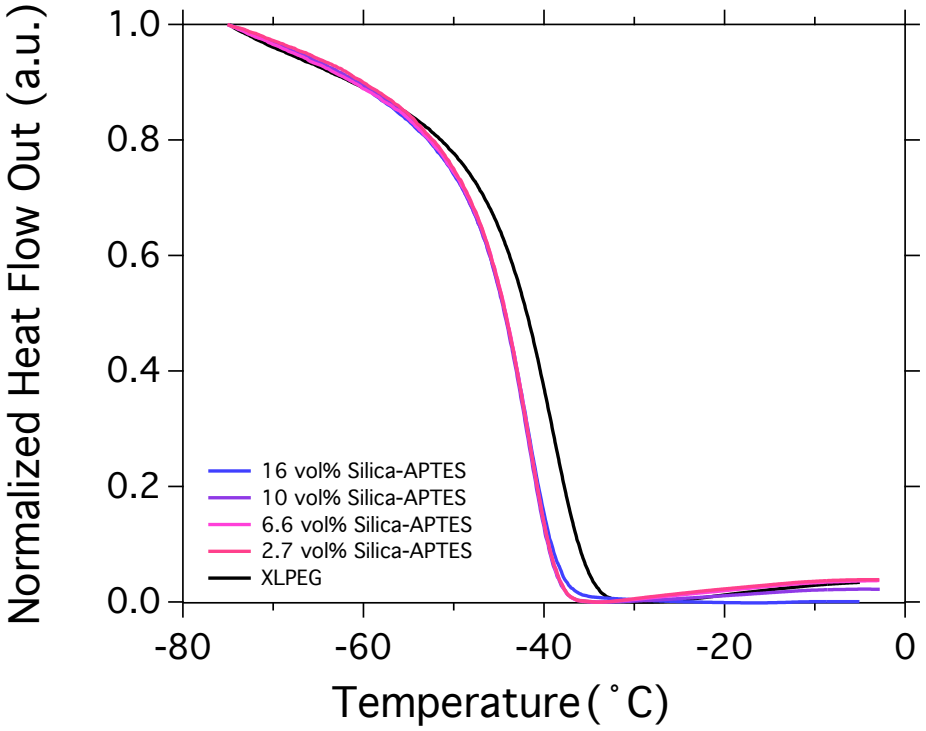

Figure 3.6. DSC thermograms of hybrid membranes. The glass transition shifts lower from -38 °C to -41 °C.

Transport through membranes can often be described by the solution-diffusion model. The permeability (P) of a membrane is the product of a kinetic diffusion coefficient (D) and a thermodynamic solubility coefficient (S).[23] I analyze permeation time lag experiments and use the solution-diffusion model[96] to calculate diffusion and solubility coefficients for methane and carbon dioxide to confirm that the expected increase in diffusion is a result of polymer relaxation. The results are presented in **Figure 3.7**. Diffusion coefficients of CO_2 and CH_4 show an immediate increase upon addition of silica-APTES nanoparticles, which results in an increase in permeability, thereby confirming that segmental mobility has increased, as suggested by T_g shifting from -38 °C to -41 °C. CO_2 diffusion increases from $5.4*10^{-7}$ cm^2/s to $6.2*10^{-7}$ cm^2/s and CH_4 diffusion increases from $4.1*10^{-7}$ cm^2/s to $5.2*10^{-7}$ cm^2/s when 2.7 vol% of silica-APTES is added. CO_2 has a larger diffusion coefficient than CH_4 due to the smaller kinetic diameter of CO_2 (3.3 Å vs. 3.8 Å). As silica loading increases, molecular diffusion decreases from its maximum value due to the increase in tortuosity from a higher density of nanoparticles, which competes with the effect from polymer relaxation. For CO_2, the diffusion continues to drop as nanoparticle loading increases. I suspect this is due to the enhanced adsorption of CO_2, due to the amine groups on the silica

surface, which may act as traps for CO_2, but not CH_4 and thereby impede the movement of CO_2. This is confirmed by inspecting the solubility of CH_4 and CO_2. Solubility of CO_2 increases from 1.5 $cm^3(STP)cm^{-3}atm^{-1}$ in neat XLPEG up to 2 $cm^3(STP)cm^{-3}atm^{-1}$ as silica-APTES loading increases. Unsurprisingly, CH_4 solubility remains approximately 0.09 $cm^3(STP)cm^{-3}atm^{-1}$ at all loadings. I find the solubility selectivity increases from 15.5 in pure XLPEG up to 21.8 in hybrid membranes containing 16 vol% silica-APTES due to the amine/CO_2 interaction. Thus, I demonstrate that polymer segmental dynamics, tortuosity, and gas adsorption can all contribute to effects on molecular diffusion.

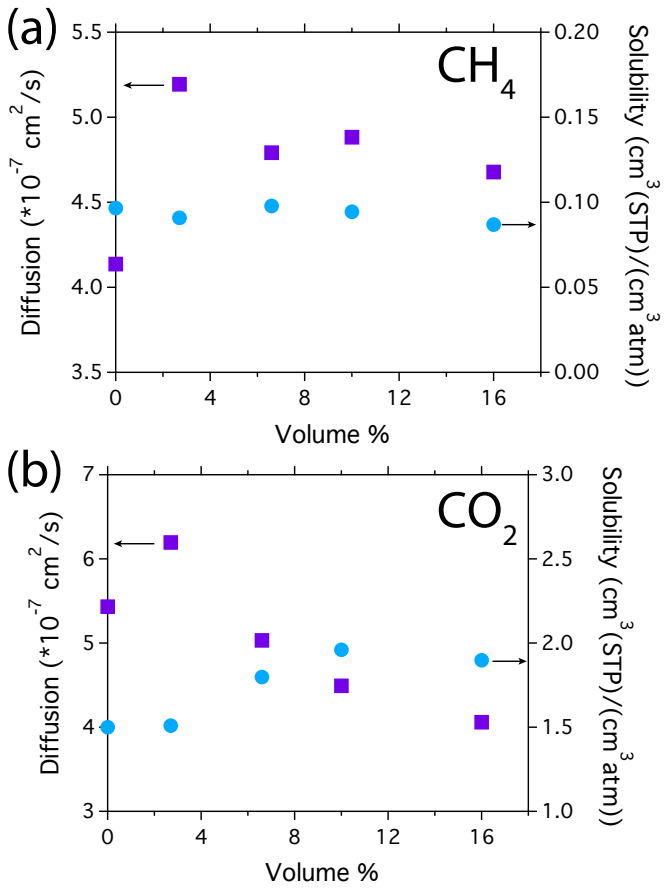

Figure 3.7. Diffusion (squares) and solubility (circles) coefficients of XLPEG/silica-APTES hybrid membranes for (a) CH_4 and (b) CO_2. The initial increase in diffusion for both gases is reflective of relaxation of segmental polymer dynamics. The increase in solubility for CO_2 is attributed to amine groups on silica nanoparticles.

Mechanical properties of hybrid membranes are determined through dynamical mechanical analysis (DMA) and are shown in **Figure 3.8**. Samples are prepared for tension geometry. The sample is fully tightened below its glass transition temperature to make for a more accurate measurement. The glassy modulus increases from 3.5 gigapascal (GPa) in the neat XLPEG up to 8.5 GPa in hybrid membrane containing 16 vol% silica-APTES, a 250% increase. The rubbery modulus remains stable between 17 and 22 MPa. Thus, I have demonstrated that our hybrid membranes exhibit a dual enhancement of gas transport and

mechanical properties as compared to the neat XLPEG. I note that the observed dip in rubbery modulus of neat XLPEG between 10 and 40 °C is likely due to trivial amounts of moisture condensation, even though careful consideration is taken to ensure a dry environment. The dip is consistent in multiple XLPEG samples, never observed in hybrid samples, and is not reflective of decrease in mechanical properties of the polymer. Additional T_g information for the membranes is also found from the peak position of tan δ (**Figure 3.9**). The T_g trend from DMA measurements closely corresponds to that determined through DSC, even though the absolute T_g values differs between the two techniques. The T_g of neat XLPEG from DMA is -29 °C, and the T_g decreases to between -32 and -34 °C when silica-APTES was added. The different T_g values determined by DSC and DMA are not unexpected because T_g is known to vary between different measurement techniques. In addition, thermal decomposition curves of the hybrid membranes show increased thermal stability as loading of silica-APTES increases (**Figure 3.10**). At 16 vol%, the decomposition temperature is 100 °C higher than the neat XLPEG.

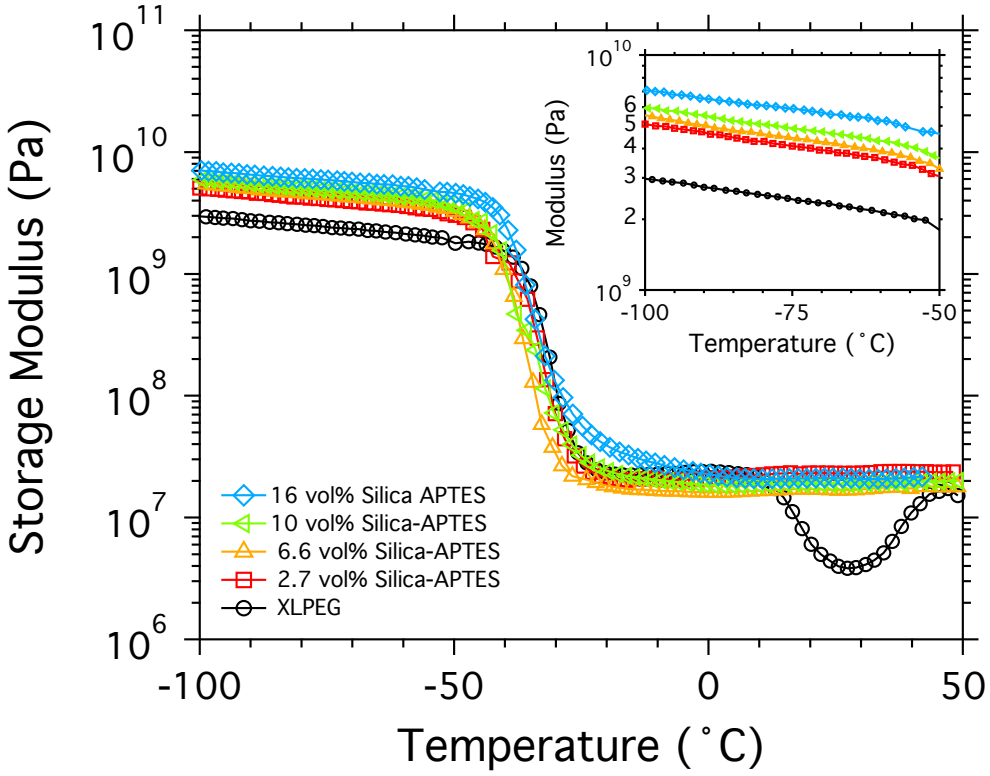

Figure 3.8. Dynamic storage modulus of silica-APTES hybrid membranes. Inset show magnified region below the glass transition temperature. Mechanical properties are robust over all volume loadings. DMA measurements were performed at 1 Hz and scan rate of 2 °C/min.

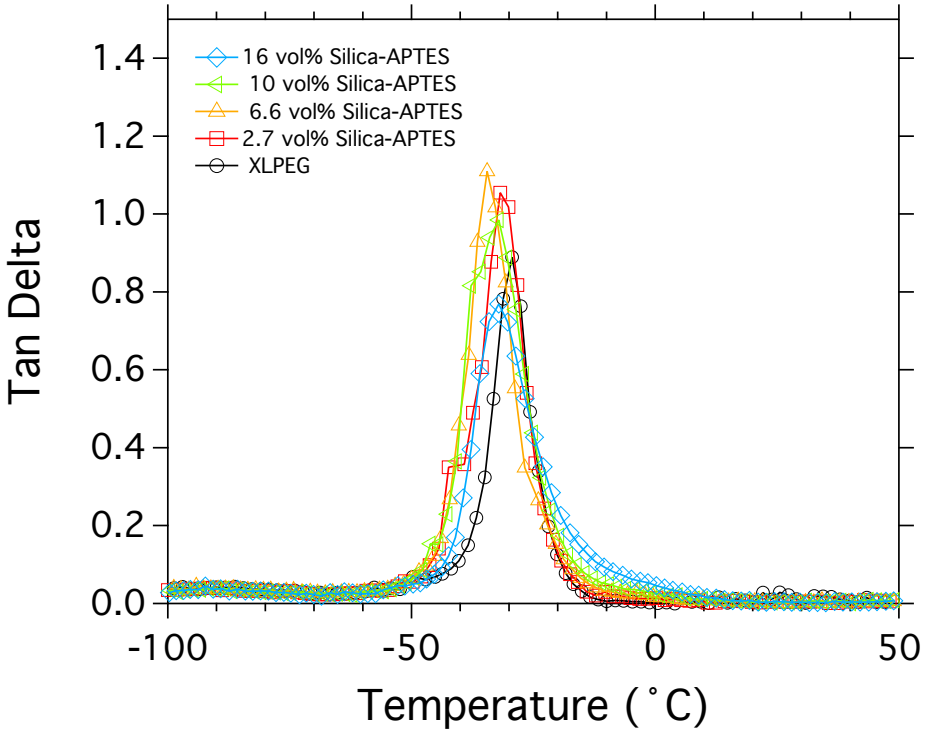

Figure 3.9. Tan delta of hybrid membranes as measured by DMA. T_g according to tan delta decreases with addition of silica-APTES.

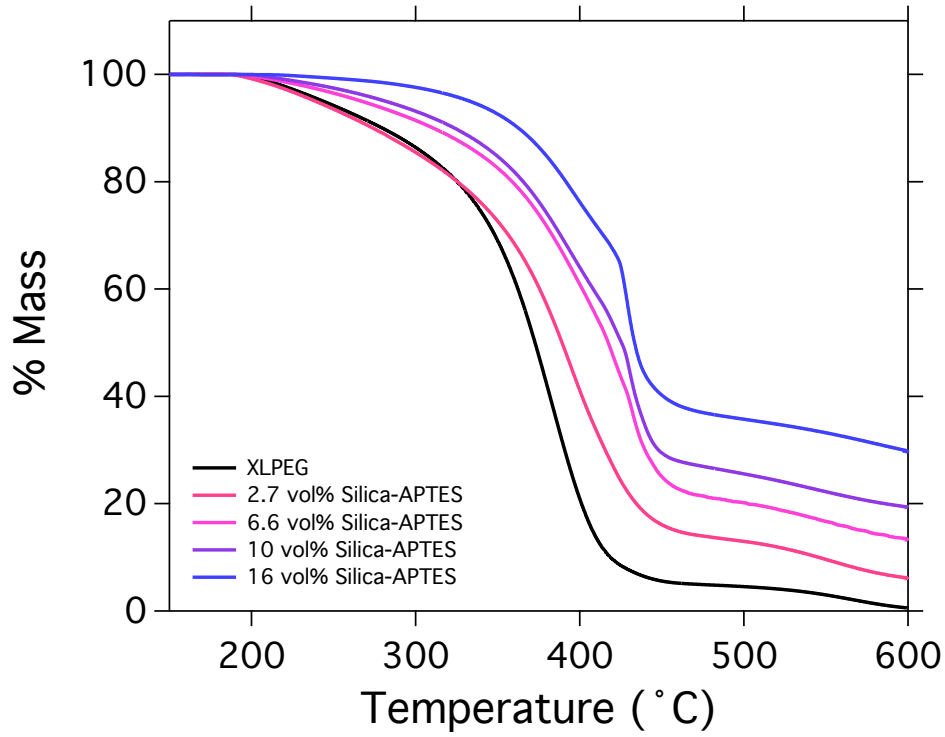

Figure 3.10. TGA decomposition of hybrid membranes. Decomposition temperature increases as silica-APTES loading is increased, indicating higher thermal stability.

3.4 Conclusions

In summary, I demonstrate simultaneous improvement of permeability and mechanical properties of hybrid membranes without sacrificing selectivity through appropriate control of the nanoparticle interface. Silanization of silica nanoparticles with APTES results in a 20% improvement in permeability from Maxwell's equation and 250% improvement in mechanical properties. Permeability in hybrid membranes of all gases deviates favorably away from Maxwell's equation and towards values higher than permeability in the neat XLPEG. The improvement in permeability is due to the relaxation of the polymer at the interface, which resulted in an immediate increase in the diffusion coefficients of both CO_2 and CH_4. This work provides an avenue to achieve a superior hybrid membrane through control of interfacial interactions between polymers and nanoparticles.

3.5 Acknowledements

I would like to thank B.A. Helms for scientific discussions. Work at the Molecular Foundry was supported by the Office of Science, Office of Basic Energy Sciences, of the U.S. Department of Energy under Contract No. DE-AC02-05CH11231. N.C. Su was supported by

the Department of Defense (DoD) through the National Science & Engineering Graduate Fellowship Program.

3.6 Supporting Information

Supporting information for this chapter can be found in Appendix A.2.

Chapter 4. Enhanced Permeation Arising from Dual Transport Pathways in Hybrid Polymer-MOF Membranes

Adapted from "Enhanced permeation arising from dual transport pathways in hybrid polymer-MOF membranes." N.C. Su, D.T. Sun, D.K, Britt, C.M. Beavers, W.L. Queen, and J.J. Urban. *Energy & Environmental Science.* 2016, DOI: 10.1039/C5EE02660A. Reproduced with permission from *Energy & Environmental Science.*

The rise of anthropogenic global warming has sparked new interest in developing strategies to mitigate carbon dioxide emissions. Conventional carbon capture processes are not economically viable at scale due to their enormous energy cost. Membrane-based separation is a promising alternative, but its separation performance has traditionally been limited by a well-known trade-off between permeability and selectivity. Incorporating the insights gained from molecular transport effects from inorganic size and surface functionalization, I explore a hybrid polymer/inorganic membrane with dual transport pathways. This special class of membranes allows us to overcome this traditional limitation. The inorganic phase consists of a metal-organic framework (MOF), which is an ideal inorganic dispersant to construct dual transport pathways as the crystalline porous structure of MOFs is more amenable to molecular diffusion than polymers. Previous hybrid membrane research has failed to achieve sufficiently high loadings to establish a percolative network necessary for dual transport, often due to mechanical failure of the membrane at high loading. Using polysulfone and UiO-66-NH_2 MOF as a model system, I achieve high MOF loadings (50 wt%) and observe the evolution from single mode to dual transport regimes. The newly formed percolative pathway through the MOF, which has not previously been observed, acts as a molecular highway for gases. As the MOF loading increases to 30 wt%, CO_2 permeability increases linearly from 5.6 barrers in polysulfone homopolymer to 18 barrers. Crucially, between 30 and 40 wt%, a percolative MOF network arises and the CO_2 permeability dramatically rises from 18 to 46 barrers; an eight-fold increase over pure polysulfone, while maintaining selectivity over methane and nitrogen near the pure polymer at 24 and 26, respectively. A similar phenomenon is observed in the measurement of the diffusion coefficient and is consistent with the formation of dual transport pathways. The findings in this study enable new approaches towards designing hybrid membranes with dual transport pathways. This is an important step towards a competitive membrane-based carbon capture process.

4.1 Introduction

While historical trends indicate the gradual decarbonization of fuel sources over time, the global economy in its present state remains heavily dependent on fuels with high carbon content such as coal, oil, and natural gas. Consequently, carbon emissions are reaching record levels and are identified as contributing to recent patterns of global climate change.[8] Mitigating carbon emissions to reverse or curb climate change using traditional amine scrubbing techniques is not scalable due to the large energy consumption and physical footprint required. Membrane separation processes have emerged as a promising technology because of the passive nature of its operation and relative ease of scalability.[22] Unfortunately, many commercialized membranes have not been optimized for the stringent purification metrics required for carbon capture applications.[118] These membranes, typically derived from polymers, suffer from an inherent trade-off between permeability and selectivity as popularized by Robeson and his eponymous plot.[28] The central dilemma is that many polymers provide either high permeability or high selectivity but not both, which limits the industrial utility of these systems.

Hybrid membranes, which typically contain an organic polymer phase and a dispersed inorganic phase, have been shown to significantly improve separation performance over pure polymer systems in a variety of applications including carbon capture[75,119–123], hydrogen purification[124], and petrochemicals.[51,60,125] The inorganic phase can be a nonporous materials such as nanoparticles[51,55,109] or porous materials such as carbon molecular sieves[39,50], zeolites[126,127], and metal-organic frameworks[75,120–122,124,125,128–130]. When integrated with an organic polymer into a hybrid system, the competitive advantages of each individual phase can be realized, such as the processability of polymers and molecular selectivity of inorganics, while also fostering new properties and functionalities through synergistic enhancements.[41] While conventional mixed matrix systems display improved separation properties, the inorganic phase often is not present in sufficient quantity to establish a percolative network, and thus their transport behavior is limited by classical solution-diffusion principles. If hybrid membranes can be designed to possess continuity of both organic and inorganic phases, there is an opportunity to reach new non-classical transport regimes governed by dual transport pathways.[119,131,132] In this dual transport regime, the inorganic phase will act as a molecular transport highway. However, achieving dual transport pathways is no easy feat as high loadings of the inorganic phase are required to achieve percolation.[133] Only a few studies have reported inorganic loadings in hybrid membranes surpassing 40 wt% due to mechanical failure of the membrane.[89,119,125] This is primarily a result of poor interphase interactions, which lead to the formation of voids, commonly referred to as “sieves-in-a-cage,” in hybrids containing porous inorganic materials.[42,47,134] Under these circumstances, molecular diffusion can circumvent the inorganic sieve and instead transport through the less selective voids at the interface. Thus, precise control of both the polymer and inorganic phase is critical to maximize separation performance.

Metal-organic frameworks (MOFs) are a relatively new class of 3-D porous crystalline inorganic materials that are ideal candidates to incorporate in hybrid membranes and

design dual transport pathways.[25,135] Their chemical flexibility provides opportunities to tune and optimize interfacial interactions between the MOF crystal and a polymer, thus reducing chances for mechanical failure. Further, large internal surface areas, tunable but rigid pores[135], and chemical functionalities of MOFs (accessible through functionalization of the organic linkers[17] or Lewis acid open metal sites[136]) can simultaneous improve diffusive size selectivity and adsorption uptake of gases in membranes. While inclusion of the MOF as a dispersed phase can be expected to improve gas transport properties, the full benefit of hybrid MOF membranes is only realized when a continuous phase exists, which would lead to a percolative transport highway.

Here, I report on the design and characterization of robust hybrid membranes possessing dual transport pathways using UiO-66-NH_2 MOF and polysulfone for relevant carbon capture applications. UiO-66-NH_2 is a zirconium based MOF, comprised of $Zr_6O_4(OH)_4$ octahedral clusters and 2-amino-1,4 benzenedicarboxylate linkers. UiO-66-NH_2 is a well-studied MOF and exhibits high thermal stability, water stability, and carbon dioxide adsorption.[17,137] I selected the amine derivative over its non-functionalized counterpart (UiO-66) to maximize interactions with polar backbone groups in the polysulfone polymer, which is critical to avoid mechanical failure as I increase the MOF loading beyond what is normally considered high loadings (i.e. 30 wt%). This hybrid system successfully maintains structural integrity at very high loadings. I demonstrate, to the best of our knowledge, the first hybrid system possessing dual transport pathways.

4.2 Experimental Procedure

UiO-66-NH_2 Synthesis. UiO-66-NH_2 is prepared following a modified version of a microwave synthetic technique.[19] Zirconium tetrachloride (99.5%) is supplied by Alfa Aesar, 2-amino-1,4-benzenedicarboxylic acid (99%) and dimethylformamide (99%) is supplied by Sigma-Aldrich.

35 mmol of $ZrCl_4$ (8.12 g) and 0.11 mmol of nanopure water (2 ml) are added to 148 mmol (400 mL) of DMF. The solid is allowed to fully dissolve. Separately, 35 mmol (6.28 g) of 2-aminoterephthalic acid is dissolved in 148 mmol DMF. The solutions are combined and heated using microwave irradiation (Anton Paar) in sealed vessels at 1500 W for two hours at 120°C. The resulting pale yellow powder is filtered and washed with methanol in a Soxhlet extractor overnight. The final product is dried in air overnight and finally in an oven at 65°C to remove residual solvent.

Fabrication of membranes. Udel P-1700 polysulfone is generously supplied by Solvay Plastics. Polysulfone (PSF) is dried overnight in a vacuum oven at 110 °C prior to use. PSF is dissolved in chloroform (BDH Chemicals) to form a 5 wt% solution and subsequently filtered with a 0.45 μm PVDF filter. For hybrid membranes containing up to 50 wt% UiO-66-NH_2, the MOF is first dispersed in chloroform by sonication. Once dispersed, the MOF is "primed" by adding a portion of the PSF solution equal to 35 wt% of the total MOF mass and subsequently sonicated. Priming the MOF is believed to increase interaction and homogeneity between the MOF and polymer by coating the MOF with a thin polymer layer[39]. The remaining PSF is then added to the MOF mixture and sonicated. To mitigate

MOF settling during casting, the solution is concentrated by gentle purging with nitrogen gas to evaporate the solvent until the solids concentration reaches 25-30 wt%. The solution is then cast into a casting plate, loosely covered, and allowed to dry under atmospheric conditions over the course of two days. The dried membranes are then placed into a vacuum oven at 110 °C overnight to remove any residual solvent and water. The target thickness of each film is 65 μm. The thickness of each film is measured individually using a micrometer.

MOF and Membrane Characterization. Nitrogen adsorption measurements of the MOF are performed at 77 K using a Tristar II Surface Area Analyzer (Micromeritics). Surface area values are calculated following Brunauer-Emmett-Teller method over a relative pressure range, p/p_o, of 0.05 to 0.25. Carbon dioxide adsorption isotherms of the MOF and membranes are collected using an ASAP 2020 Physisorption Analyzer (Micromeritics) at 20 °C up to a pressure of 1 bar. Before adsorption measurements are carried out, all samples are heated under vacuum at 110 °C for 12 hours to remove residual solvent in the pores.

X-ray diffraction patterns of the MOF powder and hybrid membranes are collected at ALS Beamline 12.2.2 on a Perkin Elmer amorphous silicon detector using synchrotron radiation monochromated by silicon(111) to a wavelength of 0.4978(1) Å. Distance and wavelength calibrations were done, using a NIST LaB_6 diffraction standard, with the program Dioptas, which was also employed for radial integration. Simulated powder diffraction patterns of UiO-66-NH_2 are calculated using Mercury 3.6 software (Cambridge Crystallographic Data Centre). Glass transition temperatures of the membranes are determined using a Q200 Differential Scanning Calorimeter (TA Instruments). The samples are heated under vacuum at 110 °C for two hours to remove water vapor before scanning to 250 °C at a scan rate of 20 °C/min. Density measurements of the bulk hybrid films are performed using hydrostatic weighing with a density determination kit (Mettler Toledo). Heptane is used as the secondary liquid. Cross-sectional images of the hybrid films are acquired with a Zeiss Gemini Ultra-55 Analytical Scanning Electron Microscope using an accelerating voltage of 5 keV. Prior to imaging, the films are cryofractured after immersion in liquid N_2 to provide a clean surface.

Gas Transport Measurements. Pure gas permeability of PSF/UiO-66-NH_2 membranes for nitrogen, methane, and carbon dioxide are measured using a custom built constant volume/variable pressure apparatus.[96,109] The films are masked with brass discs to accurately define an area through which gas transport could occur. Prior to testing, the films are degassed within the apparatus. A fixed pressure is applied to the upstream side of the membrane, while the gas flux is recorded as a steady-state pressure rise downstream of the membrane. Permeability values are calculated as follows:

$$P = \frac{V_D l}{p_2 ART}\left(\frac{dp_1}{dt}\right) \qquad (4.1)$$

where V_D is the downstream volume (cm^3), l is the film thickness (cm), p_2 is the upstream pressure (cmHg), A is the exposed area of the film (cm^2), R is the gas constant, T is the

absolute temperature (K), and dp_1/dt steady state pressure rise downstream at fixed upstream pressure (cmHg/sec). The measurements are obtained under isothermal conditions at 308 K.

Diffusivity and solubility of the hybrid membranes are calculated through permeation time lag experiments described in detail elsewhere[96] and analyzed employing the solution-diffusion model.

4.3 Results and Discussions

4.3.1 Characterization of UiO-66

Traditional MOF synthesis relies on conventional solvothermal techniques, which usually requires prolonged reaction times that range from hours to several days. Microwave assisted synthetic techniques are an emerging method to rapidly synthesize MOFs[138–140] and other microporous materials[141] within a matter of minutes to a few hours without compromising crystallite quality. This technique is not only advantageous for its short reaction time, but also for its scalability and particle size control. I employ microwave synthesis for UiO-66-NH_2 for the reasons listed above and to minimize the risk of batch-to-batch variation. All hybrid membranes investigated contained MOFs from a single large-scale batch. In **Figure. 4.1a**, the powder X-ray diffraction pattern of the synthesized UiO-66-NH_2 shows excellent agreement with the simulated diffraction pattern. Nitrogen adsorption isotherms were collected at 77 K, as shown in **Figure 4.1b**, and follow Type 1 isotherm indicative of microporosity. Based upon this analysis, the BET surface area is calculated to be 1348 ± 5 m^2/g, which is higher than previously reported surface area values for UiO-66-NH_2, which fall between 1000 and 1150 m^2/g.[17,120]

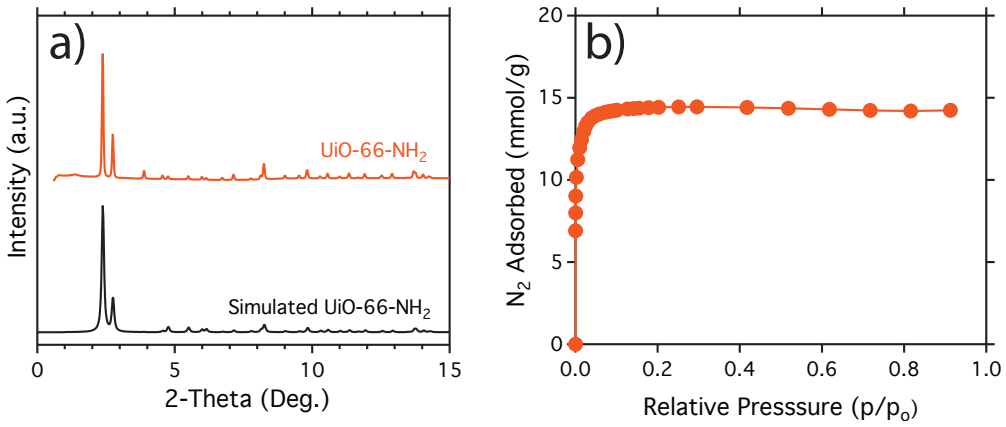

Figure 4.1. a) X-ray diffraction pattern of synthesized UiO-66-NH2 matches well with simulated pattern. b) Nitrogen adsorption isotherm of UiO-66-NH2 powder at 77 K.

4.3.2 Hybrid Membrane Characterization

By controlling the MOF-polymer interface using the techniques described previously, robust polysulfone membranes containing up to 50 wt % UiO-66-NH_2 are successfully fabricated. Few MOF-polymer membranes at such high loadings have been reported; mainly a result of mechanical failure of the membrane at these loadings, due to poor interphase interactions.[89,119,125] Thus, when undertaking the design of hybrid membranes, it is imperative to select materials which are not only individually good materials for CO_2 capture, but also with mutual chemical affinities to maximize interphase adhesion and solubility and minimize the onset of sieve-in-a-cage morphology, which deleteriously impacts the gas selectivity. One diagnostic used to understand the magnitude and type of

interfacial interactions in hybrid soft/hard systems are shifts in the glass transition temperature (T_g). Favorable interactions are noted by a T_g shift towards higher temperatures.[48,109] This positive shift is due to reduced polymer chain mobility and rigidification as the polymer becomes adsorbed onto the MOF surface, resulting in a more mechanically robust membrane. Opposite trends (i.e. reductions in T_g relative to that of the homopolymer) are observed when unfavorable interactions are present.[99,142] Glass transition temperatures as measured by differential scanning calorimetry of the hybrid membranes are presented in **Table 4.1**. The T_g of the neat homopolymer is 176 °C. The incorporation of 10 wt% UiO-66-NH_2 has a minor influence on the T_g, shifting it by only 4 °C. As MOF is further added to the membrane, I observe a larger T_g shift of 10-12 °C to a maximum T_g of 188 °C. The T_g shifts at all loadings indicates that favorable interactions are present, and I speculate this is due to hydrogen bonding interactions between the amine groups of the MOF and sulfonyl groups in the polymer. The interactions are sufficiently strong that any post-synthetic surface modification of the MOF to promote interaction is not required.

Table 4.1. Glass Transition Temperature of Hybrid Membranes

UiO-66-NH_2 weight %	T_g (°C)
0	176
10	180
20	186
30	186
40	188
50	188

Physical confirmation of good interfacial interactions as indicated by the aforementioned T_g shifts can be seen through cross-sectional imaging of the hybrid membranes. SEM cross-sections of the membranes are shown in **Figure 4.2** and **Figure 4.3** at higher and lower magnifications, respectively. The PSF homopolymer is highly uniform and dense with no sign of pinhole defects (Figure 4.2a and 4.3a). Strong interfacial interactions are observed in membranes containing 10 wt% UiO-66-NH_2 (Figure 4.2b and 4.3b) as indicated by the homogenous distribution of MOF crystals throughout the polymer. At this loading, there is minimal aggregation between MOF crystals, which have a crystallite size of approximately 400 nm in diameter. As MOF loading is increased up to 50 wt%, the membranes still display homogeneity between the polymer and MOF. Above 50 wt%, the hybrid membrane begins to lose mechanical stability. Thus, higher membrane loadings were not pursued. Furthermore, the appearance of a network of circular pattern morphology of the polymer is additional evidence of the presence of strong interfacial interactions.[119,120,125] The addition of UiO-66 induces shear stress of the polymer, which results in rigidification and elongation of polymer chains.[143] As UiO-66-NH_2 is incorporated with the polymer, the interaction

between the two phases induces a rigidification and elongation of polymer chains. This phenomenon is more evident in hybrids containing 10 and 20 wt% UiO-66-NH_2. This morphology is not to be confused with sieve-in-a-cage where delamination between the phases creates a significant volume fraction of interphase voids. As further confirmation that sieve-in-a-cage was not present in our hybrid membranes, I calculated the bulk density of each membrane as shown in **Figure 4.4**. If significant voids were present in the membranes, they would manifest itself as a non-linear density trend where the true density of the films is lower than the arithmetic average between the two phases.[89] Our hybrid membranes show a clear linear relationship between density and weight % further suggesting that good interfacial contact is present.

In addition to detecting strong interfacial interactions, the SEM cross-sections reveal another significant characteristic of these hybrid membranes advantageous for gas transport. At MOF loadings of 30 wt% or below, the MOF can be clearly discerned from the polymer as seen in Figure 4.3. At these loadings, there is sufficient polymer to completely enwrap MOF crystals. However, at 40 wt% and above, it becomes much more difficult to observe isolated MOF and polymer regions. The SEM images in Figure 4.2e and 4.2f appear to show an interconnected network of MOF crystals occasionally interrupted by the polymer. I anticipate that the transport properties in 40 and 50 wt% hybrid membranes to be different than the other membranes investigated in this study because the interconnectivity of MOF crystals will provide a parallel transport pathway to the solution-diffusion mechanism for dense polymer membranes.

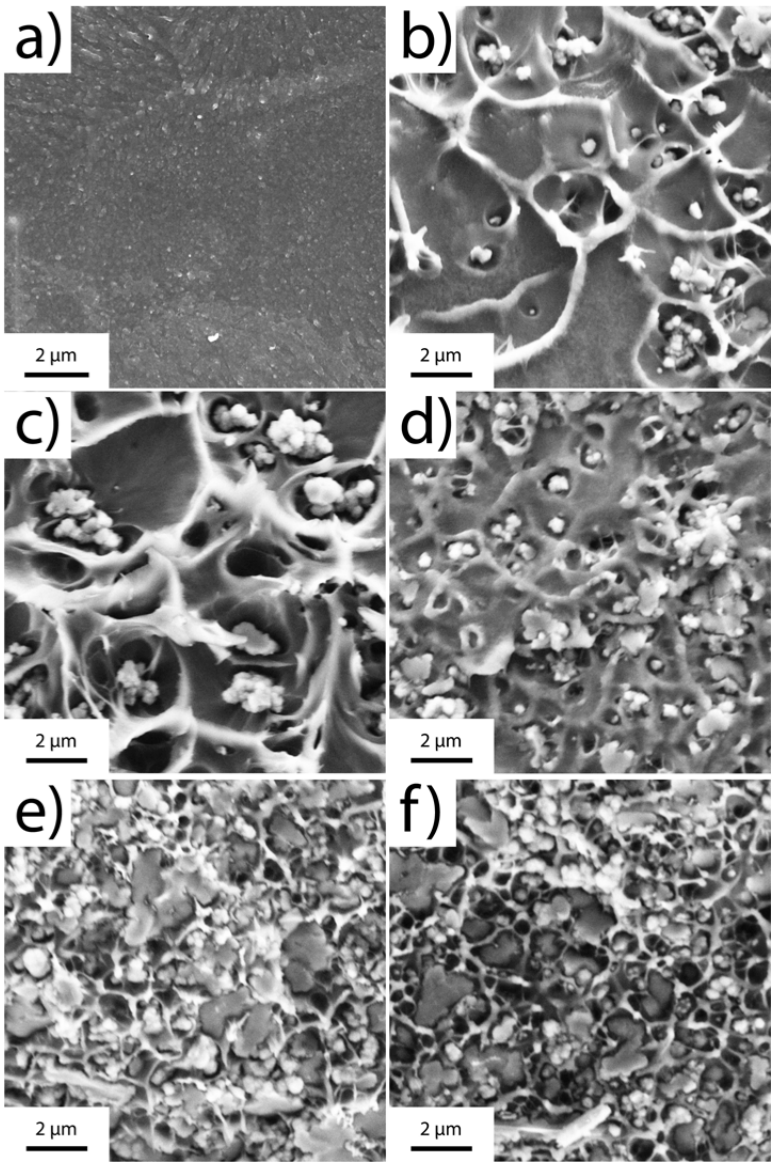

Figure 4.2. Higher magnification SEM cross-section images of (a) polysulfone homopolymer and (b -f) hybrid membranes containing (b) 10 wt%, (c) 20 wt%, (d) 30 wt%, (e) 40 wt%, and (f) 50 wt% UiO-66-NH_2, respectively. The network polymer region (brighter regions) signifies good interfacial contact between the MOF and polysulfone.

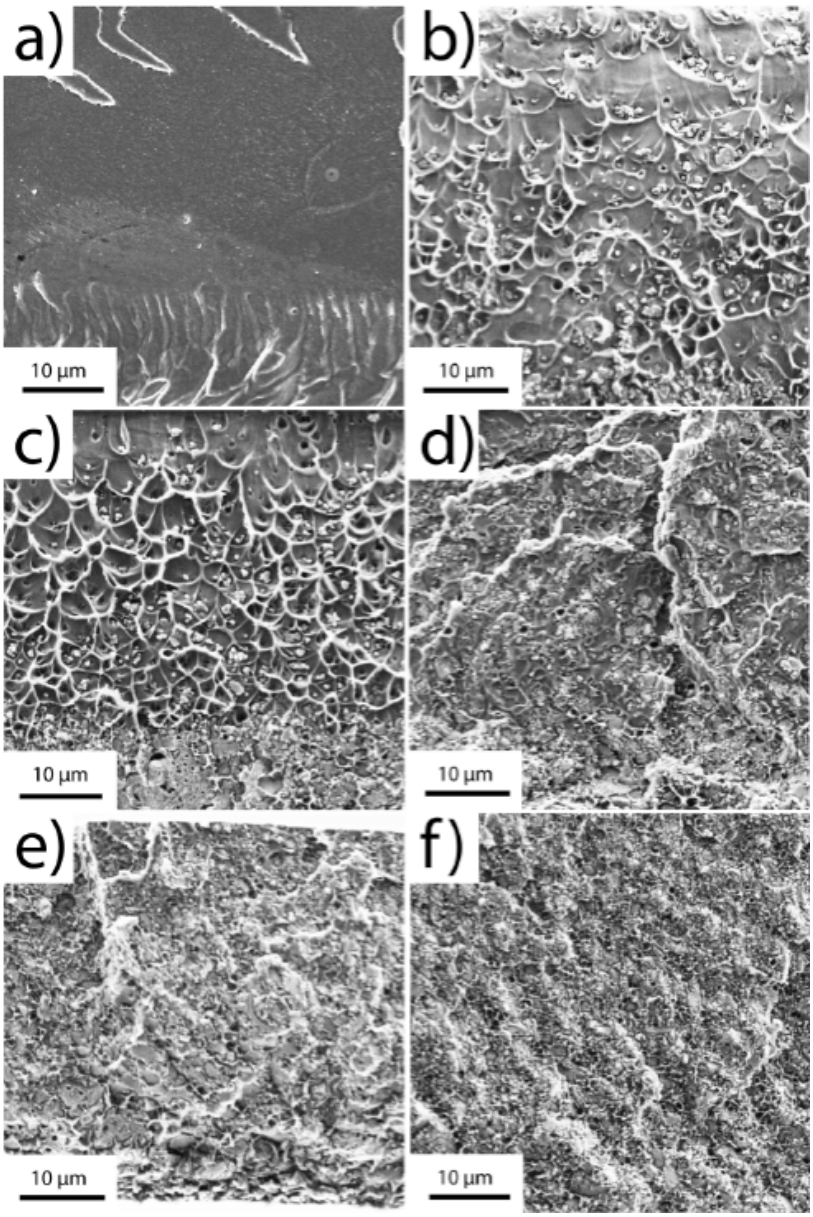

Figure 4.3. Lower magnification SEM cross-section images of (a) polysulfone homopolymer and (b -f) hybrid membranes containing (b) 10 wt%, (c) 20 wt%, (d) 30 wt%, (e) 40 wt%, and (f) 50 wt% UiO-66-NH_2, respectively. A shift in dispersion of MOF in membranes containing between 30 and 40 wt% MOF occurs, wherein interconnected MOF network can be seen in membranes containing more than 40 wt% MOF.

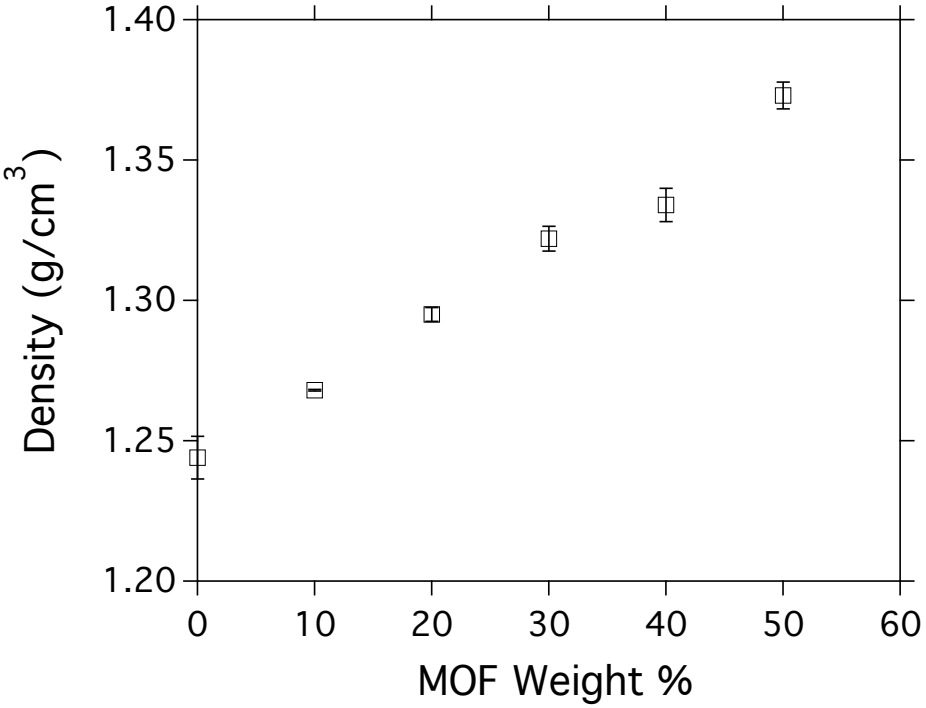

Figure 4.4. Hydrostatic density measurement of UiO-66-NH_2 PSF hybrid membranes. Density follows a linear trend, indicating good interphase interaction.

Transmittance X-ray diffraction was used to determine the presence of UiO-66-NH_2 in hybrid membranes and the diffraction patterns are shown in **Figure 4.5**. The pure polysulfone membrane shows no diffraction peaks as expected because of its amorphous nature. All hybrid membranes containing UiO-66-NH_2 display at least the two primary diffraction peaks at 2θ values of 2.38 ° and 2.68 °, confirming that UiO-66-NH_2 maintains its crystallinity during membrane fabrication. Furthermore, if the intensities are normalized by membrane thickness, I find that the intensity of the highest peak correlates well with MOF loading. The hybrid membrane containing 10 wt% UiO-66-NH_2 has a maximum peak intensity of ~25% of the maximum peak intensity of the membrane with a loading of 50 wt%. Following this trend the maximum peak intensity of 20, 30 and 40 wt% membranes are 44%, 59%, and 74% of the maximum peak intensity for 50 wt% membranes, respectively.

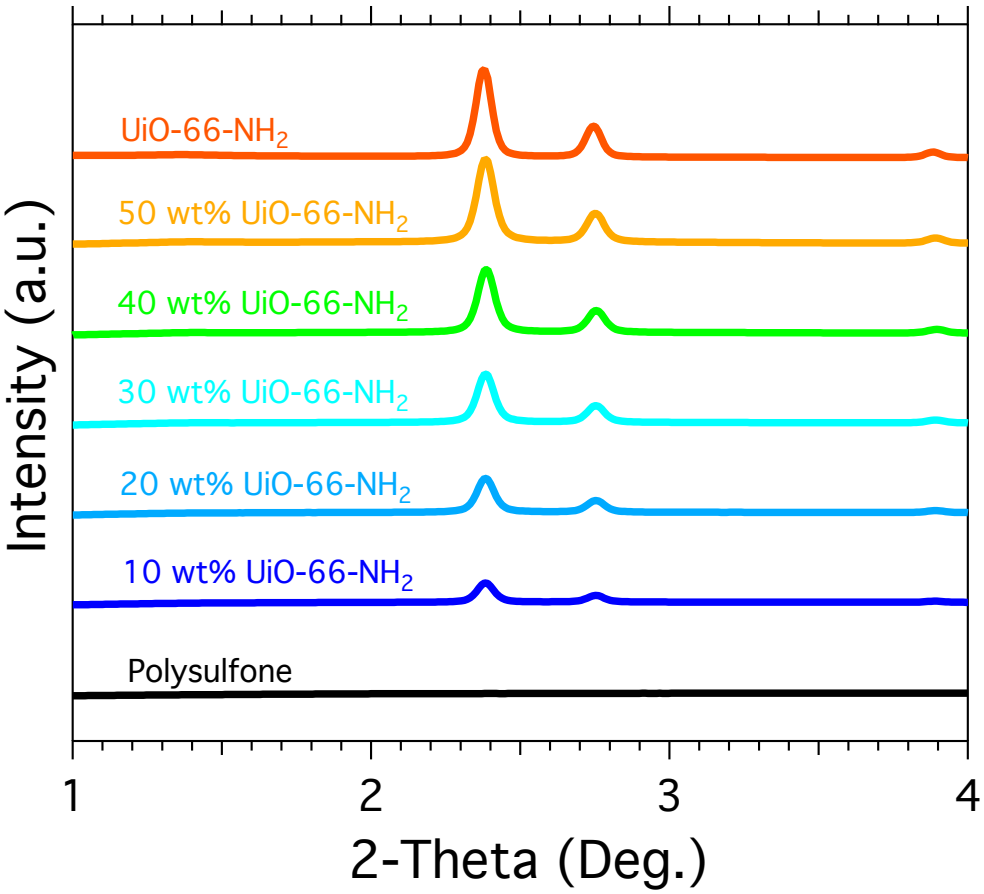

Figure 4.5. X-ray diffraction patterns of UiO-66-NH_2 and hybrid membranes containing 0 to 50 wt% UiO-66-NH_2. Maximum peak intensities of hybrid membranes correlate well with MOF loading after normalization with membrane thickness.

CO_2 adsorption isotherms of the hybrid membranes are collected at 25 °C as shown in **Figure 4.6**. UiO-66-NH_2 powder exhibits a measured CO_2 adsorption of 2.91 mmol/g at 1 bar and matches well with literature.[17] Similar to the XRD patterns, the total CO_2 adsorption correlates well with the MOF loading in the membranes. 50 wt% UiO-66-NH_2 membranes exhibit a CO_2 adsorption equivalent to 53% of the total CO_2 adsorption of just UiO-66-NH_2. Hybrid membranes containing 10, 20, 30, and 40 wt% UiO-66-NH_2 have CO_2 adsorption uptakes, which are 11%, 23%, 31%, and 37% of UiO-66-NH_2 only, respectively. The consistency of CO_2 uptakes with weight loading in these hybrid membranes is evidence of no pore blockage due to polymer chains. Pore blockage of porous materials by polymer chains is a major concern in hybrid membranes because it is known to be detrimental to the gas transport.[75,144] Depending on the pore size, polymer chains can completely or partially infiltrate the pores of the MOF. Instead of gas molecules diffusing through the MOF, molecules would be forced to travel around the pore-blocked MOF, thereby increasing tortuosity and decreasing diffusion and permeability. As a result, I do not anticipate that pore blockage is detrimentally affecting the gas transport performance of the hybrid membranes.

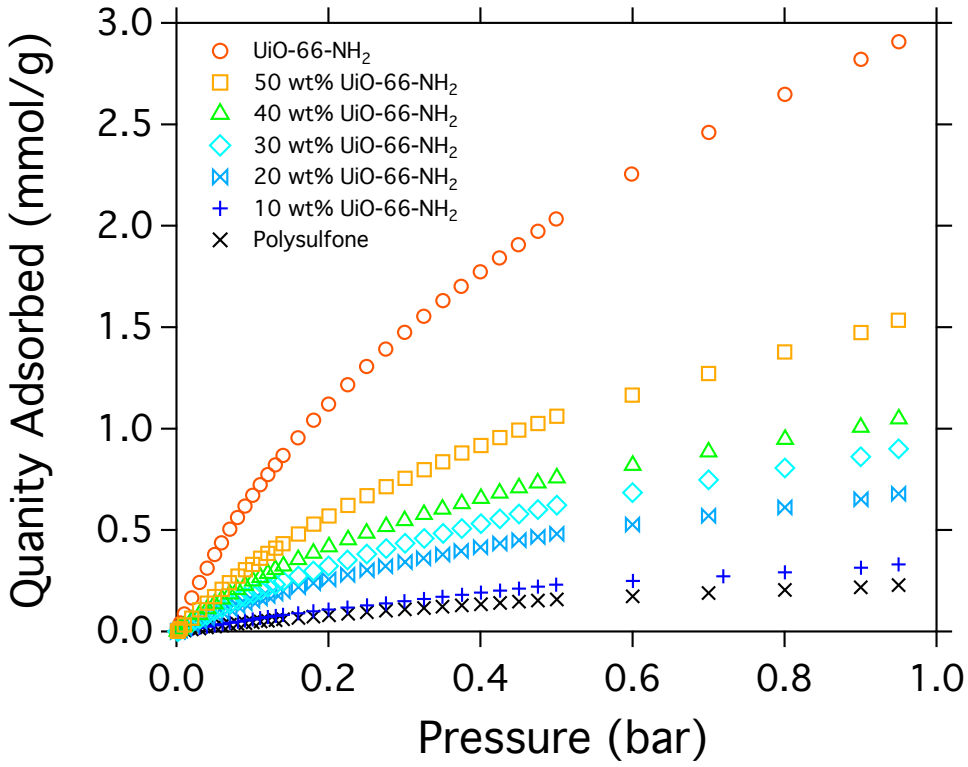

Figure 4.6. CO_2 adsorption isotherms of UiO-66-NH_2 and UiO-66-NH_2 containing membranes at 25 °C. Total CO_2 adsorption of membranes containing UiO-66-NH_2 scale with MOF loading.

4.3.3 Gas Transport Properties

Pure gas permeability and selectivity of N_2, CH_4, and CO_2 at 35 °C and 3 bar are shown in **Figure 4.7** and **Figure 4.8**, respectively, as a function of weight % of UiO-66-NH_2. All hybrid membranes exhibited at least 200% higher permeability than the permeability of neat polysulfone membranes. Surprisingly, I observe a significant increase in permeability from hybrid membranes containing 30 wt% to 40 wt% MOF. At 30 wt%, the CO_2 permeability is 18 barrer or 3.3 times higher than polysulfone only. However, at 40 wt%, the CO_2 permeability dramatically leaps to 46 barrer or 8.1 times higher than neat polysulfone. The leap in permeability is not consistent with the linear behavior between 0 and 30 wt%, in which CO_2 permeability gradually increases from 5.6 to 18 barrers.

In order to understand the permeability trends in the hybrid MOF membranes, I perform analysis using a simple effective medium model. Such models often capture the physical behavior of a broad range of systems with a continuous phase and a dispersant.[41] Specifically, permeability in heterogeneous two-phase materials are frequently modeled by Maxwell's model (Eqn. 4.2)[77],

$$P_{Maxwell} = P_p \frac{nP_d+(1-n)P_p-(1-n)\phi_d(P_p-P_d)}{nP_d+(1-n)P_p+n\phi_d(P_p-P_d)} \quad (4.2)$$

which consider the volume loading of the dispersed phase (i.e. MOF), ϕ_d, and the geometry shape factor of the dispersed phase, n, as the only adjustable parameters. $P_{Maxwell}$, P_p, and P_d are the permeability of the hybrid membrane, polymer, and dispersed phase, respectively. While the simplicity of the model allows for quick comparison of experimental data to the predicted values, the model does not consider the effects of interphase interactions, is typically applied only to systems below 20 vol% loading, and usually assumes the dispersed phase has spherical geometry (n = 1/3).[77] In this scenario, Maxwell's model collapses into the more common Maxwell's equation used in hybrid or composite membrane analysis. From our density measurements, I calculated the bulk density of UiO-66-NH_2 to be 1.53 g/cm^3, which is close to the estimated density of 1.3 g/cm^3 for a perfect crystal and ideal unit cell.[145] Assuming the experimental density, I find that hybrid membranes contain a maximum of 45 vol% MOF, which is well beyond the 20 vol% threshold for typical applications of Maxwell's model. However, I can still apply Maxwell's equation (n = 1/3) in hybrid membranes containing below 30 wt% (25 vol%) UiO-66-NH_2 as shown in **Figure 4.9**. The equation severely underestimates permeability values by up to 44%, even when assuming an infinitely permeable dispersed phase. Gas permeability of UiO-66-NH_2 has not been previously measured before, and thus, there is not an accepted literature value to use as P_d. I speculate that the poor prediction of Maxwell's model could arise from one of two possibilities. First, poor interactions between the polymer and MOF can result in interphase voids, which act as fast non-selective diffusive pathways. However, our T_g measurements and SEM images indicate the opposite, where good interfacial interactions are present. Second, our approximation of spherical geometry of the dispersed phase could be incorrect. This scenario is more likely than the former and is at least suggested by partial aggregation observed in SEM images (Figure 4.2 and 4.3). Allowing the shape factor, n, to be an adjustable parameter, I find Maxwell's model closely approximates experimental values below 30 wt% when n is equal to 0.14, equivalent to elongated ellipsoid oriented parallel to transport direction, and P_d varies between 500 and 1000 barrers, as shown in **Figure 4.10**. However, the model is still not a good predictor above 30 wt%, which would be expected given the model's assumptions and hybrid systems, which oftentimes manifest new properties that cannot be simply modeled using effective medium analysis.

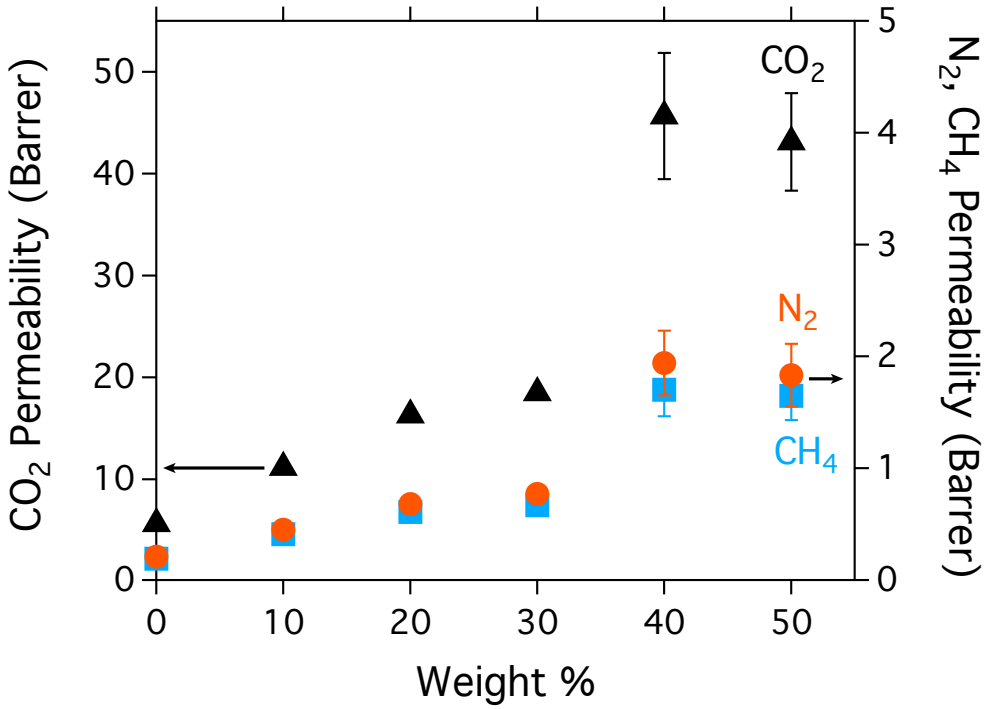

Figure 4.7. Pure gas permeabilities of CO_2 (triangles) , N_2 (squares), and CH_4 (circles) at 3 bar and 35 °C of hybrid UiO-66-NH_2 polysulfone membranes as a function of weight % of the MOF. There is a dramatic jump in permeability between 30 and 40 wt% due to percolative network of MOF crystals. Error bars represent a single standard deviation.

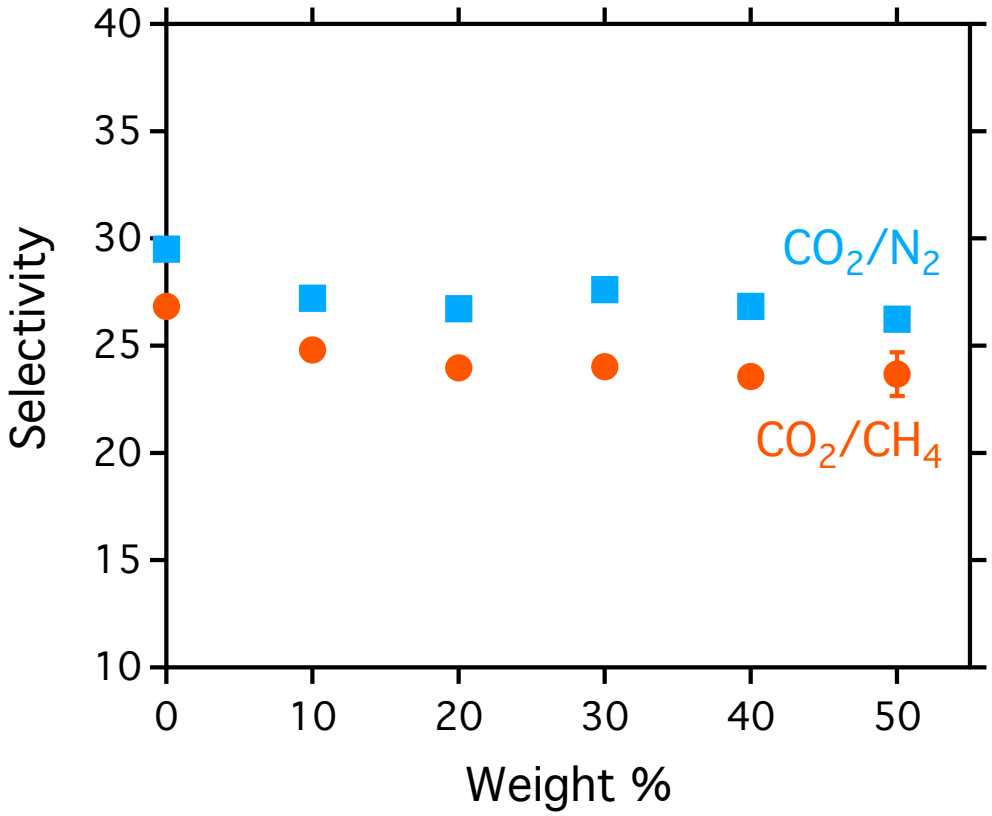

Figure 4.8. Ideal CO_2/N_2 (squares) and CO_2/CH_4 (circles) selectivities obtained from the hybrid UiO-66-NH_2 polysulfone membranes at 3 bar and 35 °C as a function of weight % of the MOF. Selectivity effectively remains constant with addition of UiO-66-NH_2. Error bars represent a single standard deviation.

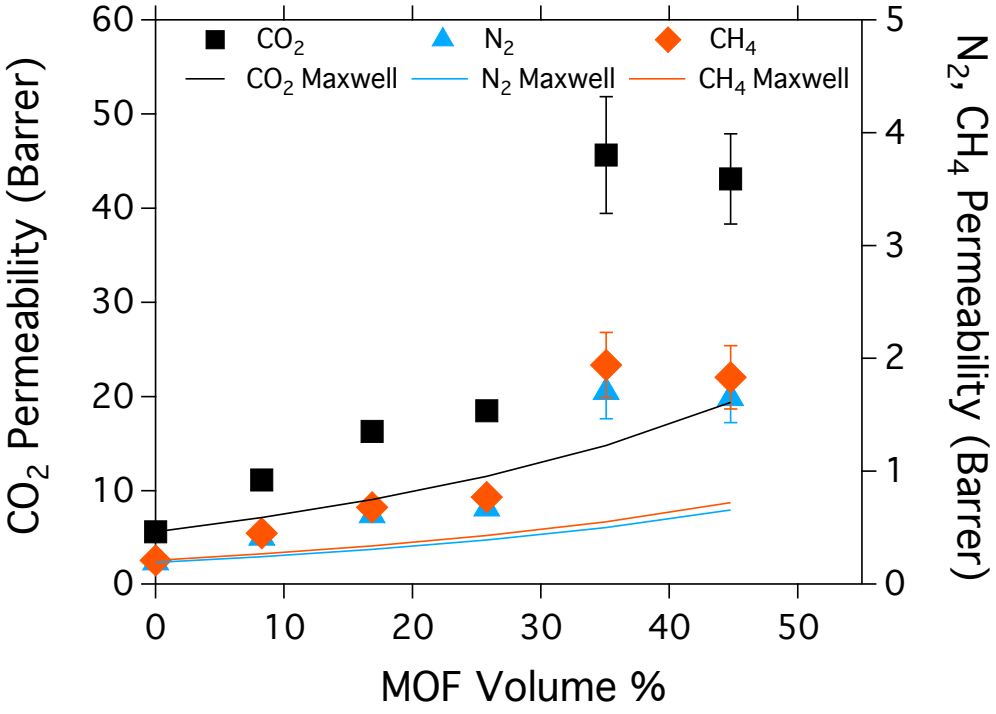

Figure 4.9. Comparing Maxwell's predicted permeability with a spherical shape factor of n = 1/3 and $P_d = \infty$ to experimental permeability. Maxwell's permeability consistently underestimates permeability for CO_2, N_2, and CH_4; this breakdown in the predictive value of the model is accentuated for high MOF loadings.

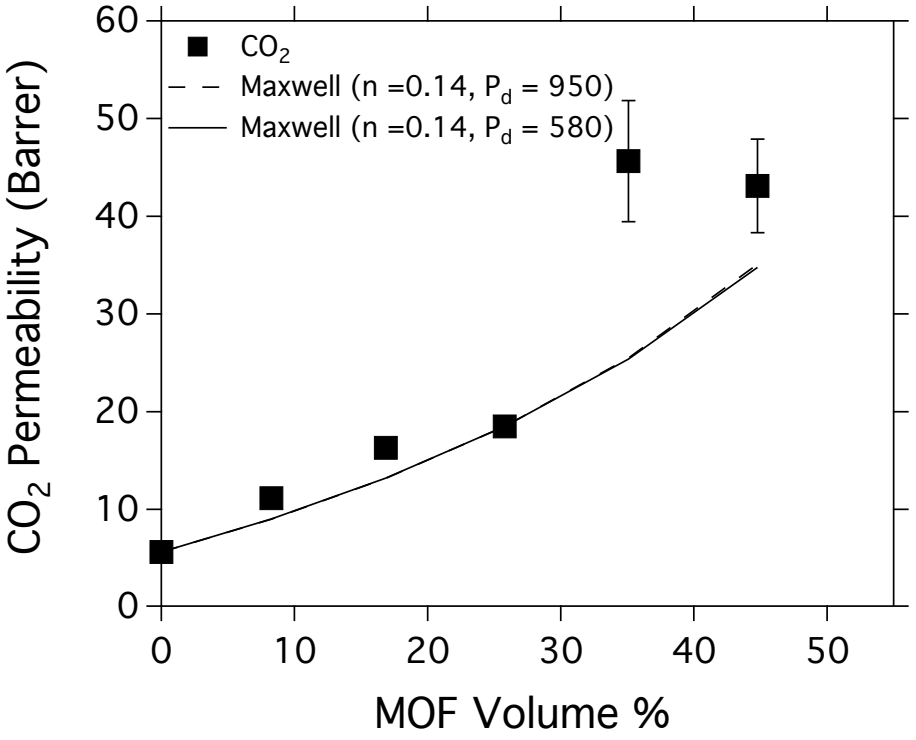

Figure 4.10. Comparing Maxwell's permeability with an adjustable shape factor. n converges to 0.14. Permeability of UiO-66-NH_2 ranges from 500-1000 barrers. Maxwell permeability trends shown for 580 and 950 barrer. Excellent correlation with experimental permeability below 30 wt%.

The dramatic increase in permeability in hybrid membranes when loading is increased from 30 to 40 wt% UiO-66-NH_2 is postulated to arise from the formation of a percolative network of MOF crystals throughout the membrane, whose effect is not captured in effective medium models. Percolation is reached when the dispersed phase surpasses a threshold volume fraction, forming an interconnected network, which spans across the entire system. Below this value, no interconnectivity across the entire system is present. The percolation threshold depends on the dimensionality of the system as well as the shape and aspect ratio of the discontinuous phase. A shape factor, n, of 0.14 suggests that the ellipsoids will have an aspect ratio between 2 and 3 and this is suggested by SEM images of MOF nanoparticles (**Figure 4.11**).[146] Applying the percolation model theorized for ellipsoids by Garboczi *et al.*[133], percolation is expected to occur between 26 and 31 vol%. This threshold overlaps with volume loading of 30 wt % (25 vol%) and 40 wt% (35 vol%) hybrid membranes, indicating that I are in the percolation regime at 40 and 50 wt%. The cross-section SEM images (Figure 4.2 and 4.3) show a visible change in morphology wherein regions of interconnected network of MOF crystals appear. This concept is illustrated in **Figure 4.12** when both the polymer and MOF exhibit continuity across the membrane. As a result, molecular transport through the MOF acts as a transport highway exhibiting higher diffusivity over solution-diffusion transport through the polymer. The higher permeation rates through the MOF are due to crystalline microporous structure,

which is governed by a transport mechanism closely resembling molecular sieving. The pore size of UiO-66-NH_2 is between 6-7 Å and is larger than the average kinetic diameters of the gas molecules explored (CO_2 (3.3 Å), N_2 (3.64 Å), and CH_4 (3.8 Å)).[23,145] The pore size to molecular size ratio does not constitute transport by molecular sieving that typically displays much higher selectivity values than polymer systems. However, Knudsen transport is not likely because the mean free path of the largest gas molecule, CH_4, is over two orders of magnitude higher than the pore size; additionally, the observed selectivities are much higher than expected for materials that typically fall within the Knudsen regime.

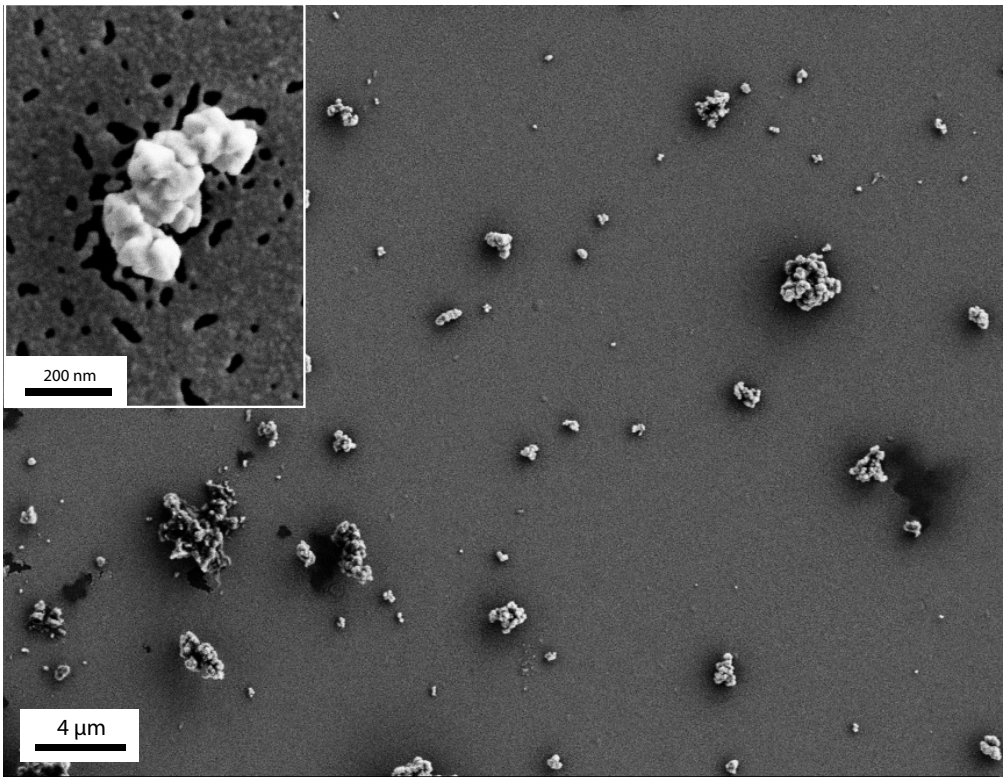

Figure 4.11. SEM image of UiO-66-NH_2 nanoparticles. I observe partial aggregation of smaller domains of UiO-66-NH_2, which results in presence of elongated UiO-66-NH_2 ellipsoids (inset) consistent with percolation theory.

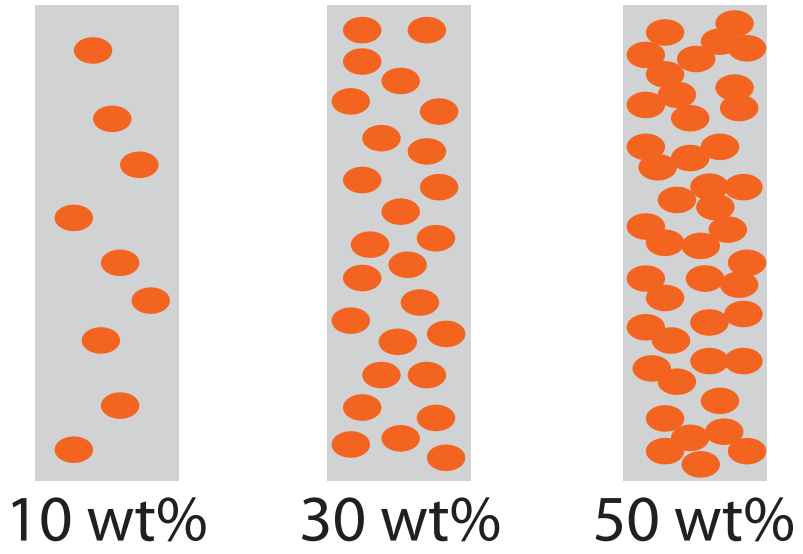

Figure 4.12. Schematic of formation of percolative interconnected network of MOF crystals with ellipsoid geometry. Interconnected network of MOF crystals is formed when percolation threshold is reached.

The selectivity of CO_2 over N_2 and CH_4 is shown in Figure 4.8. The CO_2/N_2 and CO_2/CH_4 selectivity of pure polysulfone is 30 and 27, respectively, and are similar to those previously reported in literature.[97] As UiO-66-NH_2 is added to reach 10 wt% loading there is an initial decrease in CO_2/N_2 and CO_2/CH_4 selectivity of just 8%. As loading is increased to 50 wt% MOF, the selectivities have only decreased 12% from the polymer only membranes. Coupled with the large increase in permeability, the collective separation performance in these hybrid membranes is greatly enhanced over neat polysulfone and moves closer towards the Robeson upper bound line (**Figure 4.13**). Surprisingly, the stability of CO_2/N_2 and CO_2/CH_4 selectivity and large increase in CO_2 permeability has not been readily seen in the hybrid membrane literature for carbon capture applications as the transport properties are still primarily governed by the solution-diffusion model. A comparison of our results to those in literature is listed in **Table 4.2**. I find that our system provides the largest increases in permeability without sacrificing permeability. Reports that do show similar performance improvements are isolated to a few studies involving olefin-paraffin separation processes.[51,125] Further, the recent work by Smith *et al.*[122] suggests that metallation of the MOF can lead to enhanced interactions and structural changes in the polymer that can further improve or separation performance and will be important in our future design of hybrid membranes.

Table 4.2. Selected CO_2 permeability % increase and selectivity values of hybrid membranes reported in literature and this work.

Material	Inorganic Loading	CO_2 Permeability Increase	CO_2/CH_4	CO_2/N_2	Ref.
PSF/UiO-66-NH_2	50 wt%	770%	24	26	This Work
PI/ZIF-8	40 wt%	155%	27	23	Ordonez et al.[119]
PI/Mg(dodbc)	10 wt%	30%	-	23	Bae et al.[75]
PIM-1/UiO-66-NH_2(Ti)	5 wt%	370%	-	21	Smith et al.[122]
PI/ZIF-8	30 wt%	255%	25	17	Song et al.[123]
PI/Silica	30 wt%	156%	238	41	Suzuki et al.[55]
PI/CMS	36 wt%	26%	52	33	Vu et al.[39]
PI/CMS	36 wt%	210%	53	33	Vu et al.[39]
PB/MgO	60 wt%	1000%	4.1	7.8	Matteucci et al.[89]

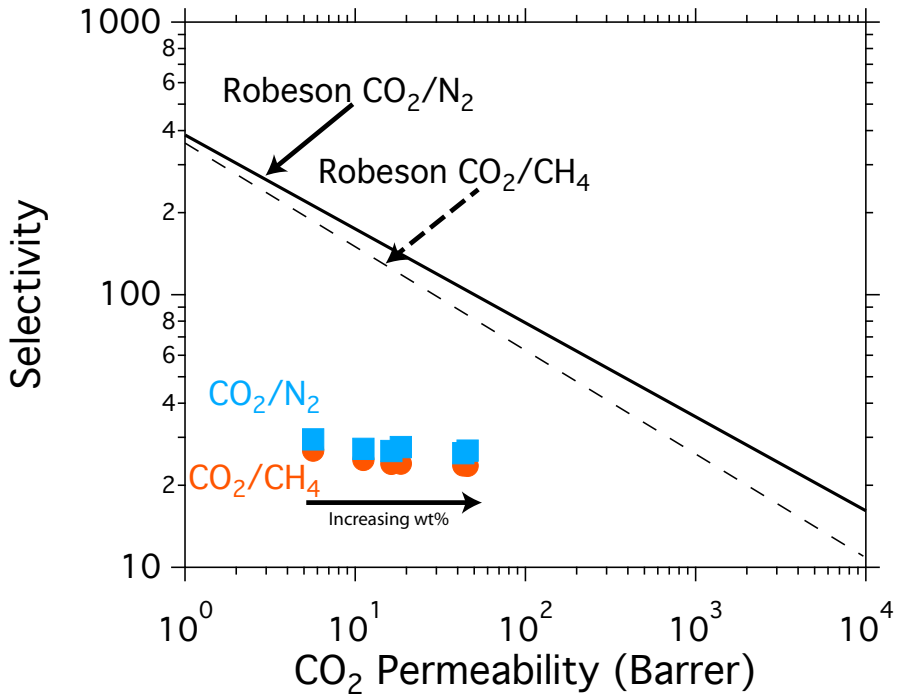

Figure 4.13. Robeson upper bound plot of UiO-66-NH_2 PSF hybrid membranes for CO_2/N_2 and CO_2/CH_4. In both cases, the addition of MOF moves the transport performance of the hybrid membrane closer to the upper bound line.

To better understand the changes in the transport mechanism, I investigate diffusivity values for hybrid membranes as a function of weight % as shown in **Figure 4.14**. Diffusion coefficients were estimated by permeation time-lag experiments.[96] As expected, the

diffusion coefficient scales inversely with the kinetic diameter of the gas molecule. CO_2 has the highest diffusion coefficient, while CH_4 has the lowest diffusion coefficient. The CO_2 diffusion coefficient gradually rises from $1.1*10^{-8}$ cm^2/s to $1.7*10^{-8}$ cm^2/s in membranes containing 0 to 30 wt% MOF. Interestingly, after 30 wt%, the diffusion coefficient jumps to above $2.9*10^{-8}$ cm^2/s with membranes containing 40 and 50 wt% UiO-66-NH_2; this trend is similarly observed for N_2 and CH_4 as well. Thus, this jump is consistent and what is expected as a parallel transport pathway of interconnected MOF crystals is introduced, because diffusion through rigid porous materials is generally higher than that of amorphous polymers. The activation energy for molecular diffusion through rigid porous media is typically lower, because diffusion is not dependent on random thermal fluctuations as found in polymers. I find that the activation energy for diffusion drops significantly upon exceeding the percolation threshold (**Figure 4.15**).

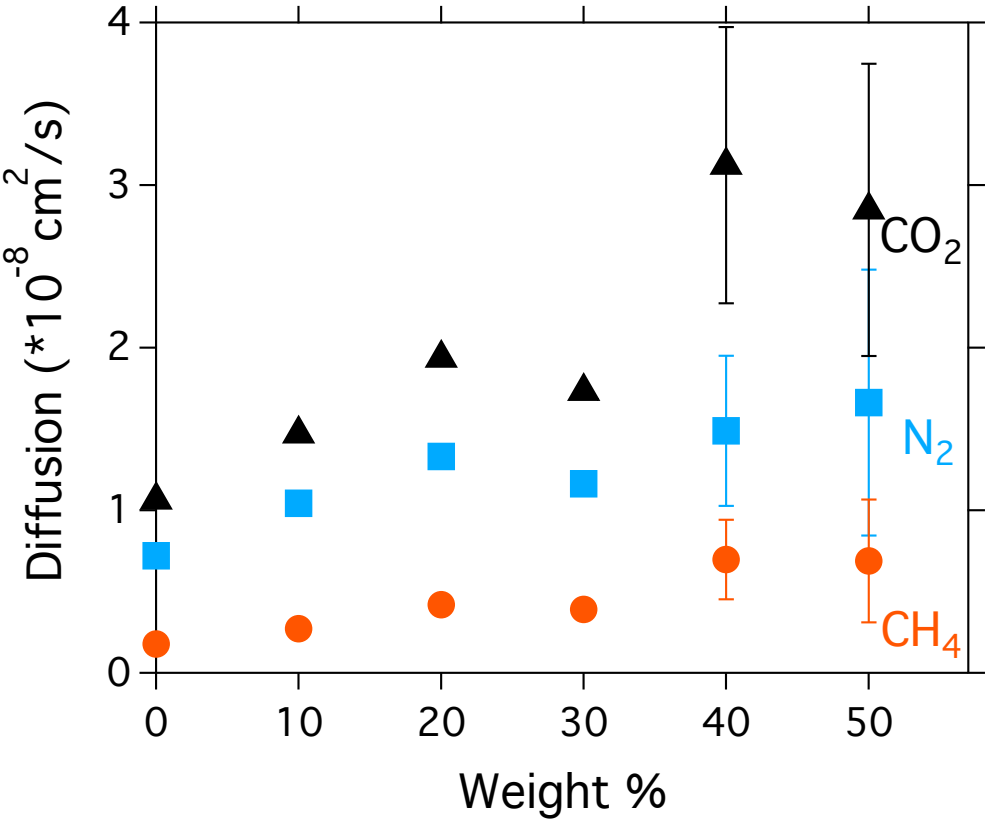

Figure 4.14. Diffusion coefficients of CO_2 (triangles), N_2 (squares), and CH_4 (circles) at 3 bar and 35 °C as a function of UiO-66-NH_2 loading in hybrid membranes. Diffusion coefficient jumps between 30 and 40 wt% MOF due to the formation of interconnected MOF crystal network.

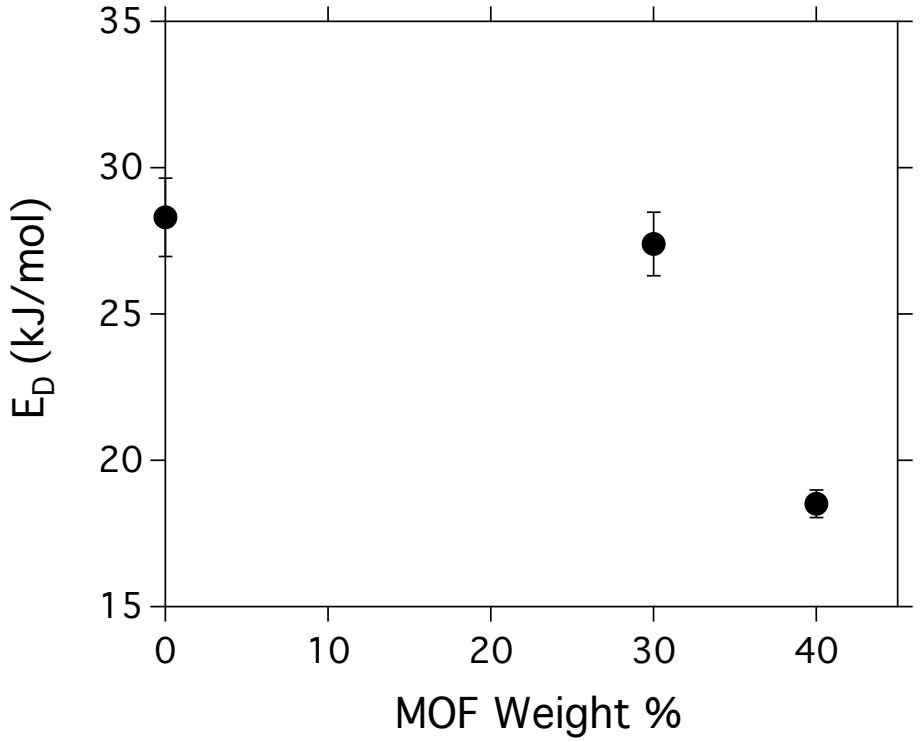

Figure 4.15. CO_2 activation energy for diffusion, E_D as a function of MOF weight %. Under the percolation threshold(up to 30 wt% MOF), the activation energy shows no significant decrease. Over the percolation threshold (over 40 wt% MOF), E_D drops significantly due to the formation of dual transport pathways.

The solution-diffusion model is most commonly used to describe molecular transport through dense polymer membranes[23,30] From this model, one defines the permeability of a gas through a polymer (P) as the product of both a kinetic term (diffusivity, D) and a thermodynamic term (solubility, S), or simply P = DS.[23,30] While the model may not be appropriate towards understanding transport mechanisms in hybrid membranes, it can still be a useful tool to provide qualitative solubility trends in hybrid membranes. Using the permeability and diffusivity data collected, I can employ the P=DS relationship to calculate S, which is plotted as a function of weight % in **Figure 4.16**. The overall solubility trend is consistent with observed trends where solubility increases as the critical temperature of gas species increases ($T_{c,CO2} > T_{c,CH4,} > T_{c,N2}$). Unsurprisingly, the solubility exhibits a linear increase as MOF loading increases. For CO_2, the solubility increases from 4 cm^3 (STP)/(cm^3 atm) in pure polysulfone up to 12 cm^3 (STP)/(cm^3 atm) in 50 wt% UiO-66-NH_2, representing a 3 fold increase. Solubility is expected to increase in hybrid membranes with the addition of porous and high surface area materials such as UiO-66-NH_2 as they are more tailored for adsorption of molecular species. The solubility of gas in any material system is a thermodynamic value and should not be dependent on any morphological changes in the membrane due to addition of a secondary phase, as was seen with diffusion. As a result, the adsorption capacity of these hybrid membranes depends only on the relative loading of polymer and MOF as was seen similarly in CO_2 adsorption isotherms (Figure 4.6).

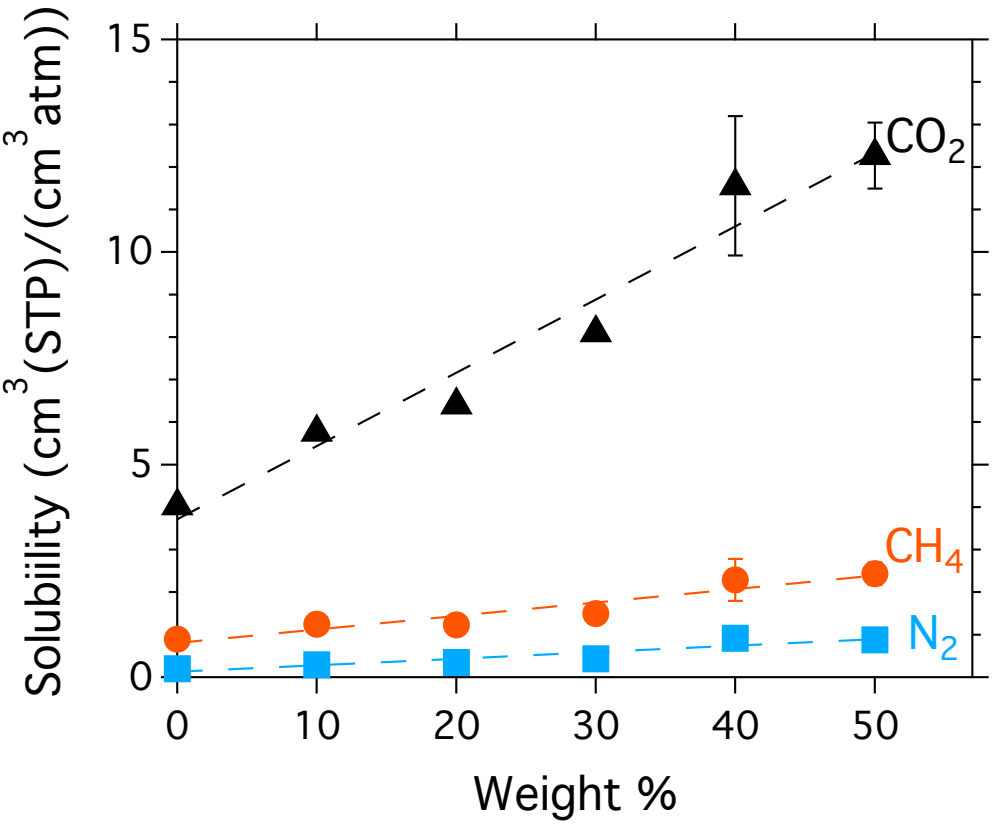

Figure 4.16. Solubility coefficients of CO_2 (triangles), N_2 (squares), and CH_4 (circles) at 3 bar and 35 °C as a function of UiO-66-NH_2 loading in hybrid membranes. Solubility shows a linear relationship with weight %. The dotted lines are linear regression fits of the data.

4.4 Conclusion

I demonstrate for the first time the formation of dual transport pathways in hybrid polymer/MOF membranes and investigate its evolution as it relates to percolation transition. The formation of dual transport pathways requires high loading of the inorganic phase, which often leads to mechanical failure of the membrane. Using polysulfone and UiO-66-NH_2, I am able to maintain structural integrity of the membranes even at very high loadings (50 wt%). Further, the transport properties associated with dual transport membranes are distinctively different than conventional mixed-matrix membranes, which contain discontinuity with the inorganic phase. Thus, in dual transport membranes, gas transport through the MOF acts as a molecular transport highway and complements classical solution-diffusion through the polymer. Below the percolation threshold, permeation properties of the hybrid membranes are higher than the pure polymer and could easily be fitted to a classical effective medium model. However, above the percolation threshold, permeation properties far exceed what the model could predict and signify a new, non-classical dual transport regime. I find for our hybrid system that dual transport pathways develop between 30 and 40 wt% UiO-66-NH_2. In the percolative regime, CO_2

permeability rises to a remarkable 46 barrers; a 8-fold increase over pure polysulfone. Additional evidence of dual transport pathways is found in a similar phenomenon in CO_2 diffusion as I surpass the percolation threshold. Furthermore, our hybrid membranes deviate from conventional permeability/selectivity trade-off relationships as selectivity over methane and nitrogen remained near that of polysulfone at 22 and 25, respectively. The unique discovery of engineering dual transport pathways enables new approaches towards designing hybrid membranes to significantly improve gas separation performance.

4.5 Acknowledgements

X-ray diffraction measurements were collected at the Advanced Light Source, Beamline 12.2.2. Work at the Molecular Foundry and the Advanced Light Source was supported by the Office of Science, Office of Basic Energy Sciences, of the U.S. Department of Energy under Contract No. DE-ACO2-05CH11231. N.S. was supported by the Department of Defense (DoD) through the National Defense Science & Engineering Graduate Fellowship Program. D.S was supported by Lawrence Berkeley National Laboratory Laboratory-Directed Research and Development Program. W.Q was supported by U.S. Department of Energy, Office of Basic Energy Sciences, Division of Chemical Sciences, Geosciences and Biosciences under Award DE-FG02-12ER16362.

4.6 Supporting Information

Supporting information for this chapter can be found in Appendix A.3.

Chapter 5. Designing Highly Selective Thin-Film MOF Membranes for CO2 Capture

Fabrication of stand-alone metal-organic framework membranes is challenging due to current solvothermal-based synthetic techniques, resulting in a powdered product. By coupling a MOF layer to a flexible polymer support, I can significantly enhance the design tunability and modularity of the membrane. Adapting the principles gained from the previous chapters and work with hybrid membrane, I show and report a new paradigm to form thickness-controlled CO2 selective MOF membranes. This new class of membranes exhibits superior selectivity over current rigid supported MOF membranes.

5.1 Introduction

In 2013, nearly 24% of the total global energy consumption is derived from natural gas sources, second only to petroleum, equivalent to over 120 trillion scf.[4,147] Natural gas is a cleaner source of energy compared to conventional carbon-based fuels (e.g. biomass, coal, petroleum) due to its low carbon:hydrogen ratio. As a result, natural gas has a high specific energy and emits lower amounts of carbon dioxide per unit of energy produced. However, an increasingly higher fraction of raw or sour natural gas needs to be processed and purified before being transported through pipelines to end-users. Approximately 20% of all natural gas contains concentrations of carbon dioxide above the threshold (2%) to be transported through pipelines.[148] If left untreated, carbon dioxide and other contaminants present in natural gas will lead to pipeline corrosion and increased operational costs. Current methods to remove carbon dioxide using amine-based absorption processes are proven but are energy intensive and require constant monitoring of the process due to corrosion. Membranes-based separation processes have emerged as an attractive alternative owing to their low parasitic energy costs.[21] However, separation efficiencies of conventional polymer-based membranes are hindered by plasticization of the polymer by highly soluble gases such as carbon dioxide.[23] Plasticization occurs when the penetrant gas concentration in the polymer causes free volume to increase often resulting in a large decrease in diffusive selectivity.

Metal-organic frameworks (MOFs) are a relatively new class of microporous 3-D crystalline materials composed of metallic clusters connected by organic linker molecules.[25,135] Unlike previously explored microporous materials such as carbon molecular sieves and zeolites, MOFs offer significantly higher chemical flexibility to tune the material for specific gas separation needs based on pore-size and chemical interactions. Recently, membranes whose selective component is solely derived from MOFs have shown promising separation properties that exceed the performance of polymer membranes and do not suffer from plasticization effects.[149–152] This is because MOF membranes discriminate between molecular species through a molecular sieving mechanism, rather than a solution-diffusion mechanism typical in polymer membranes, which affords much higher selectivity values and minimal plasticization effects. However, implementation of MOFs as a full-scale membrane device has thus far been constrained due to mechanical brittleness, which presents challenges to large-scale fabrication. To bypass this constraint, MOF crystallites are dispersed into a polymer matrix forming hybrid or mixed-matrix membranes.[45,122,123,129,153–157] These hybrid systems combine the solution processability advantages of polymers and high molecular selectivity of MOFs, while also having to potential to foster new properties and functionalities from synergistic enhancements. I recently show that hybrid membranes can possess dual transport pathways through the polymer and MOF and exhibit exceptionally high separation performance due to the formation of a percolative MOF network.[153] While promising, the performance of hybrid membranes is still limited by the polymeric component, thereby necessitating the ultimate goal of a developing and designing MOF only membranes.

There are a variety of methods to fabricate MOF films including direct growth[158,159], secondary growth[160–163], and layer-by-layer (LBL)[164–169] techniques. Of these methods, direct growth and secondary growth are most widely employed owing to their ease and conformity to traditional solvothermal synthesis techniques. Often, however, the MOF membrane layer is thick and its thickness cannot be readily controlled due to the reaction conditions. Conversely, the LBL growth method enables precise control of the MOF thickness. In this approach, the support is immersed in a solution of metal ions, washed with a solvent, and immersed in a solution of the organic ligands. The process is repeated until the desired thickness is obtained and a defect-free membrane produced. An ideal MOF candidate for membrane gas separations is ZIF-8 as its pore size (3.4 Å) is falls within the kinetic diameters of many molecular species of interest in gas separation.[170] For instance, the kinetic diameter of CO_2 and CH_4 are 3.3 Å and 3.8 Å, respectively, making ZIF-8 theoretically selective for CO_2 over CH_4. However, as a membrane, the CO_2/CH_4 selectivity is very modest (3-7) and even reverse selective.[18,158,162,164,171–173] ZIF-8 membranes do exhibit high selectivity for separation of propene from propane.[161] Further, the supports most often used in the fabrication of MOF membranes are rigid porous alumina membranes. As a result, the design flexibility of MOF membranes becomes significantly constrained to the geometry of the support.

5.2 Experimental Procedure

Polyaniline Film preparation. Polyaniline is directly polymerized onto a polypropylene support (Celgard) using previously published procedures.[174,175]The surface of PANI film is photografted with a solution containing 5% benzophenone in methanol. The film is then irradiated for a time 4 min. Non-functionalized, bare quartz plate is used to cover the surface. After photografting, the film is washed with methanol and dried.

Additionally, the PANI layer is wetted with a photografting mixture consisting of 1-vinyl imidazole (50 wt%) and 3:1 v/v t-butyl alcohol-water mixture (50 wt%). The film is placed between two quartz plates whose surface is fluorinated to prevent sticking. The quartz plates are fixed with clamps and positioned under a deep UV lamp at 360 nm (Hg/Xe 500W short-arc lamp UXM-501MA, Ushio America) at a distance of 23 cm for 15 min. After completion of the UV exposure, the quartz plates are carefully removed and the membrane is immediately immersed in 1,4-dioxane for about 1 h to dissolve all soluble polymers, then washed with methanol, and dried.

ZIF-8 Thin Film Preparation. PANI films functionalized with 1-vinyl imidazole were immersed subsequently in a 100 mM of $Zn(NO_3)_2$*6H2O methanol solution for 2 minutes and in a 50 mM 2-Methylimidazole (mIm) methanol solution for 3 minutes at room temperature. Between each step the substrates were rinsed with methanol and dried in a nitrogen stream. The process is repeated until the desired thickness is obtained

Scanning Electron Microscopy. Cross-sectional and top-down imaging of the membranes is acquired using a Zeiss Gemini Ultra-55 Analytical Scanning Electron Microscope at an accelerating voltage of 5 keV.

X-ray Photoelectron Spectroscopy. A PHI 5400 ESCA system (PerkinElmer, Waltham, MA, USA) including an Al anode (primary photon energy of 1486.6 eV) and an X-ray source with a power of 150 W (15 kV at 10 mA). Sputtering of an area of 2×2 mm^2 was performed with an Ar^+ ion gun (Beam Voltage 3000 V, Emission Current 25 mA). Membranes were dried prior these measurements at room temperature for 24 hours.

Gas Permeance Measurements. Pure gas CO_2 and CH_4 permeance measurements are collected using a custom built constant volume/variable pressure system. The films are masked with brass discs to accurately define an area through which gas transport could occur. Prior to testing, the films are degassed within the apparatus. A fixed pressure is applied to the upstream side of the membrane, while the gas flux is recorded as a steady-state pressure rise downstream of the membrane. Permeability values are calculated as follows:

$$P = \frac{V_D l}{p_2 ART}\left(\frac{dp_1}{dt}\right) \qquad (5.1)$$

where V_D is the downstream volume (cm^3), l is the film thickness (cm), p_2 is the upstream pressure (cmHg), A is the exposed area of the film (cm^2), R is the gas constant, T is the absolute temperature (K), and dp_1/dt steady state pressure rise downstream at fixed upstream pressure (cmHg/sec). The measurements are obtained under isothermal conditions at 308 K.

5.3 Results and Discussions

Utilizing the LBL growth method, I report on the development of flexible thin film ZIF-8 membranes solvated with the room temperature ionic liquid (RTIL), 1-hexyl-3-methylimidazolium bis(trifluoromethylsulfonyl)imide ([C6mim][T2fn]). These membranes exhibit high selectivity for carbon dioxide over methane. **Figure 5.1a** illustrates the scheme towards synthesizing ZIF-8 onto the support membrane. To achieve the desired flexibility of the membrane, I chose to use an asymmetric polyaniline (PANI)/polypropylene (PP) membrane as the support. PANI is polymerized directly onto the PP into a dense structure following previously reported procedures.[174,175] The thickness of the PANI layer is on average 150 nm as measured by cross-sectional SEM imaging. The PP layer is necessary to provide mechanical strength to both the PANI and ZIF-8 layers, while the PANI layer serves two purposes. Previous work with PANI thin film membranes has shown exceptionally high CO_2 separation properties when the membrane is solvated with water or polyethylene glycol.[175,176] Further, the PANI surface is photografted with benzophenone and 1-vinylimidazole to allow ZIF-8 to be covalently grown onto the support. Layers of ZIF-8 are then grown on the modified surface by first immersing the modified PANI/PP membrane into a 100 mM solution of zinc nitrate hexahydrate in methanol, rinsed with methanol, and dried. The membrane is then immersed into a 50 mM solution of 2-methylimidazole in methanol, rinsed with methanol and dried. The process is repeated for 10, 20, or 30 cycles. The LBL growth method is highly advantageous over other methods because it provides precise control over the thickness of the deposited layer. As seen in **Figure 5.1b**, the ZIF-8 layer thickness is directly proportional to the number of deposition cycles. 10 cycles equates to a ZIF-8 thickness of 290 nm (ZIF-8/290); 20 cycles equates to a ZIF-8 thickness of 500 nm (ZIF-8/500); and 30 cycles equates to a ZIF-8 thickness of 900 nm (ZIF-8/900).

While the LBL growth method can generate dense, defect-free membranes, often, the method produces membranes with micro-defects that span across the direction of gas transport.[167,169,173] Initial gas transport measurements of ZIF-8 and PANI membranes indicate presence of micro-defects resulting in non-selective transport properties. Thus to seal the defects, a layer of [C6mim][T2fn] is coated onto the ZIF-8 surface by spin coating with a 50 vol% solution with methanol. In addition, [C6mim][T2fn] can also serve as a secondary facilitated transport carrier for CO_2. [C6mim][T2fn] is chosen because of its known solubility selectivity of CO_2 over CH_4; its chemical structure is shown in **Figure 5.1c.**[177,178]. In facilitated transport, the gaseous species undergoes a reversible chemical interaction with a carrier species in the membrane that shuttles the molecules across the membrane. In this case, [C6mim][T2fn] acts as a mobile carrier for CO_2.

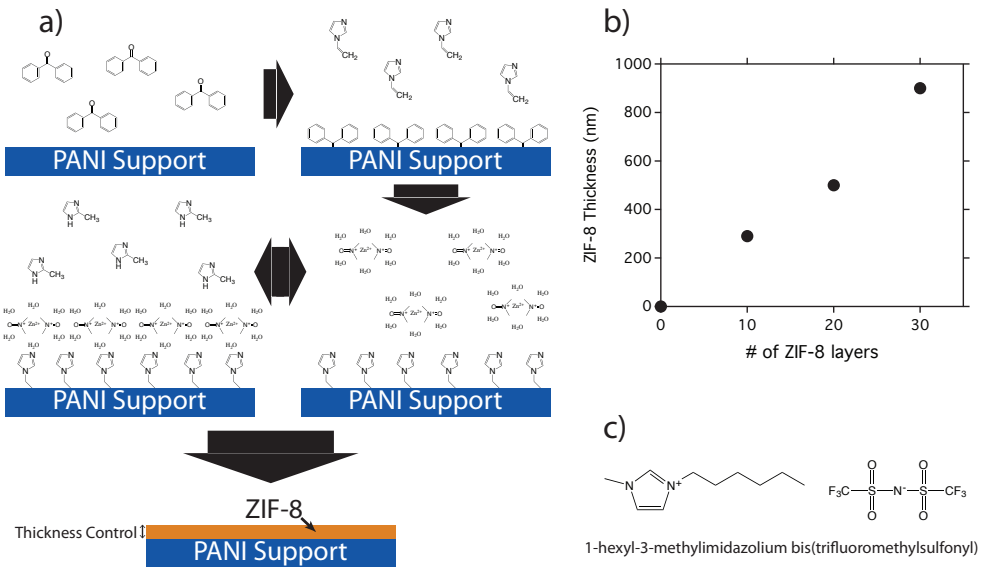

Figure 5.1. a) Schematic illustrating the layer-by-layer growth method of ZIF-8 membranes. The number of cycles dictates to total overall thickness of the MOF layer. b) ZIF-8 thickness scales linearly with the number of ZIF-8 layers synthesized. c) Chemical structure of the RTIL, [C6mim][T2fn].

SEM images of the membrane surface before and after deposition of the ZIF-8 layer are presented in **Figure 5.2**. The PANI support layer (Figure 2a) exhibits a granular morphology with some precipitated PANI granules present on the surface. The average size of these granules is 15 nm. The granular morphology is continued into the ZIF-8 membranes, in addition to the appearance of larger topological features in the ZIF-8 layer. Larger island domains (300-400 nm) can be observed and is covered by small granules of ZIF-8 that are on average 18 nm in size. While it is difficult to differentiate between ZIF-8 and PANI granules, I note that the granular morphology in ZIF-8/290 is more clearly distinct. The concentration of larger domains increases as the number of ZIF-8 cycle increases. The average size of the small granules is 18 nm and 28 nm for ZIF-8/500 and ZIF-8/900 membranes, respectively. To better observe the growth and homogeneity of the ZIF-8 layer, the formation of the ZIF-8 layer is done on the porous PP support (**Figure 5.3**). A dense layer of ZIF-8 could not be formed due to the microporous nature of the PP support as the pore size of the PP ranges between 20 and 200 nm. As seen in Figure 5.3b, islands of ZIF-8 between 20 and 100 nm in size are formed and contour to the porous structure of the PP. The formation of islands is expected, as the growth of ZIF-8 should obey classic nucleation theory. The concentration of the precursors is at high enough concentrations such that multiple nucleation sites should occur.

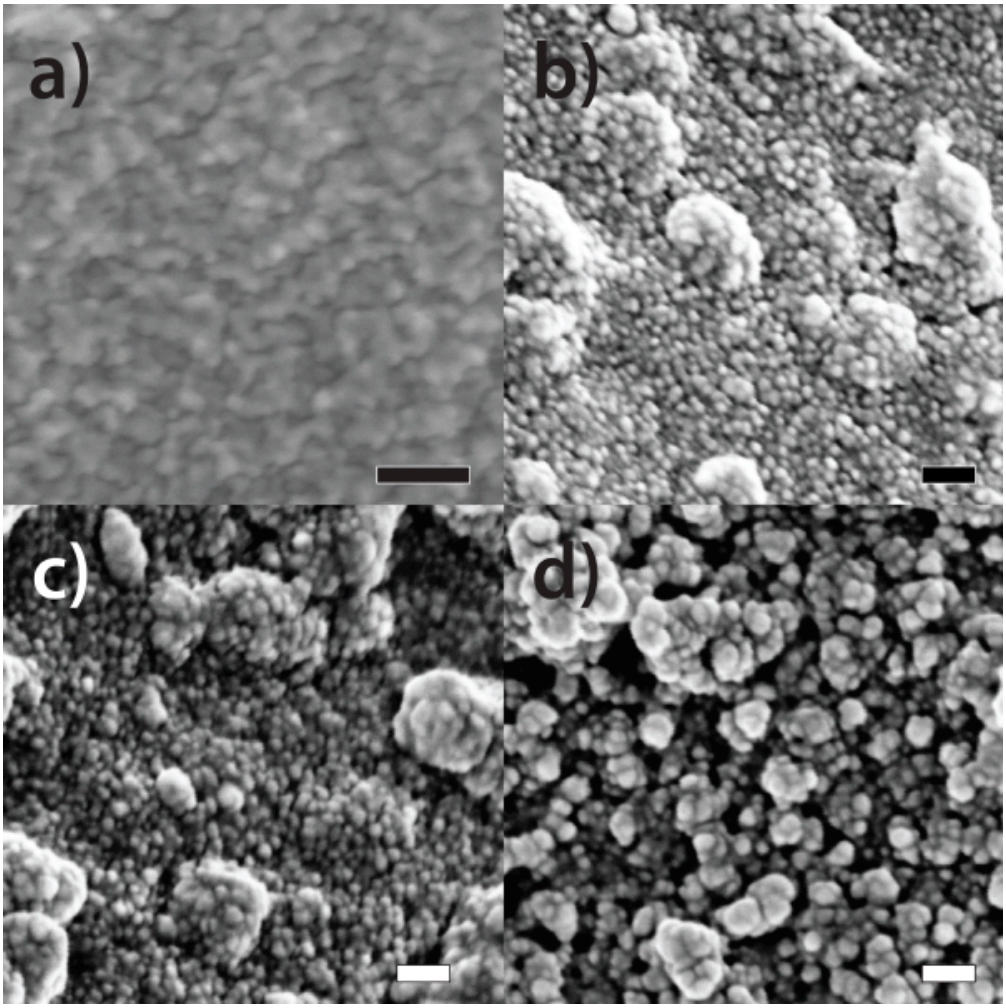

Figure 5.2. SEM images of membranes: a) PANI, b) ZIF-8/290, c) ZIF-8/500, and d) ZIF-8/900. A granular morphology is present in each membrane due to the polymerization and growth method of PANI and ZIF-8, respectively.

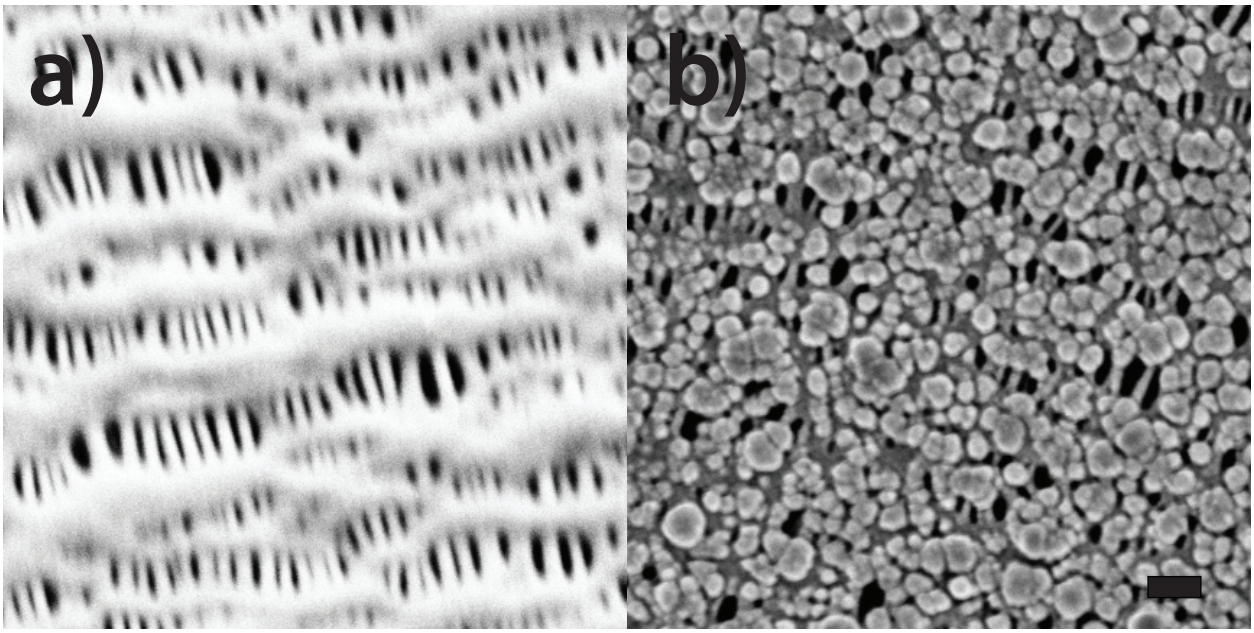

Figure 5.3. Top-down SEM images of a) Celgard polypropylene support and b) 30 cycle deposition of ZIF-8. The growth of ZIF-8 is island like and is concentrated on polymer regions of the porous support.

Table 5.1. Relative atomic compositions of the PP, PANI, and ZIF-8/500 films determined using XPS quantitative analysis after argon etching for 10 seconds.

	O 1S	N 1S	C 1S	Zn 2p3/2	C/N	C/Zn	N/Zn
PP	0	0	100	-	-	-	-
PANI	10.2	15.9	73.9	-	4.65	-	-
ZIF-8/500	10.7	14.6	67.1	7.6	4.60	8.82	1.92

XPS analysis is used to characterize the composition of the membrane at various fabrication steps and verify the presence of ZIF-8 at the membrane surface. The measurements are conducted over binding energy range between 180 and 1200 eV, which encompasses the Zn 2p, O 1S, N 1S, and C 1S regions. Hydrogen is excluded as it cannot be detected through XPS methods. **Table 5.1** presents the relative atomic percentages of Zn, O, N, and C for the bare PP support, 1-vinyl imidazole grafted PANI, and ZIF-8/500 films after 10 seconds of argon etching to clean the surface. As expected, only carbon is present in the bare PP support. Oxygen and nitrogen peaks arise in the 1-vinyl imidazole grafted PANI film at a relative concentration of 10.2% and 15.9%, respectively. The oxygen signal is observed due to surface adsorption of oxygen species with nitrogen groups found in PANI and 1-vinyl imidazole, as well as the presence of unreacted benzophenone. If oxygen concentration is excluded, the relative concentrations of nitrogen and carbon become to 17.7% and 82.3%, respectively, equivalent to a C/N ratio of 4.65. In comparison, the C/N for PANI and 1-vinyl imidazole are 6 and 2.5, respectively, and confirms that 1-vinyl imidazole is successfully grafted onto the PANI layer.

In ZIF-8/500 membranes, zinc is detected and quantified by its 2p 3/2 photoelectron peak. The relative concentrations for O, N, C, and Zn are 10.2%, 14.6%, 67.1% and 7.6%, respectively. The C/Zn and N/Zn ratios are 8.82 and 1.92, respectively. The expected relative composition of ZIF-8 is 30.8%, 61.5%, and 7.7% for N, C, and Zn, respectively, which is equivalent to a C/Zn of 8 and an N/Zn of 4. These results suggest that the ZIF-8 layer may be deficient in Zn. However, as XPS is surface sensitive technique, the composition at the surface would be skewed towards which layer is last deposited following the LBL growth method. Here, 2-methyl imidazole is the final layer deposited and results in the higher than expected concentration of nitrogen species relative to zinc.. The presence of oxygen and higher than expected carbon species, with respect to, nitrogen (C/N of 4.6) can arise from a number of reasons. Undercoordinated Zn atoms within the framework can coordinate with water and carbon dioxide molecules to form hydroxyl and carbonate species, resulting in the appearance of oxygen species and higher carbon concentrations in XPS.[179] Excess carbon species can also arise due to the presence of adventitious carbon, as the samples are prepared under atmospheric conditions. Nonetheless, the atomic quantification of the ZIF-8/500 membranes from XPS suggests that ZIF-8 is successfully synthesized as a thin layer.

Pure gas CO2 and CH4 permeance is measured using a constant volume/variable pressure Permeance values and CO2/CH4 selectivity is presented in Figure 5.4 as a function of ZIF-8 thickness and CO2 pressure. CO2 permeance initially increases from 24.8 in PANI only membranes to 28.2 GPU when the thickness of ZIF-8 reaches 290 nm (ZIF-8/290) as seen in Figure 5.4a at a pressure of 2 bar. The increase in permeance is attributed to the addition of the porous ZIF-8. The porous nature of ZIF-8 allows molecular species to diffuse faster at the PANI interface than if [C6mim][T2fn] is used solely. As the ZIF-8 thickness increases from 290 nm to 500 (ZIF-8/500) and 900 nm (ZIF-8/900), CO2 permeance decreases to 13.9 and 15 GPU, respectively. However, in parallel, CO2 selectivity over CH4 undergoes a rapid jump when the ZIF-8 thickness increases from 290 nm to 900 nm. CO2/CH4 selectivity is initially 12.5 for PANI only membranes and remains the same when ZIF-8 is deposited to a thickness of 290 nm. Further increases in the ZIF-8 thickness to 500 and 900 nm results in the selectivity rapidly increasing to 16.6 and 25.1, respectively. I speculate that the dramatic decrease in permeance from a ZIF-8 layer of 290 nm to 500 nm is due to a thicker ZIF-8 layer and grain boundaries in this layer. Mismatch of the porous structure can lead to dead-end pathways of molecular diffusion across the membrane. This postulation is partially confirmed through the increase in selectivity. There are more opportunities for grain boundary mismatch as the thickness increases. Thus, I would expect selectivity to increase as the ZIF-8 layer thickness increases.

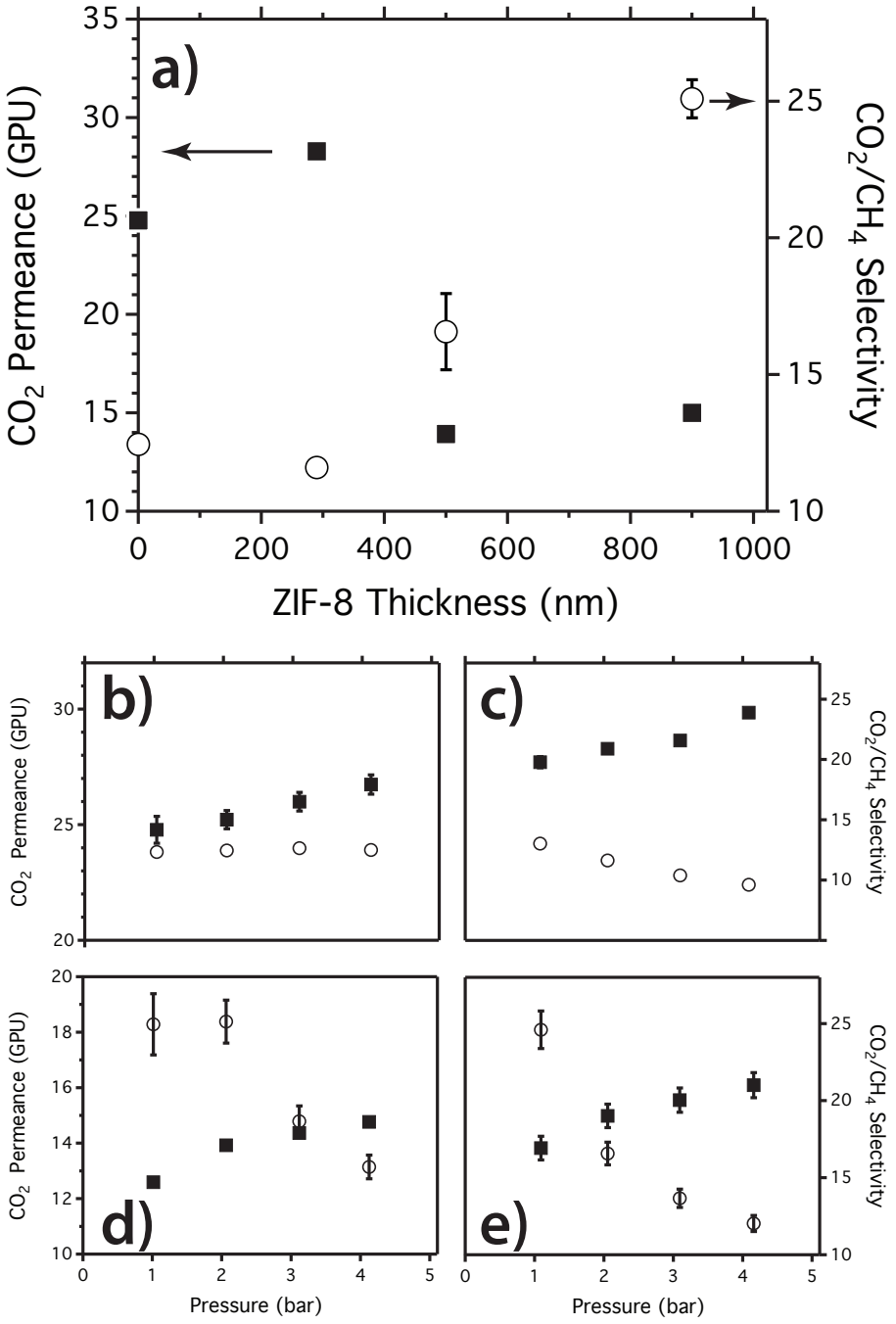

Figure 5.4. a) CO_2 permeance and CO_2/CH_4 selectivity of ZIF-8 membranes as a function of ZIF-8 thickness. Pressure dependent CO_2 permeance and CO_2/CH_4 selectivity for b) PANI, c) ZIF-8/290, d) ZIF-8/500, and e) ZIF-8/900. 1 GPU = $3.34*10^{-10}$ mol $m^{-2}s^{-1}$ Pa^{-1}.

Figure 5.4b-e present pressure dependent CO_2 permeance and CO_2/CH_4 selectivities of the PANI and ZIF-8 membranes. In all membranes, CO_2 permeance increases as pressure increases from one bar to five bars. A similar trend is observed for the pressure dependence of CO_2 permeance to ZIF-8 thickness where the behavior of PANI only and ZIF-

8/290 membranes differ from the ZIF-8/500 and ZIF-8/900 membranes. PANI only and ZIF-8/290 membranes exhibit CO_2 permeance increases of only 7.7% and 9.2%, respectively, from 24.8 and 27.7 to 26.7 and 29.9 as CO_2 feed pressure increases from one to five bar. A significantly higher increase in permeance is observed in ZIF-8/500 and ZIF-8/900 membranes. In these membranes, the CO_2 permeance increases 17% and 16%, respectively, from 12.6 and 13.8 to 14.8 and 16.1 GPU. The highest CO_2/CH_4 selectivities are observed at one bar for ZIF-8/500 and ZIF-8/900 membranes with values reaching as high as 24.9 and 24.6 respectively. This selectivity is over 200% higher than the PANI membrane (12.3) and 300-400% higher than previously reported ZIF-8 membranes. The tremendous increase in CO_2/CH_4 selectivity is attributed to the presence of [C6mim][T2fn] RTIL. [C6mim][T2fn] improves selectivity on two fronts. First, the RTIL can plug non-selective defects present within the ZIF-8 membranes. Second, the fluid nature and CO_2 selective properties of the RTIL enable a highly selective facilitated transport mechanism in parallel with the molecular sieving capabilities of ZIF-8.

5.4 Conclusions

In summary, I demonstrate the method to fabricate CO_2-selective flexible MOF membranes solvated by a RTIL utilizing the layer-by-layer growth method. The separation properties of the membrane depend on both the thickness of the MOF layer and the CO_2 feed gas pressure. The process described here to prepare membranes can be widely applied to many other classes of MOFs given the diversity of organic linker molecules. Further, the flexibility of these membranes will enable significant design freedom and conformity to current polymer-based membrane modules.

5.5 Acknowledgements

I would like to thank N. Blinova and F. Svec for their contributions and scientific discussions. Work at the Molecular Foundry and the Advanced Light Source was supported by the Office of Science, Office of Basic Energy Sciences, of the U.S. Department of Energy under Contract No. DE-ACO2-05CH11231. N. Su was supported by the Department of Defense (DoD) through the National Defense Science & Engineering Graduate Fellowship Program. N.S. was supported by the Department of Defense (DoD) through the National Defense Science & Engineering Graduate Fellowship Program.

5.6 Supporting Information

Supporting information for this chapter can be found in Appendix A.4

Chapter 6. Conclusions and Outlook

The unfettered rise in global carbon emissions has led to increasing efforts to advance technologies and policies to curtail consumption of fossil-based fuel sources. While many strategies exist, the most immediate and deployable effort lies within carbon capture and storage. In this sector, hybrid membranes are the most promising carbon capture technology, and membranes as a class offer significant higher energy efficiencies than incumbent solvent exchange and adsorbent processes. Hybrid membranes combine the solution processability of polymers with the enhanced selectivity of inorganic materials to craft a high-performing membrane, which can also benefit from synergistic enhancements due to interphase interactions. However, the success of hybrid membranes greatly depends on understanding fundamental transport effects from the inorganic phase and ensuring proper interfacial contact and adhesion. This dissertation has focused on exploring effects of inorganic size and surface chemistry on fundamental molecular transport properties to designing high performing dual-transport membranes to applying insight gained from hybrid membranes to craft the next generation MOF membranes.

In Chapter 2, I show that the size of silica nanoparticles leads to significant transport deviations not captured by effective medium models. The total available interfacial area is found to primarily contribute to the observed deviations. As the nanoparticle size decreases, total interfacial area increases and leads to simultaneous increase in polymer rigidity and increase in polymer chain packing. In Chapter 3, following the model system devised in Chapter 2, I exploit the interfacial area through silica surface functionalization with amine groups to characteristically alter the hydrogen-bonding environment at the interface. This leads to a fundamental shift to transport performance exceeding the pure polymers, indicative of a synergistic enhancement, in addition to improvements in mechanical and thermal stability of the membranes. In Chapter 4, the insights learned from the model system are applied to a new material system containing UiO-66-NH_2 MOF. Through pushing the boundaries of previously achievable MOF loadings, I show the possibility to form dual transport pathways. The availability of a secondary pathway through the MOF enables significantly enhanced permeation without sacrificing selectivity. Finally, in Chapter 5, I demonstrate the possibility to form a selective MOF layer on a flexible polymer support enabling a new paradigm in next generation membranes.

The findings presented in this dissertation provide a clearer view of fundamental shifts in molecular transport properties due to changes of the inorganic material and design opportunities for performance enhancement in hybrid membranes. Further coupling and integration of the inorganic with the polymer through functionalization of the inorganic surface will lead to fewer defects and more selective membranes. Extending the notion of dual transport pathways to more CO_2 permeable polymers and size selective MOFs are promising opportunities to design membranes competitive with incumbent technologies.

Chapter 7. References

(1) Barden, J. L.; Mellish, M. L.; Murphy, B. T.; Slater-thompson, N.; Peterson, D.; Lindstrom, P. International Energy Outlook 2013. *EIA* **2013**.

(2) Historic Paris Agreement on Climate Change- 195 Nations Set Path to Keep Temperature Rise Well Below 2 Degrees Celsius http://newsroom.unfccc.int/unfccc-newsroom/finale-cop21/ (accessed Mar 1, 2016).

(3) Program, U. S. G. C. R. Global Climate Change. **2009**, 13–26.

(4) IEA. Energy and Climate Change. *World Energy Outlook Spec. Rep.* **2015**, 1–200.

(5) NOAA. Weekly average CO2 at Mauna Loa ESRL Global Monitoring Division http://www.esrl.noaa.gov/gmd/ccgg/trends/weekly.html (accessed Mar 1, 2016).

(6) Socolow, R. H.; Pacala, S. W. A Plan to Keep Carbon in Check. *Sci. Am.* **2006**, *295*, 50–57.

(7) Pacala, S.; Socolow, R. Stabilization Wedges: Solving the Climate Problem for the next 50 Years with Current Technologies. *Science* **2004**, *305*, 968–972.

(8) *DOE/NETL Advanced Carbon Dioxide Capture R&D Program: Technology Update*; U.S. Government Printing Office: Washington, DC, 2013.

(9) U.S. Department of Energy. Materials for Separation Technologies : Energy and Emission Reduction Opportunities. **2005**.

(10) Fu, X.; Zhao, N.; Li, J.; Xiao, F.; Wei, W.; Sun, Y.; Key, S. Carbon Dioxide Capture by MgO-Modified MCM-41 Materials. **2009**, 593–602.

(11) Belmabkhout, Y.; Serna-guerrero, R.; Sayari, A. MCM-41 Silica : Application for Gas Purification. **2010**, 359–365.

(12) Belmabkhout, Y.; Sayari, A. Effect of Pore Expansion and Amine Functionalization of Mesoporous Silica on CO2 Adsorption over a Wide Range of Conditions. *Adsorption* **2009**, *15*, 318–328.

(13) Horiuchi, T.; Hidaka, H.; Fukui, T.; Kubo, Y.; Horio, M.; Suzuki, K.; Mori, T. Effect of Added Basic Metal Oxides on CO2 Adsorption on Alumina at Elevated Temperatures. *Appl. Catal. A Gen.* **1998**, *167*, 195–202.

(14) Siriwardane, R. V.; Shen, M.-S.; Fisher, E. P.; Poston, J. A. Adsorption of CO 2 on Molecular Sieves and Activated Carbon. *Energy & Fuels* **2001**, *15*, 279–284.

(15) Caro, J.; Noack, M.; Kölsch, P.; Schäfer, R. Zeolite Membranes – State of Their Development and Perspective. *Microporous Mesoporous Mater.* **2000**, *38*, 3–24.

(16) Samanta, A.; Zhao, A.; Shimizu, G. K. H.; Sarkar, P.; Gupta, R. Post-Combustion CO2 Capture Using Solid Sorbents: A Review. *Ind. Eng. Chem. Res.* **2012**, *51*, 1438–1463.

(17) Cmarik, G. E.; Kim, M.; Cohen, S. M.; Walton, K. S. Tuning the Adsorption Properties of UiO-66 via Ligand Functionalization. *Langmuir* **2012**, *28*, 15606–15613.

(18) Bux, H.; Chmelik, C.; Van Baten, J. M.; Krishna, R.; Caro, J. Novel MOF-Membrane for Molecular Sieving Predicted by IR-Diffusion Studies and Molecular Modeling. *Adv. Mater.* **2010**, *22*, 4741–4743.

(19) Britt, D.; Furukawa, H.; Wang, B.; Glover, T. G.; Yaghi, O. M. Highly Efficient Separation of Carbon Dioxide by a Metal-Organic Framework Replete with Open Metal Sites. *Proc. Natl. Acad. Sci. U. S. A.* **2009**, *106*, 20637–20640.

(20) McDonald, T. M.; Mason, J. a.; Kong, X.; Bloch, E. D.; Gygi, D.; Dani, A.; Crocellà, V.; Giordanino, F.; Odoh, S. O.; Drisdell, W. S.; *et al.* Cooperative Insertion of CO2 in Diamine-Appended Metal-Organic Frameworks. *Nature* **2015**.

(21) Baker, R. W. Future Directions of Membrane Gas Separation Technology. *Ind. Eng. Chem. Res.* **2002**, *41*, 1393–1411.

(22) Alivisatos, A. P.; Buchanan, M. *DOE Report: Basic Research Needs for Carbon Capture: Beyond 2020*; 2010.

(23) Matteucci, S.; Yampolskii, Y.; Freeman, B. D.; Pinnau, I. *Materials Science of Membranes for Gas and Vapor Separation*; Yampolskii, Y.; Pinnau, I.; Freeman, B., Eds.; John Wiley & Sons, Ltd: Chichester, UK, 2006.

(24) Koros, W. J.; Fleming, G. K. Membrane-Based Gas Separation. **1993**, *83*.

(25) D'Alessandro, D. M.; Smit, B.; Long, J. R. Carbon Dioxide Capture: Prospects for New Materials. *Angew. Chem. Int. Ed. Engl.* **2010**, *49*, 6058–6082.

(26) Graham, T. On the Absorption and Dialytic Separation of Gases by Colloid Septa. **1866**, *32*, 401–420.

(27) Gray-Weale, A. A.; Henchman, R. H.; Gilbert, R. G.; Greenfield, M. L.; Theodorou, D. N. Transition-State Theory Model for the Diffusion Coefficients of Small Penetrants in Glassy Polymers. *Macromolecules* **1997**, *30*, 7296–7306.

(28) Robeson, L. M. The Upper Bound Revisited. *J. Memb. Sci.* **2008**, *320*, 390–400.

(29) Robeson, L. M. Correlation of Separation Factor versus Permeability for Polymeric

Membranes. *J. Memb. Sci.* **1991**, *62*, 165–185.

(30) Freeman, B. D. Basis of Permeability/Selectivity Tradeoff Relations in Polymeric Gas Separation Membranes. *Macromolecules* **1999**, *32*, 375–380.

(31) Guiver, M. D.; Lee, Y. M. Polymer Rigidity Improves Microporous Membranes. *Science* **2013**, *339*, 284–285.

(32) Carta, M.; Malpass-Evans, R.; Croad, M.; Rogan, Y.; Jansen, J. C.; Bernardo, P.; Bazzarelli, F.; McKeown, N. B. An Efficient Polymer Molecular Sieve for Membrane Gas Separations. *Science* **2013**, *339*, 303–307.

(33) Park, H. B.; Jung, C. H.; Lee, Y. M.; Hill, A. J.; Pas, S. J.; Mudie, S. T.; Van Wagner, E.; Freeman, B. D.; Cookson, D. J. Polymers with Cavities Tuned for Fast Selective Transport of Small Molecules and Ions. *Science* **2007**, *318*, 254–258.

(34) Sanders, D. F.; Smith, Z. P.; Ribeiro, C. P.; Guo, R.; McGrath, J. E.; Paul, D. R.; Freeman, B. D. Gas Permeability, Diffusivity, and Free Volume of Thermally Rearranged Polymers Based on 3,3′-Dihydroxy-4,4′-Diamino-Biphenyl (HAB) and 2,2′-Bis-(3,4-Dicarboxyphenyl) Hexafluoropropane Dianhydride (6FDA). *J. Memb. Sci.* **2012**, *409-410*, 232–241.

(35) Park, H. B.; Han, S. H.; Jung, C. H.; Lee, Y. M.; Hill, A. J. Thermally Rearranged (TR) Polymer Membranes for CO2 Separation. *J. Memb. Sci.* **2010**, *359*, 11–24.

(36) Smith, Z. P.; Hern??ndez, G.; Gleason, K. L.; Anand, A.; Doherty, C. M.; Konstas, K.; Alvarez, C.; Hill, A. J.; Lozano, A. E.; Paul, D. R.; *et al.* Effect of Polymer Structure on Gas Transport Properties of Selected Aromatic Polyimides, Polyamides and TR Polymers. *J. Memb. Sci.* **2015**, *493*, 766–781.

(37) Ghosal, K.; Chern, R. T.; Freeman, B. D.; Daly, W. H.; Negulescu, I. I. Effect of Basic Substituents on Gas Sorption and Permeation in Polysulfone. *Macromolecules* **1996**, *29*, 4360–4369.

(38) Puleo, A. C.; Paul, D. R.; Kelley, S. S. The Effect of Degree of Acetylation on Gas Sorption and Transport Behavior in Cellulose Acetate. *J. Memb. Sci.* **1989**, *47*, 301–332.

(39) Vu, D. Q.; Koros, W. J.; Miller, S. J. Mixed Matrix Membranes Using Carbon Molecular Sieves- I. Preparation and Experimental Results. *J. Memb. Sci.* **2003**, *211*, 335–348.

(40) Cong, H.; Radosz, M.; Towler, B.; Shen, Y. Polymer–inorganic Nanocomposite Membranes for Gas Separation. *Sep. Purif. Technol.* **2007**, *55*, 281–291.

(41) Cho, E. S.; Coates, N. E.; Forster, J. D.; Ruminski, A. M.; Russ, B.; Sahu, A.; Su, N. C.; Yang, F.; Urban, J. J. Engineering Synergy: Energy and Mass Transport in Hybrid

Nanomaterials. *Adv. Mater.* **2015**, *27*, 5744–5752.

(42) Noble, R. D. Perspectives on Mixed Matrix Membranes. *J. Memb. Sci.* **2011**, *378*, 393–397.

(43) Zornoza, B.; Tellez, C.; Coronas, J.; Gascon, J.; Kapteijn, F. Metal Organic Framework Based Mixed Matrix Membranes: An Increasingly Important Field of Research with a Large Application Potential. *Microporous Mesoporous Mater.* **2013**, *166*, 67–78.

(44) Kim, S.; Marand, E.; Ida, J.; Guliants, V. V. Polysulfone and Mesoporous Molecular Sieve MCM-48 Mixed Matrix Membranes for Gas Separation. *Chem. Mater.* **2006**, *18*, 1149–1155.

(45) Waqas Anjum, M.; Bueken, B.; De Vos, D.; Vankelecom, I. F. J. MIL-125(Ti) Based Mixed Matrix Membranes for CO2 Separation from CH4 and N2. *J. Memb. Sci.* **2016**, *502*, 21–28.

(46) Dong, G.; Li, H.; Chen, V. Challenges and Opportunities for Mixed-Matrix Membranes for Gas Separation. *J. Mater. Chem. A* **2013**, *1*, 4610.

(47) Husain, S.; Koros, W. J. A General Strategy for Adhesion Enhancement in Polymeric Composites by Formation of Nanostructured Particle Surfaces. *J. Phys. Chem. C* **2007**, *111*, 652–657.

(48) Schadler, L. S.; Kumar, S. K.; Benicewicz, B. C.; Lewis, S. L.; Harton, S. E. Designed Interfaces in Polymer Nanocomposites: A Fundamental Viewpoint. *MRS Bull.* **2011**, *32*, 335–340.

(49) Zimmerman, C. M.; Singh, A.; Koros, W. J. Tailoring Mixed Matrix Composite Membranes for Gas Separations. *J. Memb. Sci.* **1997**, *137*, 145–154.

(50) Singh, A.; Koros, W. J. Significance of Entropic Selectivity for Advanced Gas Separation Membranes. *Ind. Eng. Chem. Res.* **1996**, *35*, 1231–1234.

(51) Merkel, T. C.; Freeman, B. D.; Spontak, R. J.; He, Z.; Pinnau, I.; Meakin, P.; Hill, A. J. Ultrapermeable, Reverse-Selective Nanocomposite Membranes. *Science* **2002**, *296*, 519–522.

(52) Jancar, J.; Douglas, J. F.; Starr, F. W.; Kumar, S. K.; Cassagnau, P.; Lesser, a. J.; Sternstein, S. S.; Buehler, M. J. Current Issues in Research on Structure–property Relationships in Polymer Nanocomposites. *Polymer (Guildf).* **2010**, *51*, 3321–3343.

(53) Merkel, T. C.; Freeman, B. D.; Spontak, R. J.; He, Z.; Pinnau, I.; Meakin, P.; Hill, A. J. Sorption, Transport, and Structural Evidence for Enhanced Free Volume in Poly(4-Methyl-2-pentyne)/Fumed Silica Nanocomposite Membranes. *Chem. Mater.* **2003**, *15*, 109–123.

(54) Ahn, J.; Chung, W.-J.; Pinnau, I.; Song, J.; Du, N.; Robertson, G. P.; Guiver, M. D. Gas Transport Behavior of Mixed-Matrix Membranes Composed of Silica Nanoparticles in a Polymer of Intrinsic Microporosity (PIM-1). *J. Memb. Sci.* **2010**, *346*, 280–287.

(55) Suzuki, T.; Yamada, Y. Physical and Gas Transport Properties of Novel Hyperbranched Polyimide - Silica Hybrid Membranes. *Polym. Bull.* **2004**, *53*, 139–146.

(56) Takahashi, S.; Paul, D. R. Gas Permeation in Poly(ether Imide) Nanocomposite Membranes Based on Surface-Treated Silica. Part 2: With Chemical Coupling to Matrix. *Polymer (Guildf).* **2006**, *47*, 7535–7547.

(57) Kim, H.; Kim, H.-G.; Kim, S.; Kim, S. S. PDMS–silica Composite Membranes with Silane Coupling for Propylene Separation. *J. Memb. Sci.* **2009**, *344*, 211–218.

(58) Matteucci, S.; Kusuma, V. A.; Swinnea, S.; Freeman, B. D. Gas Permeability, Solubility and Diffusivity in 1,2-Polybutadiene Containing Brookite Nanoparticles. *Polymer (Guildf).* **2008**, *49*, 757–773.

(59) Noble, R. D. Facilitated Transport Membranes Mechanism in Fixed Site Carrier. **1991**, *60*, 297–306.

(60) Merkel, T. C.; Blanc, R.; Ciobanu, I.; Firat, B.; Suwarlim, A.; Zeid, J. Silver Salt Facilitated Transport Membranes for Olefin/paraffin Separations: Carrier Instability and a Novel Regeneration Method. *J. Memb. Sci.* **2013**, *447*, 177–189.

(61) Shinohara, H.; Shibata, H.; Wohrle, D.; Nishide, H. Reversible Oxygen Binding to the Polymeric Cobalt Tetraazaporphyrin Complex and Oxygen-Facilitated Transport through Its Membrane. *Macromol. Rapid Commun.* **2005**, *26*, 467–470.

(62) Hosseini, S.; Li, Y.; Chung, T.; Liu, Y. Enhanced Gas Separation Performance of Nanocomposite Membranes Using MgO Nanoparticles. *J. Memb. Sci.* **2007**, *302*, 207–217.

(63) Bhaduri, G. a.; Šiller, L. Nickel Nanoparticles Catalyse Reversible Hydration of Carbon Dioxide for Mineralization Carbon Capture and Storage. *Catal. Sci. Technol.* **2013**, *3*, 1234.

(64) Kang, S. W.; Char, K.; Kang, Y. S. Novel Application of Partially Positively Charged Silver Nanoparticles for Facilitated Transport in Olefin/Paraffin Separation Membranes. *Chem. Mater.* **2008**, *20*, 1308–1311.

(65) Kang, Y. S.; Kang, S. W.; Kim, H.; Kim, J. H.; Won, J.; Kim, C. K.; Char, K. Interaction with Olefins of the Partially Polarized Surface of Silver Nanoparticles Activated by P-Benzoquinone and Its Implications for Facilitated Olefin Transport. *Adv. Mater.* **2007**, *19*, 475–479.

(66) Vu, D. Q.; Koros, W. J.; Miller, S. J. Mixed Matrix Membranes Using Carbon Molecular Sieves - II. Modeling Permeation Behavior. *J. Memb. Sci.* **2003**, *211*, 311–334.

(67) Reid, B. D.; Ruiz-Trevino, F. A.; Musselman, I. H.; Balkus, K. J.; Ferraris, J. P. Gas Permeability Properties of Polysulfone Membranes Containing the Mesoporous Molecular Sieve MCM-41. *Chem. Mater.* **2001**, *13*, 2366–2373.

(68) Kim, S.; Marand, E. High Permeability Nano-Composite Membranes Based on Mesoporous MCM-41 Nanoparticles in a Polysulfone Matrix. *Microporous Mesoporous Mater.* **2008**, *114*, 129–136.

(69) Wu, H.; Li, X.; Li, Y.; Wang, S.; Guo, R.; Jiang, Z.; Wu, C.; Xin, Q.; Lu, X. Facilitated Transport Mixed Matrix Membranes Incorporated with Amine Functionalized MCM-41 for Enhanced Gas Separation Properties. *J. Memb. Sci.* **2014**, *465*, 78–90.

(70) Bastani, D.; Esmaeili, N.; Asadollahi, M. Polymeric Mixed Matrix Membranes Containing Zeolites as a Filler for Gas Separation Applications: A Review. *J. Ind. Eng. Chem.* **2013**, *19*, 375–393.

(71) Li, Y.; Guan, H.-M.; Chung, T.-S.; Kulprathipanja, S. Effects of Novel Silane Modification of Zeolite Surface on Polymer Chain Rigidification and Partial Pore Blockage in Polyethersulfone (PES)–zeolite A Mixed Matrix Membranes. *J. Memb. Sci.* **2006**, *275*, 17–28.

(72) Yilmaz, G.; Keskin, S. Molecular Modeling of MOF and ZIF-Filled MMMs for CO2/N2 Separations. *J. Memb. Sci.* **2013**, *454*, 407–417.

(73) Hu, Z.; Kang, Z.; Qian, Y.; Peng, Y.; Wang, X.; Chi, C.; Zhao, D. Mixed Matrix Membranes Containing UiO-66(Hf)-(OH) $_2$ Metal–Organic Framework Nanoparticles for Efficient H $_2$ /CO $_2$ Separation. *Ind. Eng. Chem. Res.* **2016**, *66*, acs.iecr.5b04568.

(74) Anjum, M. W.; Vermoortele, F.; Khan, A. L.; Bueken, B.; De Vos, D. E.; Vankelecom, I. F. J. Modulated UiO-66-Based Mixed-Matrix Membranes for CO2 Separation. *ACS Appl. Mater. Interfaces* **2015**, *7*, 25193–25201.

(75) Bae, T.-H.; Long, J. R. CO2/N2 Separations with Mixed-Matrix Membranes Containing Mg2(dobdc) Nanocrystals. *Energy Environ. Sci.* **2013**, *6*, 3565–3569.

(76) Long, J. R.; Yaghi, O. M. The Pervasive Chemistry of Metal-Organic Frameworks. *Chem. Soc. Rev.* **2009**, *38*, 1213–1214.

(77) Bouma, R. H. B.; Checchetti, A.; Chidichimo, G.; Drioli, E. Permeation through a Heterogeneous Membrane: The Effect of the Dispersed Phase. *J. Memb. Sci.* **1997**, *128*, 141–149.

(78) Vinh-Thang, H.; Kaliaguine, S. Predictive Models for Mixed-Matrix Membrane Performance: A Review. *Chem. Rev.* **2013**, *113*, 4980–5028.

(79) Ash, B. J.; Siegel, R. W.; Schadler, L. S. Glass-Transition Temperature Behavior of alumina/PMMA Nanocomposites. *J. Polym. Sci. Part B Polym. Phys.* **2004**, *42*, 4371–4383.

(80) Bansal, A.; Yang, H.; Li, C.; Cho, K.; Benicewicz, B. C.; Kumar, S. K.; Schadler, L. S. Quantitative Equivalence between Polymer Nanocomposites and Thin Polymer Films. *Nat. Mater.* **2005**, *4*, 693–698.

(81) Zhang, C.; Priestley, R. D. Fragility and Glass Transition Temperature of Polymer Confined under Isobaric and Isochoric Conditions. *Soft Matter* **2013**, *9*, 7076–7085.

(82) Evans, C. M.; Deng, H.; Jager, W. F.; Torkelson, J. M. Fragility Is a Key Parameter in Determining the Magnitude of T G -Confinement Effects in Polymer Films. *Macromolecules* **2013**, *46*, 6091–6103.

(83) Qin, Q.; McKenna, G. B. Correlation between Dynamic Fragility and Glass Transition Temperature for Different Classes of Glass Forming Liquids. *J. Non. Cryst. Solids* **2006**, *352*, 2977–2985.

(84) Huang, D.; McKenna, G. B. New Insights into the Fragility Dilemma in Liquids. *J. Chem. Phys.* **2001**, *114*, 5621.

(85) Ansaloni, L.; Zhao, Y.; Jung, B. T.; Ramasubramanian, K.; Baschetti, M. G.; Ho, W. S. W. Facilitated Transport Membranes Containing Amino-Functionalized Multi-Walled Carbon Nanotubes for High-Pressure CO2 Separations. *J. Memb. Sci.* **2015**, *490*, 18–28.

(86) Wu, H.; Li, X.; Li, Y.; Wang, S.; Guo, R.; Jiang, Z.; Wu, C.; Xin, Q.; Lu, X. Facilitated Transport Mixed Matrix Membranes Incorporated with Amine Functionalized MCM-41 for Enhanced Gas Separation Properties. *J. Memb. Sci.* **2014**, *465*, 78–90.

(87) Freeman, B. D. Basis of Permeability/Selectivity Tradeoff Relations in Polymeric Gas Separation Membranes. *Macromolecules* **1999**, *32*, 375–380.

(88) Choudalakis, G.; Gotsis, A. D. Permeability of Polymer/clay Nanocomposites: A Review. *Eur. Polym. J.* **2009**, *45*, 967–984.

(89) Matteucci, S.; Raharjo, R. D.; Kusuma, V. A.; Swinnea, S.; Freeman, B. D. Gas Permeability, Solubility, and Diffusion Coefficients in 1,2-Polybutadiene Containing Magnesium Oxide. *Macromolecules* **2008**, *41*, 2144–2156.

(90) Nishide, H.; Kawakami, H.; Sasame, Y.; Ishiwata, K.; Tsuchida*, E. Facilitated Transport of Molecular Oxygen in cobaltporphyrin/poly(1-Trimethylsilyl-1-

Propyne) Membrane. *J. Polym. Sci. Part A Polym. Chem.* **1992**, *30*, 77–82.

(91) Ploegmakers, J.; Japip, S.; Nijmeijer, K. Mixed Matrix Membranes Containing MOFs for Ethylene/ethane separation—Part B: Effect of Cu3BTC2 on Membrane Transport Properties. *J. Memb. Sci.* **2013**, *428*, 331–340.

(92) Stober, W. Controlled Growth of Monodisperse Silica Spheres in the Micron Size Range 1. *J. Colloid Interface Sci.* **1968**, *69*, 62–69.

(93) Bogush, G. H.; Tracy, M. A.; Zukoski, C. F. Preparation of Monodisperse Silica Particles: Control of Size and Mass Fraction. *J. Non. Cryst. Solids* **1988**, *104*, 95–106.

(94) Lin, H.; Kai, T.; Freeman, B. D.; Kalakkunnath, S.; Kalika, D. S. The Effect of Cross-Linking on Gas Permeability in Cross-Linked Poly(Ethylene Glycol Diacrylate). *Macromolecules* **2005**, *38*, 8381–8393.

(95) Van Blaaderen, A.; Kentgens, A. P. M. Particle Morphology and Chemical Microstructure of Colloidal Silica Spheres Made from Alkoxysilanes. *J. Non. Cryst. Solids* **1992**, *149*, 161–178.

(96) Lin, H.; Freeman, B. D. *Springer Handbook of Materials Measurement Methods*; Czichos, H.; Saito, T.; Smith, L., Eds.; Springer: Berlin, Heidelberg, 2006.

(97) Ahn, J.; Chung, W.-J.; Pinnau, I.; Guiver, M. D. Polysulfone/silica Nanoparticle Mixed-Matrix Membranes for Gas Separation. *J. Memb. Sci.* **2008**, *314*, 123–133.

(98) Rittigstein, P.; Priestley, R. D.; Broadbelt, L. J.; Torkelson, J. M. Model Polymer Nanocomposites Provide an Understanding of Confinement Effects in Real Nanocomposites. *Nat. Mater.* **2007**, *6*, 278–282.

(99) Ellison, C. J.; Torkelson, J. M. The Distribution of Glass-Transition Temperatures in Nanoscopically Confined Glass Formers. *Nat. Mater.* **2003**, *2*, 695–700.

(100) Holt, A. P.; Griffin, P. J.; Bocharova, V.; Agapov, A. L.; Imel, A. E.; Dadmun, M. D.; Sangoro, J. R.; Sokolov, A. P. Dynamics at the Polymer/Nanoparticle Interface in Poly(2-vinylpyridine)/Silica Nanocomposites. *Macromolecules* **2014**, *47*, 1837–1843.

(101) Van Helden, a. K.; Jansen, J. W.; Vrij, a. Preparation and Characterization of Spherical Monodisperse Silica Dispersions in Nonaqueous Solvents. *J. Colloid Interface Sci.* **1981**, *81*, 354–368.

(102) Joly, C.; Smaihi, M.; Porcar, L.; Noble, R. D. Polyimide−Silica Composite Materials: How Does Silica Influence Their Microstructure and Gas Permeation Properties? *Chem. Mater.* **1999**, *11*, 2331–2338.

(103) Takahashi, S.; Paul, D. R. Gas Permeation in Poly(ether Imide) Nanocomposite

Membranes Based on Surface-Treated Silica. Part 1: Without Chemical Coupling to Matrix. *Polymer (Guildf).* **2006**, *47*, 7519–7534.

(104) Cong, H.; Hu, X.; Radosz, M.; Shen, Y. Brominated Poly(2,6-Diphenyl-1,4-Phenylene Oxide) and Its Silica Nanocomposite Membranes for Gas Separation. *Ind. Eng. Chem. Res.* **2007**, *46*, 2567–2575.

(105) Patel, N. P.; Miller, A. C.; Spontak, R. J. Highly CO2-Permeable and -Selective Membranes Derived from Crosslinked Poly(ethylene Glycol) and Its Nanocomposites. *Adv. Funct. Mater.* **2004**, *14*, 699–707.

(106) Patel, N. P.; Miller, a. C.; Spontak, R. J. Highly CO2-Permeable and Selective Polymer Nanocomposite Membranes. *Adv. Mater.* **2003**, *15*, 729–733.

(107) Cho, E. S.; Evans, C. M.; Davidson, E. C.; Hoarfrost, M. L.; Modestino, M. a.; Segalman, R. a.; Urban, J. J. Enhanced Water Vapor Blocking in Transparent Hybrid Polymer–Nanocrystal Films. *ACS Macro Lett.* **2015**, *4*, 70–74.

(108) Bernardo, P.; Drioli, E.; Golemme, G. Membrane Gas Separation: A Review/State of the Art. *Ind. Eng. Chem. Res.* **2009**, *48*, 4638–4663.

(109) Su, N. C.; Smith, Z. P.; Freeman, B. D.; Urban, J. J. Size-Dependent Permeability Deviations from Maxwell's Model in Hybrid Cross-Linked Poly(ethylene glycol)/Silica Nanoparticle Membranes. *Chem. Mater.* **2015**, *27*, 2421–2429.

(110) Chen, X. Y.; Nik, O. G.; Rodrigue, D.; Kaliaguine, S. Mixed Matrix Membranes of Aminosilanes Grafted FAU/EMT Zeolite and Cross-Linked Polyimide for CO2/CH4 Separation. *Polymer (Guildf).* **2012**, *53*, 3269–3280.

(111) Rezaei, F.; Lively, R. P.; Labreche, Y.; Chen, G.; Fan, Y.; Koros, W. J.; Jones, C. W. Aminosilane-Grafted Polymer/silica Hollow Fiber Adsorbents for CO_2 Capture from Flue Gas. *ACS Appl. Mater. Interfaces* **2013**, *5*, 3921–3931.

(112) Xin, Q.; Wu, H.; Jiang, Z.; Li, Y.; Wang, S.; Li, Q.; Li, X.; Lu, X.; Cao, X.; Yang, J. SPEEK/amine-Functionalized TiO2 Submicrospheres Mixed Matrix Membranes for CO2 Separation. *J. Memb. Sci.* **2014**, *467*, 23–35.

(113) Guo, X.; Huang, H.; Ban, Y.; Yang, Q.; Xiao, Y.; Li, Y.; Yang, W.; Zhong, C. Mixed Matrix Membranes Incorporated with Amine-Functionalized Titanium-Based Metal-Organic Framework for CO2/CH4 Separation. *J. Memb. Sci.* **2015**, *478*, 130–139.

(114) Xin, Q.; Gao, Y.; Wu, X.; Li, C.; Liu, T.; Shi, Y.; Li, Y.; Jiang, Z.; Wu, H.; Cao, X. Incorporating One-Dimensional Aminated Titania Nanotubes into Sulfonated Poly(ether Ether Ketone) Membrane to Construct CO2-Facilitated Transport Pathways for Enhanced CO2 Separation. *J. Memb. Sci.* **2015**, *488*, 13–29.

(115) Acres, R. G.; Ellis, A. V.; Alvino, J.; Lenahan, C. E.; Khodakov, D. a.; Metha, G. F.; Andersson, G. G. Molecular Structure of 3-Aminopropyltriethoxysilane Layers Formed on Silanol-Terminated Silicon Surfaces. *J. Phys. Chem. C* **2012**, *116*, 6289–6297.

(116) Zelenak, V.; Halamova, D.; Gaberova, L.; Bloch, E.; Llewellyn, P. Amine-Modified SBA-12 Mesoporous Silica for Carbon Dioxide Capture: Effect of Amine Basicity on Sorption Properties. *Microporous Mesoporous Mater.* **2008**, *116*, 358–364.

(117) Friedman, M. Applications of the Ninhydrin Reaction for Analysis of Amino Acids, Peptides, and Proteins to Agricultural and Biomedical Sciences. *J. Agric. Food Chem.* **2004**, *52*, 385–406.

(118) Baker, R. W.; Low, B. T. Gas Separation Membrane Materials: A Perspective. *Macromolecules* **2014**, *47*, 6999–7013.

(119) Ordoñez, M. J. C.; Balkus, K. J.; Ferraris, J. P.; Musselman, I. H. Molecular Sieving Realized with ZIF-8/Matrimid® Mixed-Matrix Membranes. *J. Memb. Sci.* **2010**, *361*, 28–37.

(120) Venna, S. R.; Lartey, M.; Li, T.; Spore, A.; Kumar, S.; Nulwala, H. B.; Luebke, D. R.; Rosi, N. L.; Albenze, E. Fabrication of MMMs with Improved Gas Separation Properties Using Externally-Functionalized MOF Particles. *J. Mater. Chem. A* **2015**, *3*, 5014–5022.

(121) Rodenas, T.; Luz, I.; Prieto, G.; Seoane, B.; Miro, H.; Corma, A.; Kapteijn, F.; Llabrés, F. X.; Gascon, J.; Llabrés i Xamena, F. X.; *et al.* Metal–organic Framework Nanosheets in Polymer Composite Materials for Gas Separation. *Nat. Mater.* **2014**, *14*, 48–55.

(122) Smith, S. J. D.; Ladewig, B. P.; Hill, A. J.; Lau, C. H.; Hill, M. R. Post-Synthetic Ti Exchanged UiO-66 Metal-Organic Frameworks That Deliver Exceptional Gas Permeability in Mixed Matrix Membranes. *Sci. Rep.* **2015**, *5*, 7823.

(123) Song, Q.; Nataraj, S. K.; Roussenova, M. V.; Tan, J. C.; Hughes, D. J.; Li, W.; Bourgoin, P.; Alam, M. A.; Cheetham, A. K.; Al-Muhtaseb, S. A.; *et al.* Zeolitic Imidazolate Framework (ZIF-8) Based Polymer Nanocomposite Membranes for Gas Separation. *Energy Environ. Sci.* **2012**, *5*, 8359–8369.

(124) Kang, Z.; Xue, M.; Fan, L.; Huang, L.; Guo, L.; Wei, G.; Chen, B.; Qiu, S. Highly Selective Sieving of Small Gas Molecules by Using an Ultra-Microporous Metal–organic Framework Membrane. *Energy Environ. Sci.* **2014**, *7*, 4053–4060.

(125) Zhang, C.; Dai, Y.; Johnson, J. R.; Karvan, O.; Koros, W. J. High Performance ZIF-8/6FDA-DAM Mixed Matrix Membrane for Propylene/propane Separations. *J. Memb. Sci.* **2012**, *389*, 34–42.

(126) Mahajan, R.; Koros, W. J. Mixed Matrix Membrane Materials with Glassy Polymers. Part 1. *Polym. Eng. Sci.* **2002**, *42*, 1420–1431.

(127) Chung, T.-S.; Jiang, L. Y.; Li, Y.; Kulprathipanja, S. Mixed Matrix Membranes (MMMs) Comprising Organic Polymers with Dispersed Inorganic Fillers for Gas Separation. *Prog. Polym. Sci.* **2007**, *32*, 483–507.

(128) Venna, S. R.; Carreon, M. a. Amino-Functionalized SAPO-34 Membranes for CO2/CH4 and CO2/N2 Separation. *Langmuir* **2011**, *27*, 2888–2894.

(129) Ban, Y.; Li, Y.; Peng, Y.; Jin, H.; Jiao, W.; Liu, X.; Yang, W. Metal-Substituted Zeolitic Imidazolate Framework ZIF-108: Gas-Sorption and Membrane-Separation Properties. *Chem. - A Eur. J.* **2014**, *20*, 1–9.

(130) Liu, X.-L.; Li, Y.-S.; Zhu, G.-Q.; Ban, Y.-J.; Xu, L.-Y.; Yang, W.-S. An Organophilic Pervaporation Membrane Derived from Metal-Organic Framework Nanoparticles for Efficient Recovery of Bio-Alcohols. *Angew. Chemie, Int. Ed.* **2011**, *50*, 10636–10639.

(131) Noble, R. D. Generalized Microscopic Mechanism of Facilitated Transport in Fixed Site Carrier Membranes. *J. Memb. Sci.* **1992**, *75*, 121–129.

(132) Pinnau, I.; Toy, L. G. Solid Polymer Electrolyte Composite Membranes for Olefin/paraffin Separation. *J. Memb. Sci.* **2001**, *184*, 39–48.

(133) Garboczi, E. J.; Snyder, K. A.; Douglas, J. F.; Thorpe, M. F. Geometrical Percolation Threshold of Overlapping Ellipsoids. *Phys. Rev. E* **1995**, *52*, 819–828.

(134) Mahajan, R.; Koros, W. J. Factors Controlling Successful Formation of Mixed-Matrix Gas Separation Materials. *Ind. Eng. Chem. Res.* **2000**, *39*, 2692–2696.

(135) Stock, N.; Biswas, S. Synthesis of Metal-Organic Frameworks (MOFs): Routes to Various MOF Topologies, Morphologies, and Composites. *Chem. Rev.* **2012**, *112*, 933–969.

(136) Kong, X.; Scott, E.; Ding, W.; Mason, J. A.; Long, J. R.; Reimer, J. A. CO2 Dynamics in a Metal-Organic Framework with Open Metal Sites. *J. Am. Chem. Soc.* **2012**, *134*, 14341–14344.

(137) Kandiah, M.; Nilsen, M. H.; Usseglio, S.; Jakobsen, S.; Olsbye, U.; Tilset, M.; Larabi, C.; Quadrelli, E. A.; Bonino, F.; Lillerud, K. P. Synthesis and Stability of Tagged UiO-66 Zr-MOFs. *Chem. Mater.* **2010**, *22*, 6632–6640.

(138) Taddei, M.; Dau, P. V.; Cohen, S. M.; Ranocchiari, M.; van Bokhoven, J. a.; Costantino, F.; Sabatini, S.; Vivani, R. Efficient Microwave Assisted Synthesis of Metal–organic Framework UiO-66: Optimization and Scale up. *Dalt. Trans.* **2015**, *44*, 14019–14026.

(139) Ni, Z.; Masel, R. I. Rapid Production of Metal–Organic Frameworks via Microwave-Assisted Solvothermal Synthesis. *J. Am. Chem. Soc.* **2006**, *128*, 12394–12395.

(140) Lin, Z.; Wragg, D. S.; Morris, R. E. Microwave-Assisted Synthesis of Anionic Metal?organic Frameworks under Ionothermal Conditions. *Chem. Commun.* **2006**, *4*, 2021.

(141) Li, Y.; Yang, W. Microwave Synthesis of Zeolite Membranes: A Review. *J. Memb. Sci.* **2008**, *316*, 3–17.

(142) Rittigstein, P.; Priestley, R. D.; Broadbelt, L. J.; Torkelson, J. M. Model Polymer Nanocomposites Provide an Understanding of Confinement Effects in Real Nanocomposites. *Nat. Mater.* **2007**, *6*, 278–282.

(143) Rong, M. Z.; Zhang, M. Q.; Zheng, Y. X.; Zeng, H. M.; Walter, R.; Friedrich, K. Structure–property Relationships of Irradiation Grafted Nano-Inorganic Particle Filled Polypropylene Composites. *Polymer (Guildf).* **2001**, *42*, 167–183.

(144) Li, Y.; Chung, T.; Cao, C.; Kulprathipanja, S. The Effects of Polymer Chain Rigidification, Zeolite Pore Size and Pore Blockage on Polyethersulfone (PES)-Zeolite A Mixed Matrix Membranes. *J. Memb. Sci.* **2005**, *260*, 45–55.

(145) Yang, Q.; Wiersum, A. D.; Llewellyn, P. L.; Guillerm, V.; Serre, C.; Maurin, G. Functionalizing Porous Zirconium Terephthalate UiO-66(Zr) for Natural Gas Upgrading: A Computational Exploration. *Chem. Commun.* **2011**, *47*, 9603–9605.

(146) Jones, S. B.; Friedman, S. P. Particle Shape Effects on the Effective Permittivity of Anisotropic or Isotropic Media Consisting of Aligned or Randomly Oriented Ellipsoidal Particles. *Water Resour. Res.* **2000**, *36*, 2821–2834.

(147) U.S.DOE. Annual Energy Outlook 2015. **2015**, 154.

(148) Baker, R. W.; Lokhandwala, K. Natural Gas Processing with Membranes: An Overview. *Ind. Eng. Chem. Res.* **2008**, *47*, 2109–2121.

(149) Li, J.-R.; Kuppler, R. J.; Zhou, H.-C. Selective Gas Adsorption and Separation in Metal-Organic Frameworks. *Chem. Soc. Rev.* **2009**, *38*, 1477–1504.

(150) Gascon, J.; Kapteijn, F. Metal-Organic Framework Membranes--High Potential, Bright Future? *Angew. Chem. Int. Ed. Engl.* **2010**, *49*, 1530–1532.

(151) Shah, M.; McCarthy, M. C.; Sachdeva, S.; Lee, A. K.; Jeong, H. K. Current Status of Metal-Organic Framework Membranes for Gas Separations: Promises and Challenges. *Ind. Eng. Chem. Res.* **2012**, *51*, 2179–2199.

(152) Qiu, S.; Xue, M.; Zhu, G. Metal-Organic Framework Membranes: From Synthesis to

Separation Application. *Chem. Soc. Rev.* **2014**, *43*, 6116–6140.

(153) Su, N. C.; Sun, D. T.; Beavers, C. M.; Britt, D. K.; Queen, W. L.; Urban, J. J. Enhanced Permeation Arising from Dual Transport Pathways in Hybrid polymer–MOF Membranes. *Energy Environ. Sci.* **2016**, *9*, 922–931.

(154) Diestel, L.; Wang, N.; Schwiedland, B.; Steinbach, F.; Giese, U.; Caro, J. MOF Based MMMs with Enhanced Selectivity due to Hindered Linker Distortion. *J. Memb. Sci.* **2015**, *492*, 181–186.

(155) Kanehashi, S.; Chen, G. Q.; Ciddor, L.; Chaffee, A.; Kentish, S. E. The Impact of Water Vapor on CO 2 Separation Performance of Mixed Matrix Membranes. *J. Memb. Sci.* **2015**, *492*, 471–477.

(156) Adatoz, E.; Avci, A. K.; Keskin, S. Opportunities and Challenges of MOF-Based Membranes in Gas Separations. *Sep. Purif. Technol.* **2015**, *152*, 207–237.

(157) Hao, L.; Li, P.; Yang, T.; Chung, T. S. Room Temperature Ionic liquid/ZIF-8 Mixed-Matrix Membranes for Natural Gas Sweetening and Post-Combustion CO2 Capture. *J. Memb. Sci.* **2013**, *436*, 221–231.

(158) Bux, H.; Liang, F.; Li, Y.; Cravillon, J.; Wiebcke, M.; Caro, J. Zeolitic Imidazolate Framework Membrane with Molecular Sieving Properties by Microwave-Assisted Solvothermal Synthesis. *J. Am. Chem. Soc.* **2009**, *131*, 16000–16001.

(159) Huang, A.; Dou, W.; Caro, J. Steam-Stable Zeolitic Imidazolate Framework ZIF-90 Membrane with Hydrogen Selectivity through Covalent Functionalization. *J. Am. Chem. Soc.* **2010**, *132*, 15562–15564.

(160) Pan, Y.; Li, T.; Lestari, G.; Lai, Z. Effective Separation of Propylene/propane Binary Mixtures by ZIF-8 Membranes. *J. Memb. Sci.* **2012**, *390-391*, 93–98.

(161) Pan, Y.; Liu, W.; Zhao, Y.; Wang, C.; Lai, Z. Improved ZIF-8 Membrane: Effect of Activation Procedure and Determination of Diffusivities of Light Hydrocarbons. *J. Memb. Sci.* **2015**, *493*, 88–96.

(162) Bux, H.; Feldhoff, A.; Cravillon, J.; Wiebcke, M.; Li, Y. S.; Caro, J. Oriented Zeolitic Imidazolate Framework-8 Membrane with Sharp H 2/C3H8 Molecular Sieve Separation. *Chem. Mater.* **2011**, *23*, 2262–2269.

(163) Guerrero, V. V.; Yoo, Y.; McCarthy, M. C.; Jeong, H.-K. HKUST-1 Membranes on Porous Supports Using Secondary Growth. *J. Mater. Chem.* **2010**, *20*, 3938.

(164) Shekhah, O.; Eddaoudi, M. The Liquid Phase Epitaxy Method for the Construction of Oriented ZIF-8 Thin Films with Controlled Growth on Functionalized Surfaces. *Chem. Commun. (Camb).* **2013**, *49*, 10079–10081.

(165) Kida, K.; Fujita, K.; Shimada, T.; Tanaka, S.; Miyake, Y. Layer-by-Layer Aqueous Rapid Synthesis of ZIF-8 Films on a Reactive Surface. *Dalt. Trans.* **2013**, *42*, 11128–11135.

(166) Shekhah, O.; Wang, H.; Kowarik, S.; Schreiber, F.; Paulus, M.; Tolan, M.; Sternemann, C.; Evers, F.; Zacher, D.; Fischer, R. a; *et al.* Step-by-Step Route for the Synthesis of Metal-Organic Frameworks. *J. Am. Chem. Soc.* **2007**, *129*, 15118–15119.

(167) Bétard, A.; Bux, H.; Henke, S.; Zacher, D.; Caro, J.; Fischer, R. A. Fabrication of a CO2-Selective Membrane by Stepwise Liquid-Phase Deposition of an Alkylether Functionalized Pillared-Layered Metal-Organic Framework [Cu2L2P]n on a Macroporous Support. *Microporous Mesoporous Mater.* **2012**, *150*, 76–82.

(168) So, M. C.; Jin, S.; Son, H.-J.; Wiederrecht, G. P.; Farha, O. K.; Hupp, J. T. Layer-by-Layer Fabrication of Oriented Porous Thin Films Based on Porphyrin-Containing Metal–Organic Frameworks. *J. Am. Chem. Soc.* **2013**, *135*, 15698–15701.

(169) Heinke, L.; Tu, M.; Wannapaiboon, S.; Fischer, R. A.; Wöll, C. Surface-Mounted Metal-Organic Frameworks for Applications in Sensing and Separation. *Microporous Mesoporous Mater.* **2015**, *216*, 200–215.

(170) Park, K. S.; Ni, Z.; Côté, A. P.; Choi, J. Y.; Huang, R.; Uribe-Romo, F. J.; Chae, H. K.; O'Keeffe, M.; Yaghi, O. M. Exceptional Chemical and Thermal Stability of Zeolitic Imidazolate Frameworks. *Proc. Natl. Acad. Sci. U. S. A.* **2006**, *103*, 10186–10191.

(171) Venna, S. R.; Carreon, M. a. Highly Permeable Zeolite Imidazolate Framework-8 Membranes for CO 2/CH4 Separation. *J. Am. Chem. Soc.* **2010**, *132*, 76–78.

(172) Huang, K.; Dong, Z.; Li, Q.; Jin, W. Growth of a ZIF-8 Membrane on the Inner-Surface of a Ceramic Hollow Fiber via Cycling Precursors. *Chem. Commun.* **2013**, *49*, 10326–10328.

(173) Yeo, Z. Y.; Chai, S.-P.; Zhu, P. W.; Mohamed, A. R. An Overview: Synthesis of Thin Films/membranes of Metal Organic Frameworks and Its Gas Separation Performances. *RSC Adv.* **2014**, *4*, 54322–54334.

(174) Blinova, N. V.; Stejskal, J.; Fréchet, J. M. J.; Svec, F. Effect of Reaction Conditions on Film Morphology of Polyaniline Composite Membranes for Gas Separation. *J. Polym. Sci. Part A Polym. Chem.* **2012**, *50*, 3077–3085.

(175) Blinova, N. V.; Svec, F. Functionalized Polyaniline-Based Composite Membranes with Vastly Improved Performance for Separation of Carbon Dioxide from Methane. *J. Memb. Sci.* **2012**, *423-424*, 514–521.

(176) Blinova, N. V; Svec, F. Functionalized High Performance Polymer Membranes for Separation of Carbon Dioxide and Methane. *J. Mater. Chem. A* **2014**, *2*, 600–604.

(177) Anderson, J. L.; Dixon, J. K.; Brennecke, J. F. Solubility of CO2, CH4, C2H6, C2H4, O2, and N2 in 1-Hexyl-3-Methylpyridinium Bis(trifluoromethylsulfonyl)imide: Comparison to Other Ionic Liquids. *Acc. Chem. Res.* **2007**, *40*, 1208–1216.

(178) Vicent-Luna, J. M. J. M.; Jose, J.; Anta, J. A.; Gutiérrez-Sevillano, J. J.; Calero, S. Effect of Room-Temperature Ionic Liquids on CO2 Separation by a Cu-BTC Metal–Organic Framework. *J. Phys. Chem. C* **2013**, *117*, 20762–20768.

(179) Tian, F.; Cerro, A. M.; Mosier, A. M.; Wayment-Steele, H. K.; Shine, R. S.; Park, A.; Webster, E. R.; Johnson, L. E.; Johal, M. S.; Benz, L. Surface and Stability Characterization of a Nanoporous ZIF-8 Thin Film. *J. Phys. Chem. C* **2014**, *118*, 14449–14456.

(180) Lin, H.; Freeman, B. D. Gas and Vapor Solubility in Cross-Linked Poly(ethylene Glycol Diacrylate). *Macromolecules* **2005**, *38*, 8394–8407.

(181) Bakhtin, D.; Eremin, Y. S.; Grekhov, a. M.; Volkov, V. V. Gas Permeability of PVTMS/CNT Mixed Matrix Membranes. *Phys. Procedia* **2015**, *72*, 166–170.

(182) Eremin, Y. S.; Grekhov, a. M. Calculation of Percolating Clusters Characteristics in Mixed Matrix Membrane with CNT. *Phys. Procedia* **2015**, *72*, 37–41.

Appendix

A.1 Supporting Information for Chapter 2

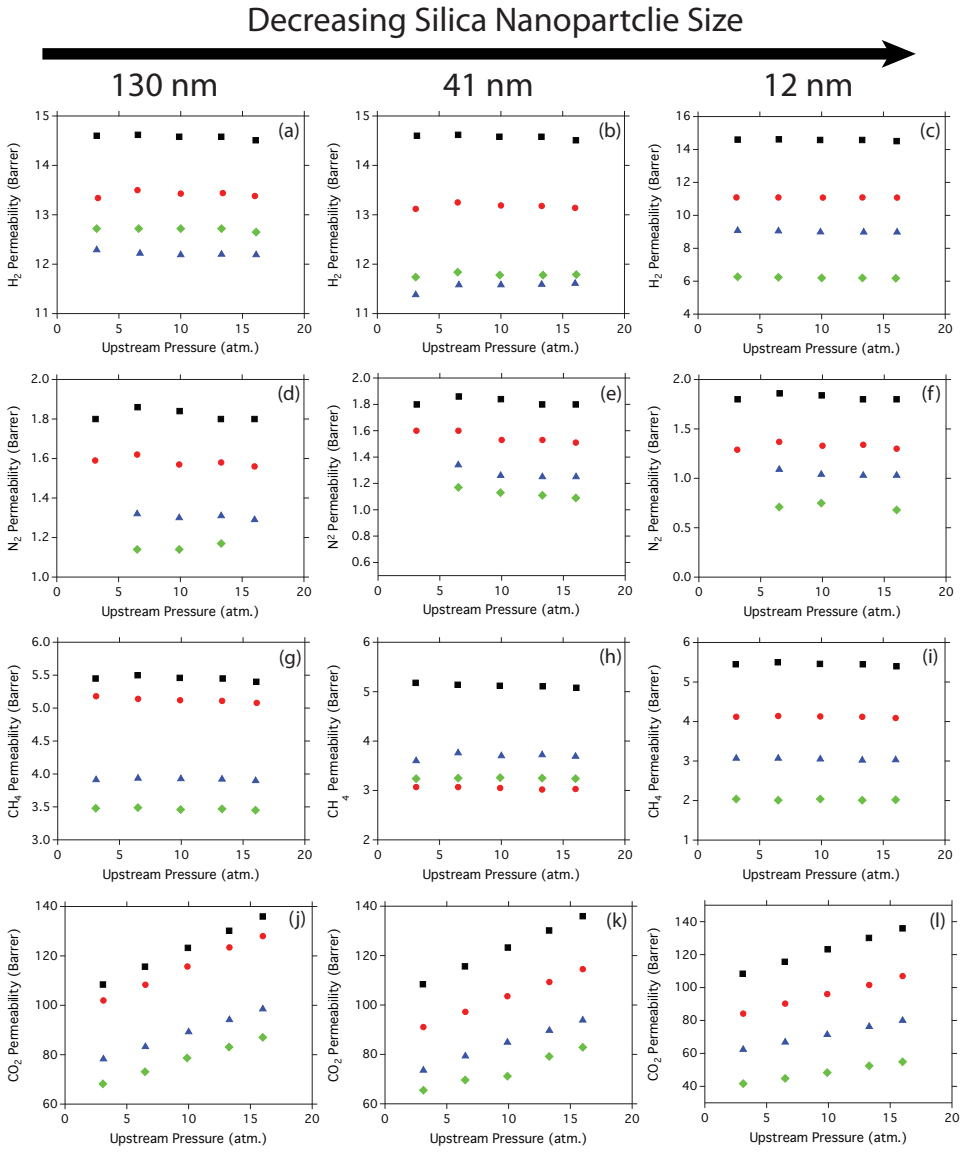

Figure A.1. Pure gas permeability of XLPEG/silica composites plotted over pressure. a)-c) H_2 permeabilities, d)-f) N_2 permeabilities, g)-i) CH_4 permeabilities, and j)-l) CO_2 permeabilities. Silica nanoparticle size decreases from left to right in for each respective gas. Vol% loading are approximately 0 vol% (diamonds), 7-9 vol% (circles), 17-19 vol%, (triangles) and 27-30 vol% (squares)

Table A.1. Pure Gas Permeability and Selectivity of Various Gases at 6 atm and 35 °C.

Polymer	Silica Size (nm)	ϕ_{SiO2}× (100%)	H_2	N_2	CH_4	CO_2	CO_2/H_2	CO_2/N_2	$CO_2/CH4$
XLPEGDA	-	0	14.6 ± 0.17	1.86 ± 0.03	5.5 ± 0.07	116 ± 1.4	7.9 ± 0.2	62.2 ± 1.2	21 ± 0.4
XLPEGDA	109 ± 15	6.9	13.5 ± 0.23	1.62 ± 0.032	5.14 ± 0.078	108 ± 1.6	8 ± 0.2	67 ± 1.7	21.1 ± 0.5
XLPEGDA	109 ± 15	17	12.2 ± 0.23	1.32 ± 0.03	3.93 ± 0.075	83.2 ± 1.5	6.8 ± 0.2	63 ± 1.8	21.2 ± 0.6
XLPEGDA	109 ± 15	27	12.7 ± 0.19	1.14 ± 0.02	3.49 ± 0.052	73.1 ± 1	5.7 ± 0.1	64.1 ± 1.4	20.9 ± 0.5
XLPEGDA	38 ± 3.8	7.9	13.2 ± 0.27	1.6 ± 0.036	4.58 ± 0.094	97.2 ± 2	7.3 ± 0.2	60.8 ± 1.8	21.3 ± 0.6
XLPEGDA	38 ± 3.8	17	11.6 ± 0.3	1.34 ± 0.038	3.76 ± 0.098	79.3 ± 2	6.9 ± 0.3	59.4 ± 2.3	21.1 ± 0.8
XLPEGDA	38 ± 3.8	28	11.8 ± 0.2	1.17 ± 0.03	3.25 ± 0.058	69.7 ± 1.2	5.9 ± 0.2	59.5 ± 1.8	21.4 ± 0.7
XLPEGDA	12 ± 1.2	7.8	11.1 ± 0.26	1.37 ± 0.036	4.14 ± 0.064	90.2 ± 1.3	8.1 ± 0.2	62.2 ± 1.2	21 ± 0.4
XLPEGDA	12 ± 1.2	19	9 ± 0.14	1.09 ± 0.023	3.07 ± 0.049	66.8 ± 1	7.4 ± 0.2	65.9 ± 2	21.8 ± 0.7
XLPEGDA	12 ± 1.2	30	6.2 ± 0.23	0.71 ± 0.02	2.01 ± 0.036	44.9 ± 0.7	7.2 ± 0.2	61.5 ± 1.6	21.8 ± 0.6

A.2 Supporting Information for Chapter 3

Table A.2. BET surface area measurements of silica nanoparticles before and after silanization with APTES

Silica Nanoparticles	BET Surface Area (m^2/g)
Before silanization	293
After silanization with APTES	236

Table A.3. Pure gas permeability of XLPEG/silica hybrid membranes

XLPEG/Silica-APTES Permeability (Barrer)				XLPEG/Silica-OH Permeability (Barrer)			
Silica volume %	CO_2	N_2	CH_4	Silica volume %	CO_2	N_2	CH_4
0.0%	116	1.9	5.5	0%	116	1.9	5.5
2.7%	134	2.1	6.4	7.8%	90	1.4	4.1
6.6%	130	2.1	6.3	19%	67	1.1	3.1
10.2%	125	2.0	6.1				
16.2%	109	1.7	5.3				

Table A.4. Pure gas selectivity of XLPEG/silica hybrid membranes

XLPEG/Silica-APTES Permeability (Barrer)			XLPEG/Silica-OH Permeability (Barrer)		
	CO2/N2	CO2/CH4	volume %	CO2/N2	CO2/CH4
0.0%	62	21	0%	62	21
2.7%	63	21	7.8%	66	22
6.6%	62	21	19%	62	22
10.2%	62	20			
16.2%	64	21			

Table A.5. Solubility selectivity of hybrid membranes for CO_2/CH_4

	S_{CO2}/S_{CH4}	
	This Work	Lin *et al.*[180]
XLPEG	15.5	10.6
2.7 vol% Silica	16.6	-
6.6 vol% Silica	18.4	-
10 vol% Silica	20.8	-
16 vol% Silica	21.8	-

A.3 Supporting Information for Chapter 4

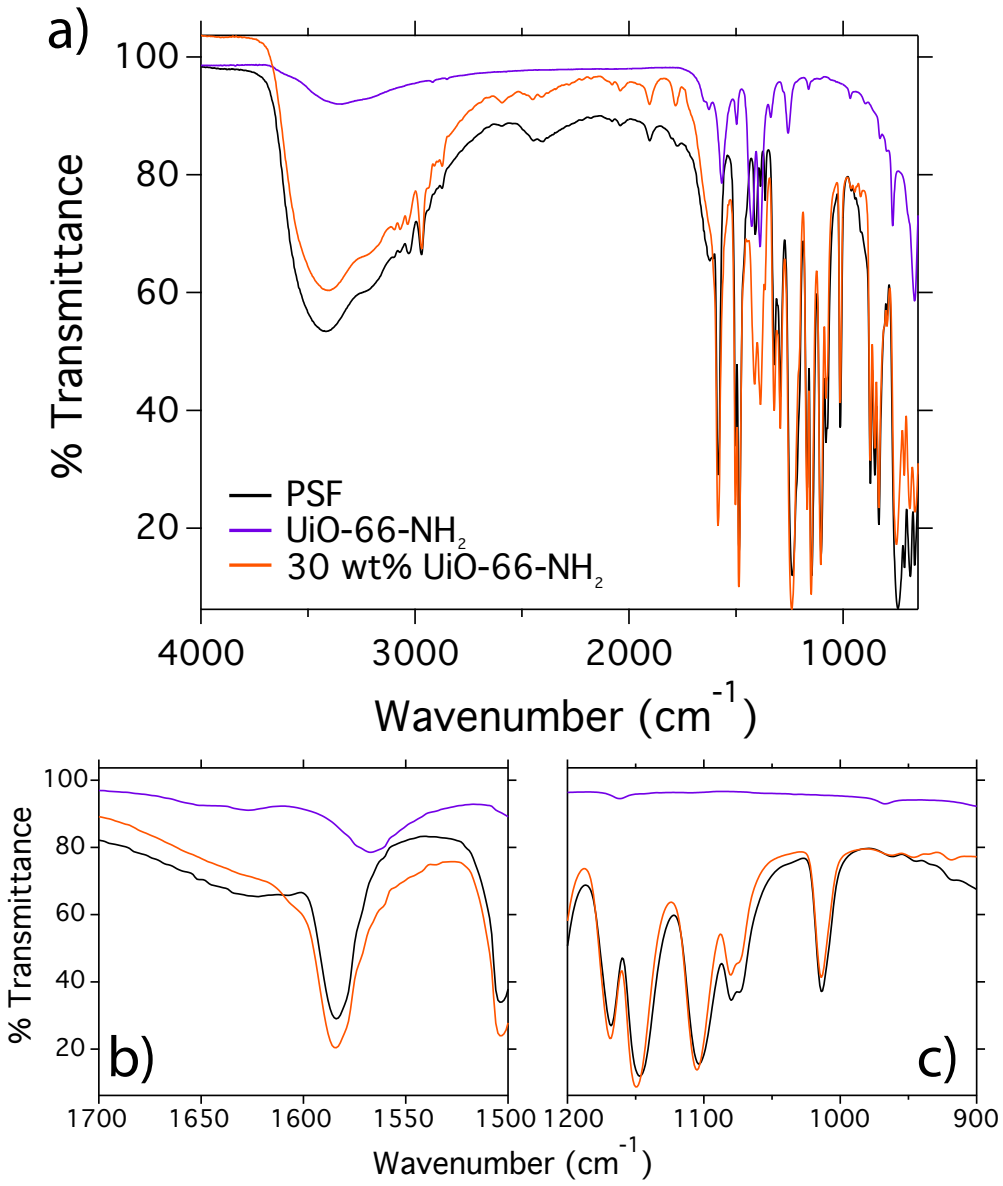

Figure A.2. a) FT-IR spectra of UiO-66-NH_2, PSF, and 30 wt% UiO-66-NH_2/PSF. b) Primary amine peak of UiO-66-NH_2 at 1567 cm^{-1} becomes less apparent upon incorporation with PSF at 30 wt% indicating possible hydrogen-bonding interactions. c) Sulfonyl peak at 1150 and 1170 cm^{-1} does not shift with addition of UiO-66-NH_2

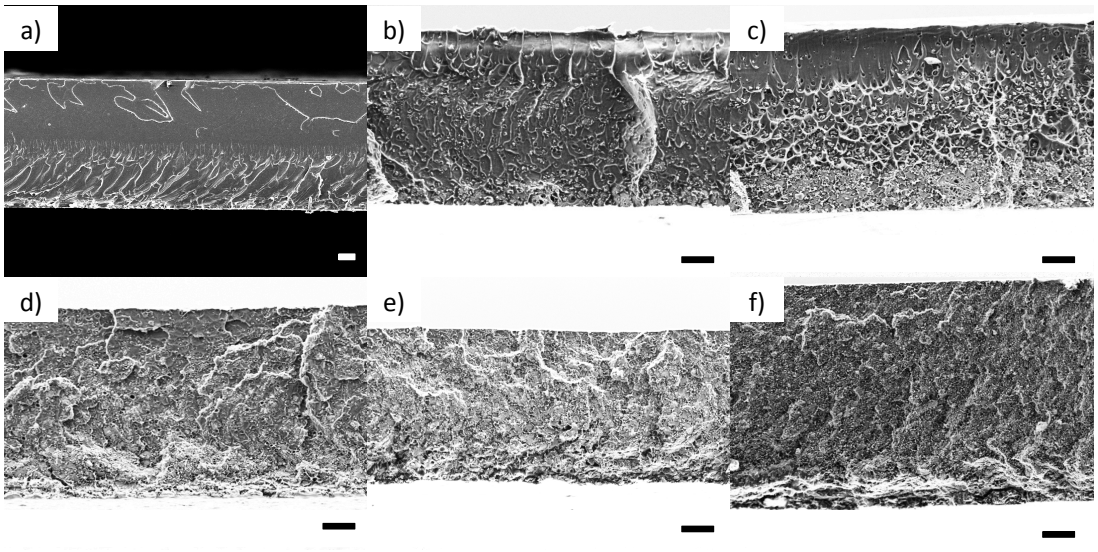

Figure A.3. Thickness of hybrid membranes. a) PSF, b) 10 wt% UiO-66-NH_2, c) 20 wt% UiO-66-NH_2, d) 30 wt% UiO-66-NH_2, e) 40 wt% UiO-66-NH_2, f) 50 wt% UiO-66-NH_2. All scale bars represent 10 μm.

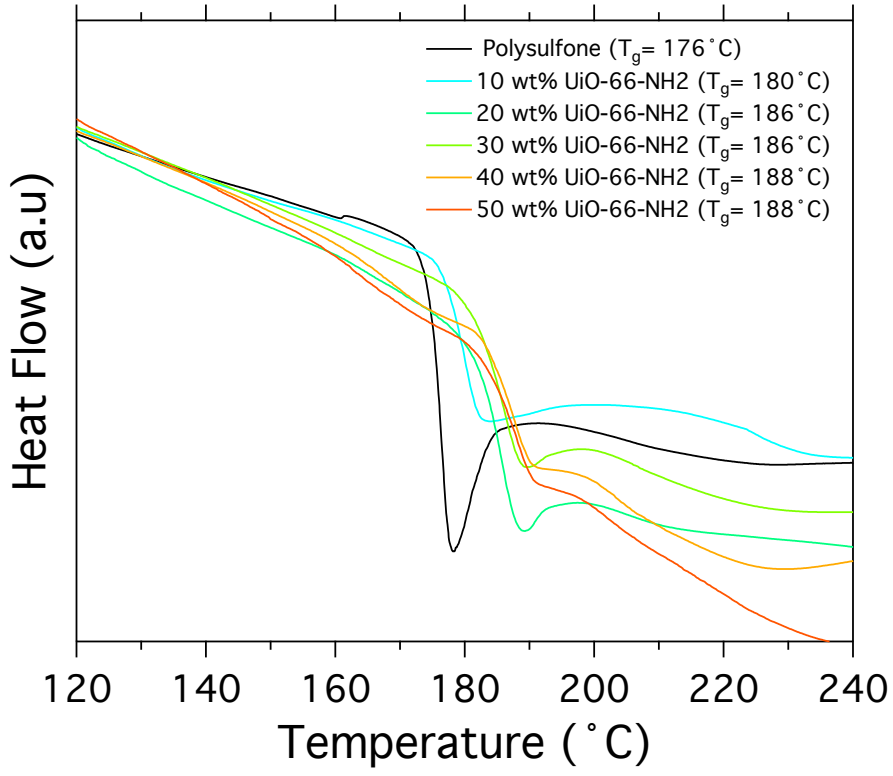

Figure A.3 DSC thermograms of UiO-66-NH2 PSF hybrid membranes. Scan rate 20 °C/min. Tg increases with increasing MOF loading.

Table A.6. CO_2, N_2, and CH_4 permeabilities in barrers for UiO-66-NH_2 at 3 bar and 35 °C

MOF Weight %	N_2	CH_4	CO_2
0%	0.19 ± 0.011	0.21 ± 0.017	5.6 ± 0.32
10%	0.41 ± 0.012	0.45 ± 0.013	11 ± 0.32
20%	0.61 ± 0.032	0.68 ± 0.036	16 ± 0.86
30%	0.67 ± 0.017	0.77 ± 0.02	19 ± 0.47
40%	1.7 ± 0.024	1.9 ± 0.28	46 ± 6.2
50%	1.65 ± 0.022	1.8 ± 0.28	43 ± 4.8

Table A.7. CO_2/CH_4 and CO_2/N_2 selectivities for UiO-66-NH_2 at 3 bar and 35 °C

MOF Weight %	CO_2/CH_4	CO_2/N_2
0%	27	30
10%	25	27
20%	24	27
30%	24	28
40%	24	27
50%	24	26

Gas transport above the percolation threshold can be understood by the following equation:[181,182]

$$P_{Hybrid} = P_{cluster}\phi_{cluster} + P_{polymer}(1 - \phi_{cluster}) \quad (8.3)$$

where P_{Hybrid} is the permeability of the hybrid membrane, $P_{cluster}$ is the permeability of the percolation cluster, $\phi_{cluster}$ is the volume fraction of the percolation cluster, and $P_{polymer}$ is the permeability of the polymer. We were not able to quantify the volume fraction of the MOF that participated as a percolation cluster but we believe it to be only a small fraction of the total MOF available for transport.

Table A.8. Diffusivity, Solubility, and Gas Uptake Values for UiO-66-NH_2 membranes at 3 bar and 35 °C

	Diffusion*10^8 (cm^2/s)			Solubility (cm^3(STP)/(cm^3 atm))			Gas Uptake(cm^3/(cm^3 atm))		
MOF wt%	N_2	CH_4	CO_2	N_2	CH_4	CO_2	N_2	CH_4	CO_2
0%	0.72	0.18	1.1	0.20	0.90	4.0	0.63	2.8	12.5
10%	1	0.27	1.5	0.30	1.2	5.8	0.92	3.9	17.9
20%	1.3	0.42	1.9	0.35	1.2	6.4	1.1	3.8	19.8
30%	1.2	0.39	1.7	0.44	1.5	8.1	1.4	4.7	25.5
40%	1.5	0.7	3.1	0.92	2.3	11.6	2.8	7.2	36.0
50%	1.7	0.69	2.9	0.88	2.4	12.3	2.7	7.6	38.2

A.4 Supporting Information for Chapter 5

Table A.9. CH_4 and CO_2 Permeance and selectivity for PANI membrane

Pressure (bar)	CH_4 (GPU)	CO_2 (GPU)	CO_2/CH_4
1.1	1.94 +/- 0.04	25.5 +/- 0.58	12.3 +/- 0.4
2.2	2.01 +/- 0.03	24.78 +/- 0.39	12.4 +/- 0.2
3.1	2.02 +/- 0.03	25.21 +/- 0.4	12.6 +/- 0.2
4.1	2.05 +/- 0.03	25.99 +/- 0.41	12.4 +/- 0.2

Table A.10. CH_4 and CO_2 Permeance and selectivity for ZIF-8/290 membrane

Pressure (bar)	CH_4 (GPU)	CO_2 (GPU)	CO_2/CH_4
1.1	2.12 +/- 0.03	27.7 +/- 0.3	13 +/- 0.2
2.2	2.43 +/- 0.02	28.29 +/- 0.26	11.6 +/- 0.1
3.1	2.75 +/- 0.02	28.64 +/- 0.27	10.3 +/- 0.1
4.1	3.1 +/- 0.03	29.85 +/- 0.3	9.6 +/- 0.1

Table A.11. CH_4 and CO_2 Permeance and selectivity for ZIF-8/500 membrane

Pressure (bar)	CH_4 (GPU)	CO_2 (GPU)	CO_2/CH_4
1.1	0.5 +/- 0.011	12.5 +/- 0.1	24.9 +/- 1.9
2.2	0.55 +/- 0.006	13.9 +/- 0.1	25 +/- 1.3
3.1	0.77 +/- 0.008	14.3 +/- 0.1	18.6 +/- 0.9
4.1	0.94 +/- 0.009	14.7 +/- 0.1	15.6 +/- 0.7

Table A.12. CH_4 and CO_2 Permeance and selectivity for ZIF-8/900 membrane

Pressure (bar)	CH_4 (GPU)	CO_2 (GPU)	CO_2/CH_4
1.1	0.56 +/- 0.02	13.8 +/- 0.42	24.6 +/- 1.2
2.2	0.9 +/- 0.03	15 +/- 0.42	16.5 +/- 0.7
3.1	1.13 +/- 0.03	15.5 +/- 0.43	13.6 +/- 0.5
4.1	1.33 +/- 0.04	16.1 +/- 0.45	12 +/- 0.5